

# **Run 2b Trigger Conceptual Design Report**

The DØ Collaboration

October 8, 2001

Draft version 2.3

# **Contents**

Contents	2
1 Introduction	8
1.1 Overview	8
1.2 Trigger Upgrade Motivation	9
2 Triggers, Trigger Terms and Trigger Rates	11
2.1 Overview of the DØ Trigger System	11
2.2 Leptonic Triggers	12
2.3 Leptons plus Jets	13
2.4 Leptons/Jets plus Missing E <sub>T</sub>	13
2.5 Triggers for Higgs Searches	13
2.6 Trigger Menu and Rates	14
3 Level 1 Tracking Trigger	15
3.1 Goals	15
3.1.1 Track Triggers	15
3.1.2 Electron/Photon Identification	16
3.1.3 Track Matching	16
3.2 Description of Current Tracking Trigger	16
3.2.1 Tracking Detectors	16
3.2.2 CTT Segmentation	17
3.2.3 CTT Electronics	19
3.2.4 CTT Outputs	19
3.2.5 Tracking Algorithm	20
3.3 Fiber Tracker Trigger Operation at 132 ns bunch spacing	22
3.3.1 Introduction	22
3.3.2 SIFT Replacement: the TriP ASIC	23
3.3.3 High Speed ADC	24
3.3.4 FPGA	24
3.3.5 Preliminary Cost Estimate	25
3.3.6 Milestones	26
3.4 Performance of Current Tracking Trigger	27

	3.4.1 Conclusions and implications for high luminosity	31
	3.4.2 Comments on the CFT Lifetime	31
;	3.5 Minimum Bias Models	33
(	3.6 Overview of Options	35
(	3.7 Axial CPS as Ninth Layer	35
	3.7.1 Concept and Implications	35
	3.7.2 Implementation	36
	3.7.3 Efficiency/Acceptance	36
	3.7.4 Rates and Rejection Improvements	36
	3.7.5 Cost & Schedule	37
	3.7.6 Conclusions	37
(	3.8 Stereo Track Processor	37
	3.8.1 Concept	37
	3.8.2 Simulation	39
	3.8.3 Implementation	41
	3.8.4 Conclusions	44
;	3.9 Singlet Equations	44
	3.9.1 Concept	44
	3.9.2 Simulation	46
	3.9.3 Rates and Rejection Improvements and Efficiency	46
	3.9.4 Implementation, Cost & Schedule	47
	3.9.5 Conclusions	49
;	3.10 L1 Tracking Trigger Summary and Conclusions	49
4 L	evel 1 Calorimeter Trigger	51
4	4.1 Goals	51
4	4.2 Description of Run 2a Calorimeter Electronics	52
	4.2.1 Overview	52
	4.2.2 Trigger pickoff	53
	4.2.3 Trigger summers	54
	4.2.4 Trigger sum driver	55
	4.2.5 Signal transmission, cable dispersion	55
4	4.3 Description of Current L1 Calorimeter Trigger	57
	4.3.1 Overview	57

4.3.2 Global Triggers	59
4.3.3 Cluster Triggers	59
4.3.4 Hardware Implementation	60
4.3.5 Physical Layout	62
4.4 Performance of the Current Calorimeter Trigger	62
4.4.1 Energy measurement and turn-on curves	62
4.4.2 Trigger rates	63
4.4.3 Conclusions/implications for high luminosity	65
4.5 Overview of Options for Improvement	66
4.5.1 Global view of options considered	66
4.6 Digital Filtering	67
4.6.1 Concept & physics implications	67
4.6.2 Pileup rejection	67
4.6.3 Simulation	68
4.6.4 Implementation	68
4.6.5 Conclusions	68
4.7 Sliding Trigger tower Windows for Jets and Electrons	69
4.7.1 Concept & physics implications	69
4.7.2 Simulation	70
4.7.3 Efficiency	71
4.7.4 Rates and rejection improvements	73
4.7.5 Implementation	75
4.7.6 Conclusions	76
4.8 Track Matching and Finer EM Segmentation	76
4.8.1 Concept & physics implications	76
4.8.2 Simulation	77
4.8.3 Rates and rejection improvements	77
4.8.4 Track matching gains for tracking	81
4.8.5 Change of EM granularity to Δφ=0.1	82
4.8.6 Implementation	
4.8.7 Conclusions	
4.9 Improving Missing E <sub>T</sub> Triggering using ICD Energy at Level 1	

4.9.1 Concept & physics implications	84
4.9.2 Simulation	86
4.9.3 Rates and rejection improvements from ICR energies	86
4.9.4 Improving Missing E $_{T}$ for Multiple interaction Events	87
4.9.5 Conclusions	90
4.10 Finer EM Tower Segmentation for electrons	90
4.10.1 Concept & physics implications	90
4.10.2 Simulation	91
4.10.3 Efficiency	92
4.10.4 Implementation	93
4.10.5 Conclusions	93
4.11 Topological Considerations	94
4.11.1 Concept & physics implications (acoplanar jets)	94
4.11.2 Efficiency	94
4.11.3 Rates and rejection improvements	97
4.11.4 Implementation	98
4.11.5 Conclusions	98
4.12 L1 Calorimeter Trigger Implementation	98
4.12.1 Constraints	98
4.12.2 L1 Calorimeter trigger hardware conceptual design	99
4.12.3 ADC/TAP Split	99
4.12.4 Granularity	100
4.12.5 Overlap	101
4.12.6 TAP implementation	102
4.12.7 Schedule, resources and cost estimate	104
4.12.8 Resources	104
4.12.9 Cost estimate	105
4.13 L1 Calorimeter Summary & Conclusions	105
5 L1 Muon Trigger	107
5.1 Goals	107
5.2 Description of the Current L1 Muon Trigger	107
5.2.1 Overview	107
5.2.2 Central Muon Trigger Algorithm (CF MTC05)	109

5.2.3 Central Muon Trigger Algorithm (CF MTC10)	109
5.2.4 Forward Muon Trigger Algorithms (EF MTC05)	110
5.2.5 Forward Muon Trigger Algorithms (EF MTC10)	110
5.3 Performance of the Current Muon Detector	111
5.4 Performance of the Current L1Muon Trigger	111
5.5 Estimating the Run 2b Performance of the L1 Muon Trigge	∍r112
5.6 Run 2b Issues	119
5.7 Summary	122
6 Level 2 Triggers	123
6.1 Goals	123
6.2 L2β Upgrade	123
6.2.1 Concept & physics implications	123
6.2.2 Implementation	124
6.2.3 Performance scaling	130
6.2.4 Cost & schedule	130
6.3 STT Upgrade	131
6.3.1 Concept & physics implications	131
6.3.2 STT Architecture	132
6.3.3 Reconfiguration of STT for Run 2b	133
6.3.4 Cost and Schedule	133
6.4 Other Level 2 Options	134
6.5 Conclusions for Level 2 Trigger	135
7 Level 3 Triggers	136
7.1 Status of the D0 Data Acquisition and Event Filtering	136
7.1.1 Description of Current Data Acquisition System	136
7.1.2 Status	138
7.1.3 An Alternate System	139
7.1.4 Comments on Current Status	140
7.2 Run 2b Upgrades to Level 3	141
7.3 Conclusions	142
8 Online Computing	143
8.1 Introduction	143

8.1.1 Scope	143
8.1.2 Software Architecture	143
8.1.3 Hardware Architecture	144
8.1.4 Motivations	144
8.1.5 Interaction with the Computing Division	146
8.2 Plan	146
8.2.1 Online Network	146
8.2.2 Level 3 Linux Filter Farm	147
8.2.3 Host Data Logging Systems	147
8.2.4 Control Room Systems	149
8.2.5 Data Monitoring Systems	149
8.2.6 Database Servers	149
8.2.7 File Servers	150
8.2.8 Slow Control Systems	151
8.3 Procurement Schedule	152
8.4 Summary	153
9 Summary and Conclusions	154
9.1 Cost Summary for Trigger Completion and Upgrades	156
A D0 Run 2b Trigger Task Force	158
A.1 Task Force Charge	158
A.2 Trigger Task Force Membership	159
B Level 2 $\beta$ and Level 2 STT Cost Estimates	160

### 1 Introduction

#### 1.1 Overview

We present in this report a description of the trigger and related upgrades D0 is proposing to mount in order to adequately address the Run 2b physics program. An initial draft of a Technical Design Report for the Run 2b silicon detector is presented to the Committee under separate cover; we include herein a discussion of the other — "non-silicon" - upgrades we are proposing. These include upgrades to the three trigger levels, as well as the online system. The motivation for these improvements, supported by Monte Carlo studies, is described in some detail, as are the technical descriptions of each of the proposed projects. Preliminary outlines of the cost and schedule for each of the upgrades are included as well.

The primary feature driving the reconsideration of the design of the Run 2b trigger elements is the higher rates associated with the approximately factor of 2.5 increase in instantaneous luminosity that will be delivered to the experiments. The concomitant increase in the integrated exposure motivates the silicon upgrade, and is less of a concern for the readout elements described here. Nevertheless, with the Run 2 program now expected to extend to 6 or more years of data taking, the long-term hardware needs and maintenance have become more of an issue. This extension of the run has motivated a somewhat modified approach to the development of the Run 2 detector and the associated organization with which we oversee it: we consider the distinction between Run 2a and 2b now as being for the most part artificial, and increasingly treat the Run 2 experiment as a continually evolving, integrated enterprise, with the goal being to optimize the physics reach over the entire run in as efficient and cost-effective a manner as possible. In part, this document represents our attempt to coalesce our recent thinking in this regard. Accordingly, we include in this report brief status reports and plans for the Fiber Tracker Trigger (SIFT) chip replacement for 132 nsec running, the Level 2β trigger system, and the data acquisition system all of which are needed for near-term physics running - in addition to those upgrades specifically targeted at addressing the increase in luminosity in 2004. The latter subject is the primary focus of this report. A description of the overall management of the Run 2b project for D0, including the trigger sub-projects discussed in this report, can be found in the silicon Technical Design Report submitted to this Committee under separate cover.

Finally, we note that the bulk of the information contained here – and particularly that portion of the report focusing on the increase in luminosity, along with the associated simulation studies – reflects the considerable efforts of the D0 Run 2b Upgrade Trigger Task Force. The 29-member Task Force was appointed on June 25, 2001 by the D0 Technical Manager (J. Kotcher); the charge and personnel are given in Appendix A. We take this opportunity to thank the Task Force for its dedication and perseverance in providing the experiment with the basis on which these trigger upgrades can be defined and pursued.

### 1.2 Trigger Upgrade Motivation

A powerful and flexible trigger is the cornerstone of a modern hadron collider experiment. It dictates what physics processes can be studied properly and what is ultimately left unexplored. The trigger must offer sufficient flexibility to respond to changing physics goals and new ideas. It should allow the pursuit of complementary approaches to a particular event topology in order to maximize trigger efficiency and allow measurement of trigger turn-on curves. Adequate bandwidth for calibration, monitoring, and background samples must be provided in order to calibrate the detector and control systematic errors. If the trigger is not able to achieve sufficient selectivity to meet these requirements, the capabilities of the experiment will be seriously compromised.

As described in the charge to the D0 Run 2b Upgrade Trigger Task Force in Appendix A, a number of ground rules were established for our studies that reflect the expected Run 2b environment. We anticipate operating at a peak luminosity of ~5×10<sup>32</sup> cm<sup>-2</sup>s<sup>-1</sup> in Run 2b, which is a factor of 2.5 higher than the Run 2a design luminosity. The higher luminosity leads to increased rates for all physics processes, both signal and backgrounds. Assuming ~100 bunches and 132 ns bunch spacing, this leads to an average of ~5 non-diffractive "minbias" interactions superimposed on the hard scattering. The increased luminosity also increases occupancies in the detector, leading to a substantial loss in trigger rejection for some systems.

We plan to retain the present trigger architecture with three trigger levels. The Level 1 (L1) trigger employs fast, deterministic algorithms, generating an accept/reject decision every 132 ns. The Level 2 (L2) trigger utilizes DSPs and high performance processors with variable processing time, but must issue its accept/reject decisions in order. The Level 3 (L3) trigger is based on high-performance processors and is completely asynchronous. The L1 and L2 trigger rely on dedicated trigger data paths, while the L3 trigger utilizes the DAQ readout to collect all event data in a L3 processing node.

We cannot accommodate the higher luminosity by simply increasing trigger rates. The L1 trigger rate is limited to a peak rate of ~5 kHz by readout deadtime. The L2 trigger rate is limited to a peak rate of ~1 kHz by the calorimeter digitization time. Finally, we have set a goal of ~50 Hz for the L3 trigger rate to limit the strain on data storage and offline computing.

The above L1 and L2 trigger rates are essentially the same as for Run 2a. Thus, we must accommodate the higher luminosity in Run 2b by increasing the L1 trigger rejection by a factor of 2.5 and maintaining the current L2 rejection factor of 5. Studying various ways of meeting these goals was the major focus of the efforts of the Task Force.

Our ability to plan a Run 2b trigger upgrade is further limited by the relatively short time available in which to plan. We must have a high degree of confidence that the required trigger upgrades can begin to be deployed at the start of the shutdown associated with the installation of the Run 2b silicon, currently scheduled for mid-2004. This goal is made all the more challenging by the need

to simultaneously complete and commission the Run 2a detector, acquire physics data, and exploit the resulting physics opportunities. Thus, it is essential that the number and scope of the proposed Run 2b trigger upgrades not exceed the resources of the collaboration.

In the sections below, we describe the results of Task Force studies for these upgrades. We first consider various options for improving the L1 track trigger, since the tracks found by this trigger are potentially useful to the other triggers. We then examine replacement of the L1 calorimeter trigger, which is one of the few remaining pieces of Run 1 electronics in DØ, with entirely new electronics. This upgrade will employ digital filtering to better associate energy with the correct beam crossing, and provide the capability of clustering energy to form It will also allow improved  $e/y/\tau$  triggers that make use of energy flow jets. (HAD/EM, cluster shape/size, isolation) and tracking information. The sections that follow describe possible upgrades to the L1 muon trigger, processor and Silicon Track Trigger (STT) upgrades of the L2 trigger, processor upgrades for the L3 trigger, and plans for improvements to the online system. As mentioned above, we also intersperse status reports of the outstanding Run 2a trigger projects – SIFT, L2β project, and L3 - in the relevant sections. The last section summarizes the results and conclusions of the report.

# 2 Triggers, Trigger Terms and Trigger Rates

At 2 TeV, the inelastic proton-antiproton cross section is very large, about 50 mb. At Run II luminosities, this results in interaction rates up to and beyond 10 MHz, with multiple interactions occurring during each beam crossing. Virtually all of these events are without interest to the physics program. In contrast, at these luminosities W bosons are produced at a few Hz; a few top quark pairs are produced per hour. It is evident that sophisticated triggers are necessary to separate out the rare events of physics interest from the overwhelming backgrounds. Rejection factors of nearly 10<sup>6</sup> must be achieved in decision times of a few milliseconds.

The salient features of interesting physics events naturally break down into specific signatures which can be sought after in a programmable trigger. The appearance in an event of high  $p_T$  leptons, for example, can signal the presence of a W or a Z. Combined with jets containing b quark tags, the same lepton signature could now be indicative of top quark pair production or the Higgs. Leptons combined instead with missing energy is a classic SUSY discovery topology, etc. The physics "menu" of Run 2 is mainly built on the menu of signatures and topologies available to the trigger. In order for the physics program to succeed, these fundamental objects must exist and must remain uncompromised at the highest luminosities. The following paragraphs give a brief overview of the trigger system and a sampling of the physics impact of the various combinations of trigger objects.

# 2.1 Overview of the DØ Trigger System

The DØ trigger system for Run 2 is divided into three levels of increasing complexity and capability. The Level 1 (L1) trigger is entirely implemented in hardware (see Figure 1). It looks for patterns of hits or energy deposition consistent with the passage of high energy particles through the detector. The calorimeter trigger tests for energy in calorimeter towers above pre-programmed thresholds. Hit patterns in the muon system and the Central Fiber Tracker (CFT) are examined to see if they are consistent with charged tracks above various transverse momentum thresholds. These tests take up to 3.5  $\mu$ s to complete, the equivalent of 27 beam crossings. Since ~10  $\mu$ s of deadtime for readout is incurred following a L1 trigger, we have set a maximum L1 trigger rate of 5 kHz.

The Level 2 trigger (L2) takes advantage of the spatial correlations and more precise detector information to further reduce the trigger rate. The L2 system consists of dedicated preprocessors, each of which reduces the data from one detector subsystem (calorimeter, muon, CFT, preshowers, and SMT). A global L2 processor takes the individual elements and assembles them into physics "objects" such as muons, electrons, or jets. The Silicon Track Trigger (STT) introduces the precise track information from the SMT to look for large impact parameter tracks from b quark decays. Some pipelining is necessary at L2 to meet the constraints of the 100  $\mu$ s decision time. L2 can accept events and pass them on to Level 3 at a rate of up to 1 kHz.

The Level 3 (L3) trigger consists of a farm of fast, high-level computers (PCs) which perform a simplified reconstruction of the entire event. Even within the tight time budget of 25 ms, this event reconstruction will allow the application of algorithms in the trigger with sophistication very close to that of the offline analyses. Events that satisfy desired characteristics will then be written out to a permanent storage medium. The maximum L3 output for Run 2a is 50 Hz and is largely dictated by downstream computing limits.

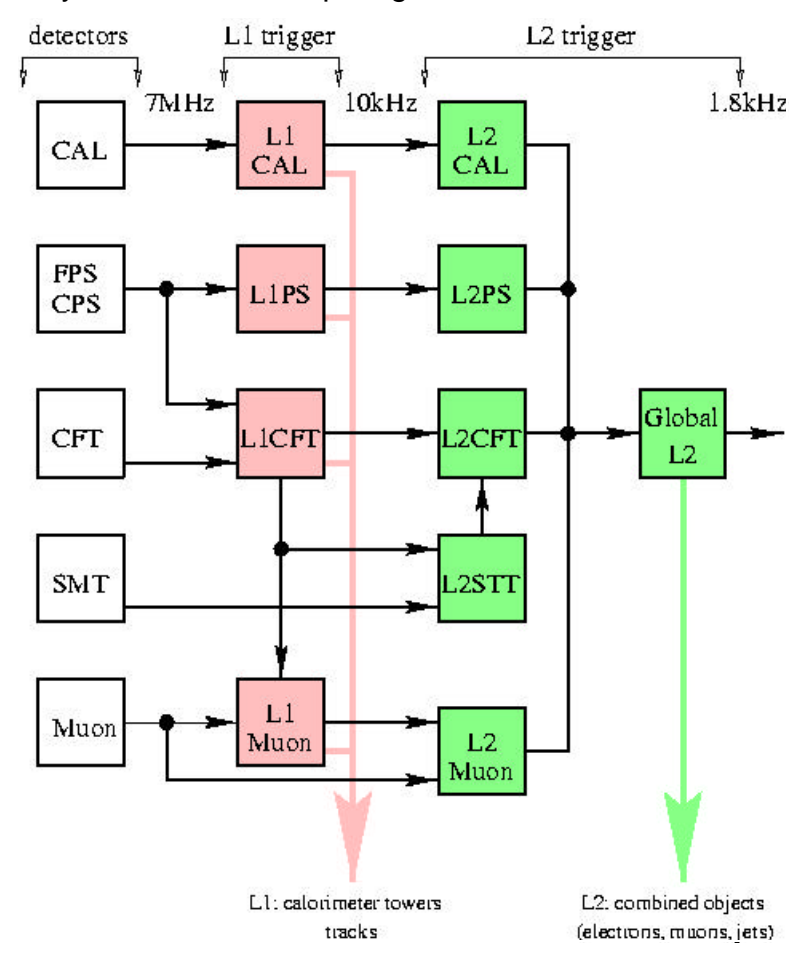


Figure 1. Block diagram of Level 1 and Level 2 triggers, indicating the individual trigger processors that comprise each level.

# 2.2 Leptonic Triggers

As mentioned above, leptons provide the primary means of selecting events containing W and Z bosons. They can also tag *b* quarks through their semileptonic decays, complementing the more efficient (but only available at Level 2 through the STT) lifetime selection. The impact of the purely leptonic tag is seen most strongly in the measurements of the W mass, the W and Z production cross sections, and the W width, since the events containing W and Z bosons are selected solely by requiring energetic leptons. The increased statistics provided by Run 2b should allow for a significant improvement in the

precision of these measurements, complementing the direct searches in placing more stringent constraints on the Standard Model.

In addition to their inherent physics interest, leptonic signals will play an increasingly important role in the calibration of the energy and momentum scales of the detectors, which is crucial for the top quark and W mass measurements. This will be accomplished using  $Z\rightarrow e^+e^-$ ,  $Y\rightarrow e^+e^-$ , and  $J/\Psi\rightarrow e^+e^-$  for the electromagnetic calorimeter energy scale and the corresponding muon decays for the momentum scale. Since the trigger bandwidth available for acquiring calibration samples must be non-zero, another set of constraints is imposed on the overall allocation of trigger resources.

## 2.3 Leptons plus Jets

During Run I, lepton-tagged decays of the W bosons and b quarks played an essential role in the discovery of the top quark and were exploited in the measurements of the top mass and production cross section. The new capability provided by the STT to tag b quark decays on-line will allow the collection of many thousands of  $t\bar{t}$  pairs in the channel  $t\bar{t}\to 1\, v+{\rm jets}$  with one b-tagged jet. This will be sufficient to allow the study of top production dynamics as well as the measurement of the top decay branching fractions. This was also the most precise channel used in the measurement of the top mass in Run I - the increase in statistics will allow the reduction of several key systematic errors for this channel as well as for the channel  $t\bar{t}\to 1\, v1' v+{\rm jets}$ . One of these, the uncertainty in the jet energy scale, can be reduced by understanding the systematics of the direct reconstruction of W or Z boson decays into jets. The most promising channel in this case is the decay  $Z\to b\bar{b}$ , in which on-line b-tagging can provide the needed rejection against the dominant two-jet background.

### 2.4 Leptons/Jets plus Missing E<sub>T</sub>

As mentioned above, events containing multiple leptons and missing energy are often referred to as the "gold-plated" SUSY discovery mode. These signatures, such as three leptons plus missing energy, were explored in Run I to yield some of the most stringent limits on physics beyond the Standard Model. These investigations will be an integral part of the search for new physics in Run II. Missing energy is characteristic of any physics process where an invisible particle, such as an energetic neutrino or a massive stable neutral particle, carries away a large fraction of the available energy. As such, missing energy combined with leptons/photons or jets can be a manifestation of the presence of large extra dimensions, different SUSY configurations, or other new physics beyond the Standard Model.

### 2.5 Triggers for Higgs Searches

One of the primary goals of the Run 2b physics program will be to exploit the delivered luminosity as fully as possible in search of the Higgs mechanism up to the highest accessible Higgs masses. Since even a delivered luminosity of 15fb<sup>-1</sup> per experiment may not lead to a statistically significant discovery, the emphasis will be on the combination of as many decay channels and production

mechanisms as possible. For the trigger, this implies that flexibility, ease of monitoring, and selectivity will be critical issues.

Coverage of the potential window of discovery is provided by the decay channel  $H \to b \overline{b}$  at low masses, and by  $H \to W^{(*)}W$  at higher masses. In the first case, the production mechanism with the highest sensitivity will probably be in the mode  $p\overline{p} \to WH$ . For leptonic W decays, the leptons can be used to tag the events directly. If the W decays hadronically, however, the four jets from the  $q\overline{q}\,b\overline{b}$  final state will have to be pulled out from the large QCD backgrounds. Tagging b jets on-line will provide a means to select these events and ensure that they are recorded. Of course, three or four jets with sufficient transverse energy are also required. Another decay mode with good sensitivity is  $p\overline{p} \to ZH$ , where the Z decays to leptons, neutrinos, or hadrons. From a trigger perspective, the case where the Z decays hadronically is identical to the WH all-hadronic final state. The final state  $ZH \to n\overline{n}\overline{b}b$ , however, provides a stringent test for the missing  $E_T$  trigger, since the final state is only characterized by two modest b jets and missing energy.

Recently, the secondary decay mode H  $\to \tau^+ \tau^-$  has come under scrutiny as a means of bolstering the statistics for Higgs discovery in the low mass region. A trigger that is capable of selecting hadronic tau decays by means of isolated, stiff tracks or very narrow jets may give access to the gluon-fusion production mode gg  $\to$  H  $\to \tau^+ \tau^-$  for lower Higgs masses. This mode can also be important in some of the large tan $\beta$  SUSY scenarios, where the Higgs coupling to  $b\bar{b}$  is reduced, leaving H  $\to \tau^+ \tau^-$  as the dominant decay mode for the lightest Higgs.

The higher Higgs mass regime will be covered by selecting events from  $p\overline{p} \to \mathsf{H} \to \mathsf{W}^{(\star)}\mathsf{W}$  with one or two high-energy leptons from the  $\mathsf{W} \to \mathsf{l}\,\mathsf{v}$  decay. This decay mode thus requires a trigger on missing  $\mathsf{E}_\mathsf{T}$  in addition to leptons or leptons plus jets.

## 2.6 Trigger Menu and Rates

As even the previous cursory review makes clear, the high- $p_T$  physics menu for Run 2b requires efficient triggers for jets, leptons (including taus, if possible), and missing  $E_T$  at Level 1. The STT will be crucial in selecting events containing b quark decays; however, its rejection power is not available until Level 2, making it all the more critical that the Level 1 system be efficient enough to accept all the events of interest without overwhelming levels of backgrounds.

In an attempt to set forth a trigger strategy that meets the physics needs of the experiment, the Run II Trigger Panel suggested a preliminary set of Trigger Terms for Level 1 and Level 2 triggers<sup>1</sup>. In order to study the expected trigger rates for various physics processes, many of these terms have been implemented into the Run 2 Trigger Simulation. While the results are still

\_

<sup>&</sup>lt;sup>1</sup> The report of the Run II Trigger Panel can be found at http://www-d0fnal.gov/trigger\_meister/private/www.

preliminary, the overall trend is very clear. The simple triggers we have currently implemented at Level 1 for Run2a will not be able to cope with the much higher occupancies expected in Run2b without a drastic reduction in the physics scope of the experiment and/or prescaling of important physics triggers. Our studies have focused on various QCD jets samples in order to determine the effects of many low-p<sub>T</sub> minimum bias events superimposed on the dominant processes. In a sample of jet events where the jet spectrum includes jets down to a  $p_T$  of 2 GeV, for example, a high-p<sub>T</sub> electron/photon trigger requiring a 10 GeV electromagnetic tower in the central calorimeter has essentially zero rate at a luminosity of 3.8x10<sup>31</sup> cm<sup>-2</sup>s<sup>-1</sup>; this rate at 5x10<sup>32</sup> cm<sup>-2</sup>s<sup>-1</sup> is 5.4 kHz, which exceeds the Level 1 trigger bandwidth. A di-electron or di-photon trigger requiring a 10 GeV electromagnetic tower in the central region and a 5 GeV electromagnetic tower in the calorimeter endcaps is expected to reach a rate of 2.7 kHz at a luminosity of 5x10<sup>32</sup> cm<sup>-2</sup>s<sup>-1</sup>. A two-track trigger requiring one track with a p<sub>T</sub> greater than 10 GeV with a total of two tracks above 5 GeV reaches an expected rate of 10 kHz. Even given the uncertainties in the simulation of multiple interactions, these results suggest that the current Level 1 trigger system will not function as desired in the high-occupancy, high-luminosity Run 2b environment.

We now turn to discussions of potential upgrades to the trigger system in order to cope with the large luminosities and occupancies of Run 2b.

# 3 Level 1 Tracking Trigger

The Level 1 Central Tracking Trigger (CTT) plays a role in the full range of L1 triggers. In this section, we outline the goals for the CTT, describe the implementation and performance of the present track trigger, and examine three options for upgrading the CTT.

### 3.1 Goals

The goals for the CTT include providing track triggers, combining tracking and preshower information to identify electron and photon candidates, and generating track lists that allow other trigger systems to perform track matching. We briefly discuss these goals below.

### 3.1.1 <u>Track Triggers</u>

The CTT provides various Level 1 trigger terms based on counting the number of tracks whose transverse momentum ( $p_T$ ) exceeds a threshold. Track candidates are identified in the axial view of the Central Fiber Tracker (CFT) by looking for hits in all 8 layers within predetermined roads. Four different sets of roads are defined, corresponding to  $p_T$  thresholds of 1.5, 3, 5, and 10 GeV, and the number of tracks above each threshold can be used in the trigger decision. For example, a trigger on two high  $p_T$  tracks could require two tracks with  $p_T > 5$  GeV and one track with  $p_T > 10$  GeV.

Triggering on isolated tracks provides a complementary approach to identifying high-p<sub>T</sub> electron and muon candidates, and is potentially useful for

triggering on hadronic tau decays. To identify isolated tracks, the CTT looks for additional tracks within a  $12^{\circ}$  region in azimuth ( $\phi$ ).

### 3.1.2 <u>Electron/Photon Identification</u>

Electron and photon identification is augmented by requiring a significant energy deposit in the preshower detector. The Central Preshower (CPS) and Forward Preshower (FPS) detectors utilize the same readout and trigger electronics as the fiber tracker, and are included in the discussion of tracking triggers. Clusters found in the axial layer of the CPS are matched with track candidates to identify electron and photon candidates. Clusters found in the FPS are also used to help identify electron/photon candidates, but cannot be matched with tracks.

## 3.1.3 <u>Track Matching</u>

Track candidates found in the CTT are utilized in several other trigger systems.

The Level 1 muon trigger matches CTT tracks with hits in the muon detector. To meet timing requirements, the CTT tracks must arrive at the muon trigger on the same time scale as the muon proportional drift tube (PDT) information becomes available.

The current Level 1 trigger allows limited azimuthal matching of tracking and calorimeter information at the quadrant level. Significantly increasing the flexibility and granularity of the calorimeter track matching is under consideration for Run 2b (see the Level 1 Calorimeter Trigger section). This option would require sending track lists to the calorimeter trigger.

The L2 Silicon Track Trigger (STT) uses tracks from the CTT to generate roads for finding tracks in the Silicon Microstrip Tracker (SMT). The precision of the SMT measurements at small radius, combined with the larger radius of the CFT, allows displaced vertex triggers, sharpening of the momentum thresholds for track triggers, and elimination of fake tracks found by the CTT. The momentum spectra for b-quark decay products to low  $p_T$ . The CTT therefore aims to provide tracks extending down to the lowest  $p_T$  possible. The Run 2a CTT generates track lists down to  $p_T \approx 1.5$  GeV. The CTT tracks must also have good azimuthal  $(\phi)$  resolution to minimize the width of the road used by the STT.

In addition to the track lists sent to the STT, each portion of the L1 track trigger (CFT, axial CPS, and FPS) provides information for the Level 2 trigger decision. The stereo CPS signals are also sent to L2 to allow 3-D matching of calorimeter and CPS signals.

## 3.2 Description of Current Tracking Trigger

This section describes the architecture of the Run 2a track trigger.

### 3.2.1 Tracking Detectors

The CFT is made of scintillating fibers mounted on eight low mass cylinders. Each of these cylinders supports four layers of fibers arranged into two doublet

layers. The innermost doublet layer on each cylinder has its fibers oriented parallel to the beam axis. These are referred to as Axial Doublet layers. The second doublet layer has its fibers oriented at a small angle to the beam axis. These are referred to as Stereo Doublet layers. Only the Axial Doublet layers are incorporated into the current L1 CTT. Each fiber is connected to a visible light photon counter (VLPC) that converts the light pulse to an electrical signal.

The CPS and FPS detectors are made of scintillator strips with wavelengthshifting fibers threaded through each strip. The CPS has an axial and two stereo layers outside mounted on the outside of the solenoid. The FPS has two stereo layers in front of a lead radiator and two stereo layers behind the radiator. The CPS/FPS fibers are also readout using VLPCs.

# 3.2.2 CTT Segmentation

The CTT is divided in  $\phi$  into 80 Trigger Sectors (TS). A single TS is illustrated schematically in Figure 2. To form a track, information is needed from a TS, called the home sector, and from each of its two neighboring trigger sectors. The TS is sized such that the tracks satisfying the lowest  $p_T$  threshold (1.5 GeV) is contained within a single TS and its neighbors. A track is 'anchored' in the outermost (H) layer. The  $\phi$  value assigned to a track is the fiber number at the H layer. The  $p_T$  value for a track corresponds to the intercept of the track on the innermost (A) layer.

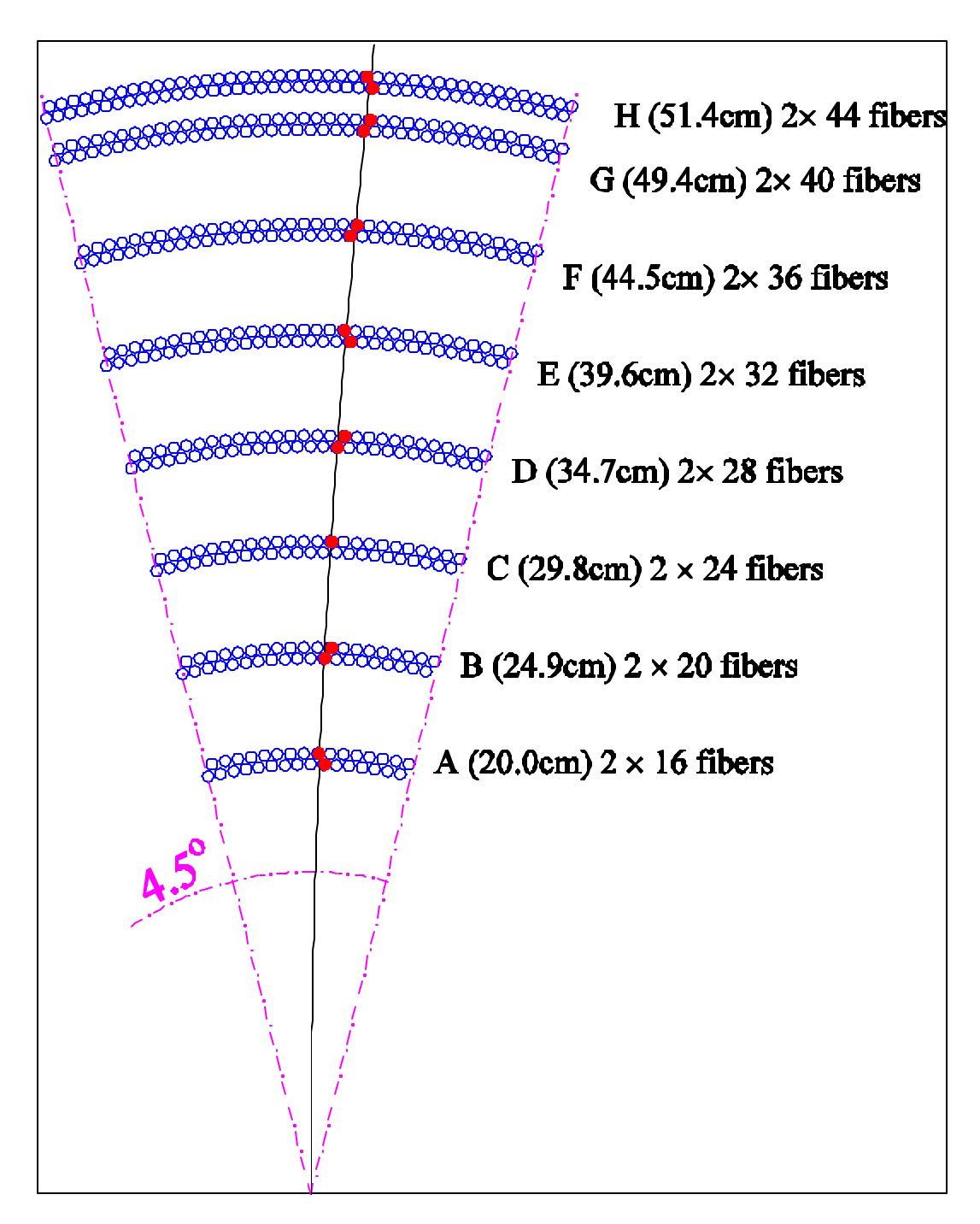


Figure 2. Illustration of a CTT trigger sector and the labels assigned to the eight CFT cylinders. Each of the 80 trigger sectors has a total of 480 axial fibers.

The home sector contains 480 axial fibers. A further 368 axial fibers from 'next' and 'previous' sectors are sent to each home sector to find all the possible axial tracks above the  $p_T$  threshold. In addition, information from 16 axial scintillator strips from the CPS home sector and 8 strips from each neighboring sector are included in the TS for matching tracks and preshower clusters.

### 3.2.3 CTT Electronics

The tracking trigger hardware has three main functional elements. The first element is the Analog Front-End (AFE) boards that receive signals from the VLPCs. The AFE boards provide both digitized information for L3 and offline analysis as well as discriminated signals used by the CTT. Discriminator thresholds should be set at a few photoelectrons for the CFT, and at the 5 – 10 MIP level for the CPS and FPS. Discriminator outputs for 128 channels are buffered and transmitted over a fast link to the next stage of the trigger. The axial layers of the CFT are instrumented using 76 AFE boards, each providing 512 channels of readout. The axial CPS strips are instrumented using 10 AFE boards, each having 256 channels devoted to axial CPS readout and the remaining 256 channels devoted to stereo CFT readout. The FPS is instrumented using 32 AFE boards.

The second hardware element is the Mixer System (MS). The MS resides in a single crate and is composed of 20 boards. It receives the signals from the AFE boards and sorts them for the following stage. The signals into the AFE boards are ordered in increasing azimuth for each of the tracker layers, while the trigger is organized into TS wedges covering all radial CFT/CPS axial layers within 4.5 degrees in  $\phi$ . Each MS board has sixteen CFT inputs and one CPS input. It shares these inputs with boards on either side within the crate and sorts them for output. Each board then outputs signals to two DFEA boards (described below), with each DFEA covering two TS.

The third hardware element is based on the Digital Front-End (DFE) motherboard. These motherboards provide the common buffering and communication links needed for all DFE variants and support two different types of daughter boards, single-wide and double-wide. The daughter boards implement the trigger logic using Field Programmable Gate Array (FPGA) chips. The signals from the Mixer System are received by 40 DFE Axial (DFEA) boards. There are also 5 DFES boards that prepare the signals from the CPS stereo layers for L2 and 16 DFEF boards that handle the FPS signals.

### 3.2.4 CTT Outputs

The current tracking trigger was designed to do several things. For the L1 Muon trigger it provides a list of found tracks for each crossing. For the L1 Track Trigger it counts the number of tracks found in each of four  $p_T$  bins. It determines the number of tracks that are isolated (no tracks in neighbor TS). The sector numbers for isolated tracks are recorded to permit triggers on acoplanar high  $p_T$  tracks. Association of track and CPS clusters provides the ability to recognize both electron and photon candidates. FPS clusters are categorized as electrons or photons, depending on an association of MIP and shower layer clusters. Finally, the L1 trigger boards store lists of tracks for each beam crossing, and the appropriate list is transferred to L2 processors when an L1 trigger accept is received.

The L1 CTT must identify real tracks within several  $p_T$  bins with high efficiency. The nominal  $p_T$  thresholds of the bins are 1.5, 3, 5, and 10 GeV. The

L1 CTT must also provide rejection of fake tracks (due to accidental combinations in the high multiplicity environment). The trigger must perform its function for each beam crossing at either 396 ns or 132 ns spacing between crossings. With the exception of the front end electronics, the system as constructed should accommodate both crossing intervals<sup>2</sup>.

A list of up to six found tracks for each crossing is packed into 96 bits and transmitted from each of the 80 trigger sectors. These tracks are used by the L1 Muon trigger and must be received within 1000ns of the crossing. These track lists are transmitted over serial copper links from the DFEA boards.

The L1 CTT counts the number of tracks found in each of the four pr bins. with subcategories such as the number of tracks correlated with showers in the Central Preshower Detector, and the number of isolated tracks. Azimuthal information is also preserved so that information from each  $\phi$  region can be correlated with information from other detectors. The information from each of the 80 TS is output to a set of 8 Central Tracker Octant Card (CTOC) boards, which are DFE mother boards equipped with CTOC type double wide daughter boards. During L1 running mode, these boards collect the information from each of 10 DFEA boards, combine the information and pass it on to a single CTTT board. The CTTT board, also a DFE type mother board equipped with a different double wide daughter board, assembles the information from the eight CTOC boards and reformats it for transmission to two Muon Trigger Manager (MTM) board. The MTM board, identical to that used in the muon trigger, prepares the trigger input terms that are used by the Trigger Framework in forming the L1 trigger decision. For example, the condition "TPQ(2,3)" indicates two tracks associated with CPS hits were present in quadrant 3. The Trigger Framework accommodates a total of 256 such conditions, feeding them into a large programmable AND/OR network that determines whether the requirements for generating a trigger are met.

The DFEA boards store lists of tracks from each crossing, and those lists are transferred to the L2 processors when an L1 trigger accept is received. A list of up to 6 tracks is stored for each  $p_T$  bin. When an L1 trigger accept is received, the normal L1 traffic is halted and the list of tracks is forwarded to the CTOC board. This board recognizes the change to L2 processing mode and combines the many input tracks lists into a single list that is forwarded to the L2 processors. Similar lists of preshower hits are maintained by the DFES and DFEF boards for the CPS stereo and FPS strips. These lists are also transferred to the L2 processors upon receiving an L1 trigger accept.

### 3.2.5 <u>Tracking Algorithm</u>

\_

The tracking trigger algorithm currently implemented is based upon hits constructed from pairs of neighboring fibers, referred to as a "doublet". Fibers in doublet layers are arranged on each cylinder as illustrated in Figure 3. In the first

<sup>&</sup>lt;sup>2</sup> Work is in progress to upgrade the AFE boards to AFE2 versions that will support operation at 132 ns crossings.

stage of the track finding, doublet layer hits are formed from the individual axial fiber hits. The doublet hit is defined by an OR of the signals from adjacent inner and outer layer fibers in conjunction with a veto based upon the information from a neighboring fiber. In Figure 3, information from the first fiber on the left on the upper layer would be combined by a logical OR with the corresponding information for the second fiber from the left on the lower layer. This combination would form a doublet hit unless the first fiber from the left on the lower layer was also hit. Without the veto, a hit in both the first upper fiber and the first lower fiber would result in two doublet hits.

# **Doublet Layer**

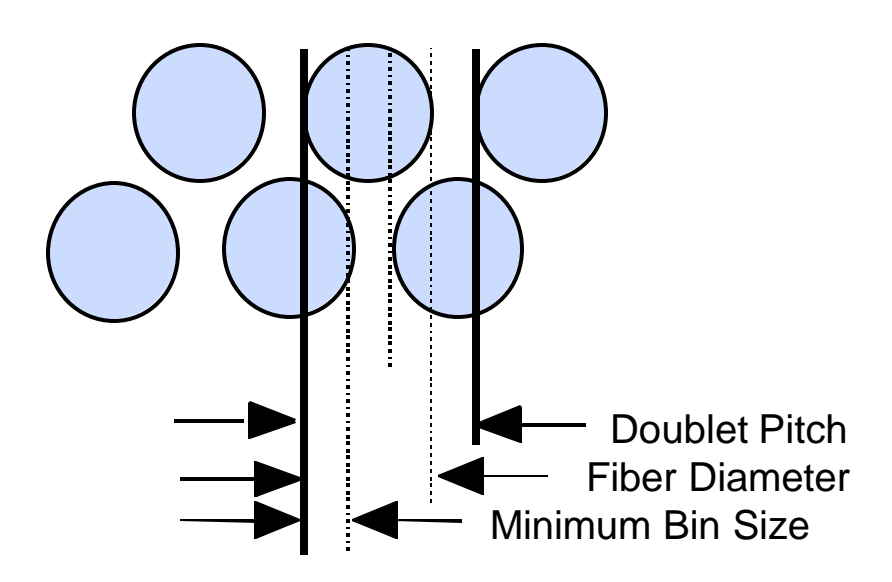


Figure 3. Sketch illustrating the definition of a fiber doublet. The circles represent the active cross sectional areas of individual scintillating fibers. The boundaries of a doublet are shown via the thick black lines. The dashed lines shown the four distinguishable regions within the doublet.

The track finding within each DFEA board is straightforward. Each daughter board has 4 large FPGA chips, one for each of the four  $p_T$  bins. Within each chip the track roads are represented by equations which correspond to a list of which doublets can be hit for a track with a given  $p_T$  and  $\phi$ . For each possible road the eight fibers for that road are combined into an 8-fold-AND equation. If all the fibers on that road were hit then all 8 terms of the AND are TRUE and the result is a TRUE. The FPGA chips are loaded with the equations for all possible real tracks in each sector in each  $p_T$  range. Each TS has 44  $\phi$  bins and 24 possible  $p_T$  bins and in addition about 12 different routes through the intermediate layers. This results in about 12K equations per TS.

The individual track results are then OR'ed together by  $\phi$  bin and sorted by p<sub>T</sub>. Up to six tracks per TS are reported out to the trigger. This list of 6 tracks is then sent to the fifth or backend chip on the daughter board for all the remaining functions.

The FPGA chips have a very high density of gate logic which lends itself well to the track equations. Within these chips all 12k equations are processed simultaneously in under 200 ns. This design also keeps the board hardware as general as possible. The motherboard is simply an I/O device and the daughter boards are general purpose processors. Since algorithms and other details of the design are implemented in the FPGA, which can be reprogrammed via high level languages, one can re-download different triggers configurations for each run or for special runs and the trigger can evolve during the run.

## 3.3 Fiber Tracker Trigger Operation at 132 ns bunch spacing

DØ currently uses a special trigger chip to provide a hardware trigger for the Central Fiber Tracker. This chip is called the SIFT chip, and is housed within Multi-Chip Modules (MCM) that are mounted on the Analog Front End (AFE) boards. The SIFT lies upstream of the SVX2 chip, and downstream of the VLPCs, in the CFT readout chain. It provides 16 channels of discriminator output before transferring the charge to the input of SVX2. In order for the CFT to perform with an efficiency that is adequate for addressing our physics needs, studies have shown that charge collection times of 50 to 70 ns are needed. The performance of the current SIFT chip is marginal at 132 ns with charge collection times of this duration. We are therefore pursuing a modified version of the SIFT chip that will appropriately address this deficiency. We believe this is needed in order to adequately pursue the relevant Run 2 physics goals during 132 ns accelerator operation.

The technical approach DØ has initiated to address this consists of an effort to design a replacement for the current Multi-Chip Modules mounted on the AFE boards. The MCMs will be replaced with a small daughter board that uses one custom integrated circuit (IC), a commercially available ADC, and an FPGA. Each of these boards would accommodate 64 fiber inputs, providing discriminated digital outputs for the trigger and digitized pulse heights for readout. We believe this design represents a simplification of the present version, and expect it to perform adequately during 132ns crossing operation. More details are described in subsequent paragraphs below.

### 3.3.1 Introduction

The new SIFT design will have to have excellent noise performance and threshold uniformity for the CFT, as well as sufficient dynamic range and adequate energy resolution for the preshowers (CPS/FPS). While it is possible to replace only the chips housed within the Multi-Chip Modules (MCM), we feel that this is a high-risk solution from both the design point of view - where very high speed, bw noise operation of the current MCM is required - and from the manufacturing/production point of view, where very high yields are necessary in order to contain the cost. We are therefore pursuing a full replacement of the

current MCM with a standard printed circuit daughter board. This board will have mounted on it a series of new elements that will functionally replace the current SIFT chip: the Trigger and Pipeline chip (the TriP chip), a high speed ADC for analog readout, and a Field Programmable Gate Array (FPGA) to buffer the data and emulate the current SVX2 chip during readout. Our default design is one in which the daughter board would carry the new custom IC and a few standard chips; the AFE motherboard would not be redesigned or refabricated. We are also considering a version in which the new components would be mounted directly on the AFE board without the need of a daughter board. For this option, the TriP chip would have to be packaged - for example, in a standard thin quad flat pack (TQFP). New AFE boards would also have to be manufactured. Although this latter option would allow for a far simpler AFE motherboard design with reduced functionality compared to the present version, it would require a new layout and production cycle, and would therefore be more costly than our current baseline design. A preliminary outline of the costs of these two options, along with sub-project milestones and remarks on the current status, is given in Table 1 and Table 2 at the end of this section.

### 3.3.2 SIFT Replacement: the TriP ASIC

This TriP chip will be a custom IC manufactured in the TSMC 0.25 micron process and will be powered from a 2.5V to 3V supply. The new chip is simple in concept and design, and is based on several already-existing sub-designs of other chips. It would replace the four SIFT chips on the current MCMs with a single 64 channel chip that performs the two functions required: first, it provides the trigger output for every channel above a preset threshold, and second, it provides a pipeline delay so that analog information is available for channels above threshold if the trigger system determines that the event should be read out (a Level 1 accept). The rest of the devices on the daughter board are readily available commercial parts.

### 3.3.2.1 Amplifier/ Discriminator

Because of the possibility of large signals being generated within the detectors for readout, the preamplifier needs to be reset after every crossing. The input charge range is 4 to 500 fC. Since this device will be used in both the fiber tracker and preshower detectors - and the preshower detector will, for high energy electrons, produce signals that are as much as 16 times larger than the fiber tracker - the preamplifier will have programmable gain. Four binary weighted capacitors that can be switched into the feedback loop of the amplifier will provide the desired flexibility for setting the gain range.

The discriminator will be set as a fraction of the selected full range of the preamp. It will be digitally controlled and have approximately 8 bits of resolution. The discriminators will be uniform across the chip to 1%. The chip will include a provision for test inputs to allow a\_known amount of charge to be injected into selected channels. The input will be AC coupled and will present a capacitive load of 30 to 40 pF. Signal rise time of the VLPC is less than 600 ps, so rise time

at the input is entirely determined by the input capacitance. The chips will collect 95% of the signal charge in 50 to 75ns.

There are 64 bits of discriminator information that must be sent from the MCM to the trigger system every crossing. Because the preamp is required to reset every crossing and the charge collection time is less than 75ns, it is possible to send the discriminator bits only during the time the preamp is inactive. Furthermore, if the discriminator outputs are multiplexed by a factor of two in an effort to reduce the number of lines required, the switching frequency of the discriminator bits is still manageable: lines may switch at a maximum frequency of once every 25ns, but only during the time the preamp is being reset. The discriminators would be sent to the FPGA on the same daughter board only a few centimeters away and would require only about 1/15 of the energy of the present design.

## 3.3.2.2 Pipeline and Mux

The TriP chip will use the pipeline designed for the SVX4 chip being designed for the silicon detector for Run 2b, including the on-chip bypass capacitors. This is a 47-deep pipeline and is adequate for this application. Only minimal modifications will be required to match the full-scale output of the preamp. The 64 channels will be multiplexed out onto an external bus, which will be connected to a commercial Analog to Digital Converter (ADC). It is possible to fit two dual input 10 bit ADCs on to the daughter board: this will allow the analog outputs to work at 7.6Mhz with four 16-to-1 multiplexors on the TriP chip.

# 3.3.3 <u>High Speed ADC</u>

This ADC being used here is a commercially available, 10 bit, dual input device with impedance inputs and less than 10 pF input capacitance. The device is capable of 20 million samples per second (MSPS) but will run at a frequency of only 7.6 MSPS. With two ADCs per daughter board, the time required to digitize 64 channels is 2.2  $\mu$ s, which is approximately the same duration as the digitization time of the SVX II chip. The digital outputs of the ADCs will be connected to a small FPGA on the daughter board for further processing before readout. At least two component parts from different manufacturers are available that meet all the design requirements related to power needs and consumption, space, speed, performance and cost.

### 3.3.4 FPGA

Field Programmable Gate Arrays have developed rapidly in the last few years. A small FPGA placed on the daughter board is able to provide the processing power and speed to emulate an SVXII, the necessary data storage for buffering the discriminator information during the trigger latency time, and sufficiently flexible I/O to provide level translation and control functions.

The FPGA is connected to both the TriP chip and the ADCs on the daughter board. It also interfaces with the SVX bus and the trigger data path. The FPGA senses the MODE lines of the SVX bus to control the rest of the devices on the daughter board. During ACQUIRE mode, the TriP chip will output the

discriminator information on 32 lines during a part of the crossing using LVCMOS2 or similar signal levels (2 bits per line, time-multiplexed.) The FPGA will latch the 64 bits, add 7 bits of status information, and repackage the bits into 10-bit-wide packets that will be sent to the motherboard at 53Mhz and then passed on to the LVDS drivers. At the same time, the discriminator bits will be stored in the FPGA-embedded RAM blocks so the information is available for readout to the offline system. Even a small FPGA, such as the Xilinx XC2S30, has 24KB of block RAM - much more than is required to implement a 32-stage digital pipeline for the 64 trigger bits. However, the RAM will be used for other purposes as well. Once a L1 accept signal is received, the SVX bus will change from the ACQUIRE mode to the DIGITIZE mode. The FPGA would sense this mode change, stop the analog pipeline inside the TriP chip, and start the analog multiplexors and the ADCs. The FPGA would collect the digital data from the ADCs; reformat the 10 bits into a floating-point format, and temporarily save it in RAM, pending readout. Once the READOUT phase starts, the FPGA would emulate the SVX functionality by generating the chip ID, status and channel ID, and retrieving the discriminator and analog information from the on-chip RAM and putting it on the SVX bus.

### 3.3.5 Preliminary Cost Estimate

As mentioned above, there are a few options for replacement of the SIFT: 0) One can replace only the SIFT within existing MCMs. The technical risks are potentially serious enough in this option that we do not further consider it here. 1) One can replace the MCM with new daughter boards. In this option, the TriP chip can be used in bare-die form by wirebonding it directly onto the daughter board, or in packaged form prior to mounting it on the daughter cards. The current AFE boards would be used in this option, but the existing MCMs would have to be removed and the boards restuffed with the new daughter cards. There is some technical risk associated with MCM removal that, though still something of a concern, has been tested and appears to be surmountable. 2) The AFE boards can be redesigned to accommodate directly mounting the TriP chip. In this version, the daughter boards would not be needed, and the TriP must be packaged. The space on the AFE board that would be needed for the redesigned SIFT would be exactly the same as the area occupied by the daughter board mounted on the existing AFE board in option 1. The rest of the AFE replacement board could use the same layout and components as those in the present version. There would be some engineering effort required to design and layout the new AFE, but these changes consist of relatively straightforward modifications to the present design. We estimate the cost for each of the options in Table 1 below.

The current plan for the TriP submission (ASIC) takes advantage of a concurrent submission of a similar chip already being planned and paid for by the Laboratory in conjunction with the BTeV experiment. At the moment, the expectation is that DØ will fabricate the TriP chip on the tail end of this run in order to save the cost that would be associated with an additional fabrication

phase. This should yield more parts than are needed for the SIFT project if they function as expected.

Table 1: Preliminary cost estimate for the SIFT replacement. Total cost for the baseline option (1) and the AFE replacement option (2) are shown (see text for details). Estimated cost for outside engineering known to be required for layout work is included. Additional manpower is not included.

		M&S			Cont	tingency		
Item	•		number	Unit cost	M&S		Cost	Total
					Total			
#	Description	unit	(incl.	(\$)	(\$K)	%	(\$K)	Cost
			spares)					
1	New parts	MCM	2000	40	80	50	40	120
	(FPGA, ADCs,							
	etc.)							
2	Replacement	Ea	2000	150	300	50	150	450
	daughter							
	boards							
3	TriP ASIC	Ea	2200	15	33	50	16.5	49.5
	packaging							
4	New AFE	Ea	240	1,500	360	50	180	540
	motherboards							
5	TriP ASCI	Lot	1	185,000	(185)			Not incl
	(see notes)							
6	Layout	Lot	1	30,000	30	100	30	60
	Engineering							
1,2,5,6	Option 1	Total cos	st (TriP ASI	C not incl.)	\$410k			\$630k
1,3,4,5,6	Option 2	Total cos	st (TriP ASI	C not incl.)	\$503k			\$770k

### 3.3.6 Milestones

We present below in Table 2 a series of milestones that have been extracted from a preliminary schedule for the SIFT replacement. This schedule is in the process of being more fully developed. It assumes two rounds of daughter board prototypes and two rounds of ASIC submissions for the TriP chip.

Table 2: Preliminary milestones for the SIFT replacement project.

1	1-Sep-01	Prototype daughter board available
2	15-Oct-01	AFE-daughter board integration demonstrated
3	20-Dec-01	TriP ASIC submitted to fab
4	10-Jan-02	Pre-production daughter board submitted for manufacture
5	15-Apr-02	AFE operation at 132ns demonstrated
6	15-Jun-02	Second ASIC submission
7	15-Jul-02	Daughter boards submitted for production
8	1-Oct-02	Final ASIC available (diced and tested)
9	20-Dec-02	Daughter boards ready for mounting on AFE

An analog engineer experienced in chip design from the Electrical Engineering Department in the Particle Physics Division at Fermilab has been working on the design of the TriP chip since early summer, 2001. The September 1 milestone, by which a prototype daughter board was to be made available, was met. The next critical date is the initial submission of the TriP chip on December 20, 2001. Work is progressing at a rate consistent with meeting this milestone. The December 20, 2002 end date is still roughly consistent with the latest plan for the changeover of the accelerator to accommodate 132 ns running. However, the schedule contingency is small, and efforts are underway to identify means by which portions of the project might be accelerated. We note that the schedule shown assumes two ASIC submissions – this may in fact prove to be unnecessary, and therefore might prove to be one source of schedule contingency for future use.

We note that a review of the SIFT replacement project was organized by the Run 2b Project Management, and took place on Tuesday, September 25, 2001. The Review Committee consisted of three Fermilab engineers (from outside DØ), and two DØ physicists. As of this writing, a report of their findings is being drafted for submission to the DØ Technical Manager (J. Kotcher). The charge to the committee can be made available upon request.

## 3.4 Performance of Current Tracking Trigger

It is intended that the current version of the DØ track trigger will be optimized for the data taking conditions that will occur during Run 2a. Under such conditions the current track trigger performs very well. From looking at a sample of muons simulated in Monte Carlo, with  $p_T > 50$  GeV/c, it was found that 97 % of the muons were reconstructed correctly; of the remaining 3%, 1.9 % of the tracks were not reconstructed at all and 1.1 % were reconstructed as two tracks due to detector noise (as the background in the CFT increases, due to overlay events,

we expect this latter fraction to get progressively higher). Since the data taking environment during Run 2b is expected to be significantly more challenging, it is important to characterize the anticipated performance of the current trigger under Run 2b conditions.

In order to test the expected behavior of the current trigger in the Run 2b environment, the current trigger simulation code was used with high levels of overlaid minimum bias interactions. The minimum bias interactions used in this study were generated using the **ISAJET** Monte Carlo generator according to the prescription described in the next section. As illustrated in the following section, this type of Monte Carlo overlay gives the worst case scenario for the Run 2b tracking trigger.

Figure 4 shows the rate at which a tracking trigger requiring two tracks with more than 10 GeV transverse momentum is satisfied as the luminosity, and thus the number of underlying minimum bias interactions, increases. During Run 2b, it is anticipated that the mean number of underlying interactions will be about 5, and Figure 4 shows that a tracking trigger rate for the current version of the trigger is expected to rise dramatically due to accidental hit combinations yielding fake tracks. This results in an increasingly compromised tracking trigger.

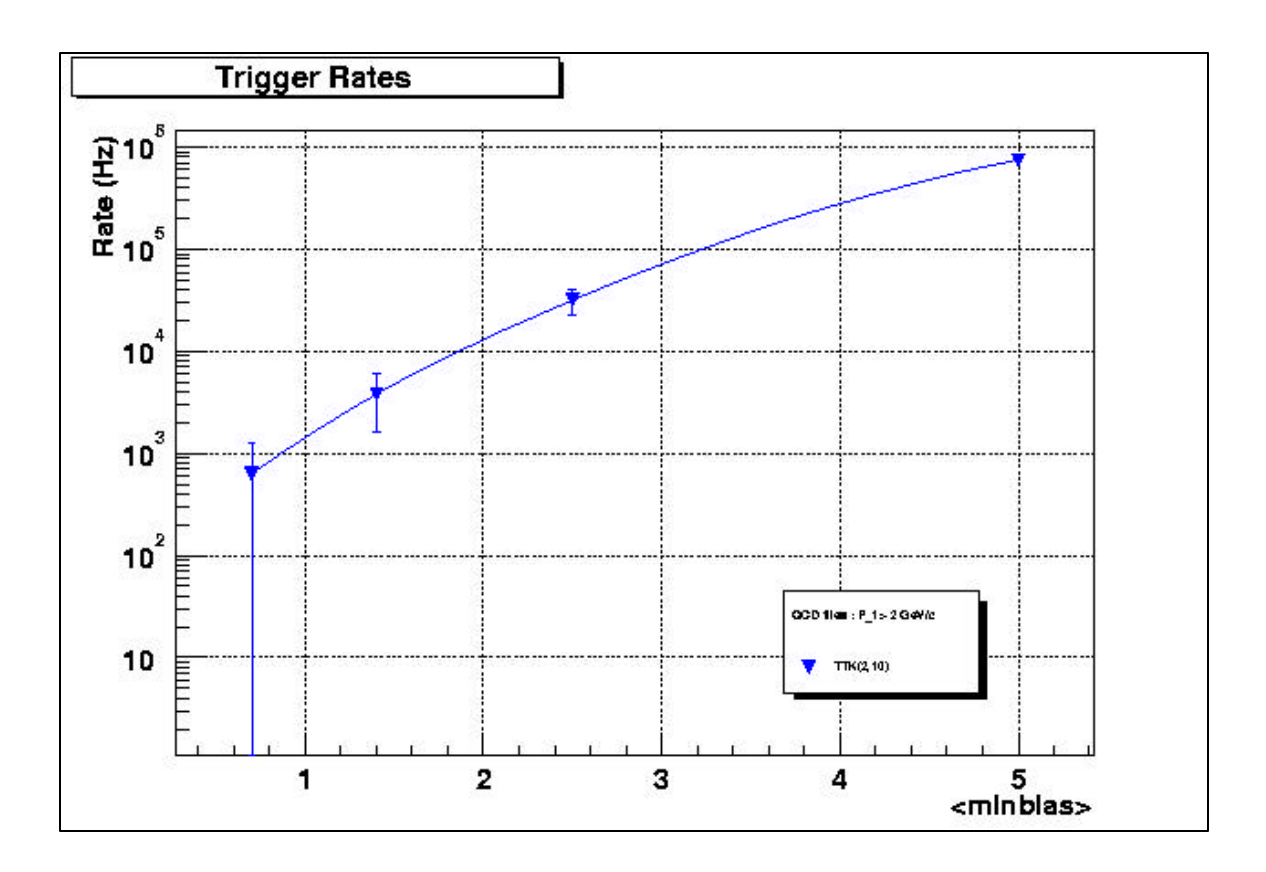


Figure 4. Tracking trigger rate as a function of the number of underlying minimum bias interactions. TTK(2,10) is a trigger requiring 2 tracks with transverse momentum greater than 10 GeV.

Figure 5 shows that the probability that various tracking trigger requirements will be satisfied in a given crossing is strongly dependent upon the number of underlying minimum bias interactions. These studies indicate that a stand-alone track trigger based upon the current hardware will be severely compromised under Run 2b conditions.

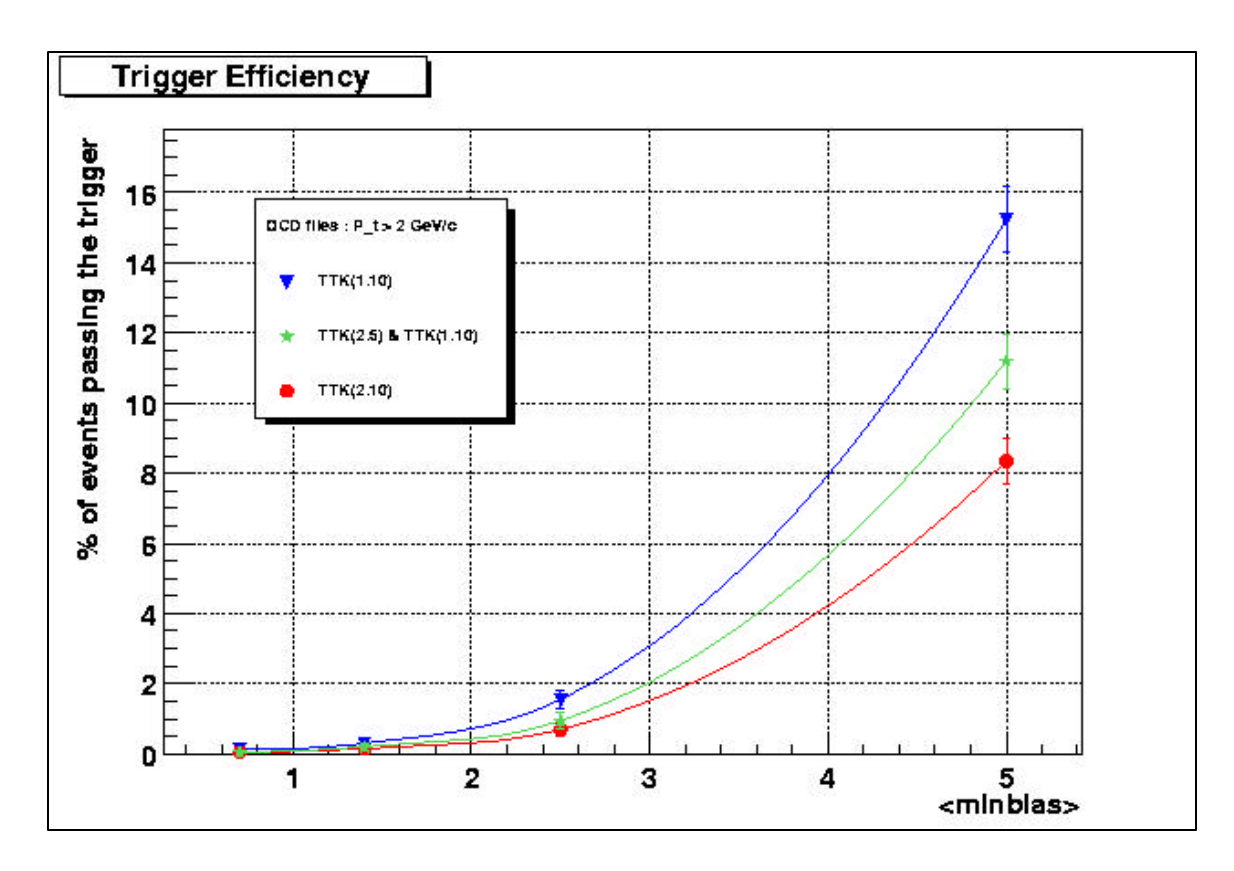


Figure 5. This plot shows the probability for minbias overlays to satisfy several Run 2a track trigger requirements as the luminosity increases.  $TTK(n,p_T)$  is a trigger requiring n tracks with transverse momentum greater than  $p_T$ .

In order to investigate these effects further, we looked at a sample of W events, where the W decays to  $\mu\nu.$  These are representative of a class of physics events that theoretically could be selected using a pure track trigger. We found a substantial number of fakes tracks that generated a track trigger, as expected given the previous results. But we observed that the rate for these fakes was strongly related to the CFT activity in the sectors where they were found. This effect is clearly illustrated in Figure 6, which shows how the fake rate varies with the number of doublets hit in a sector.

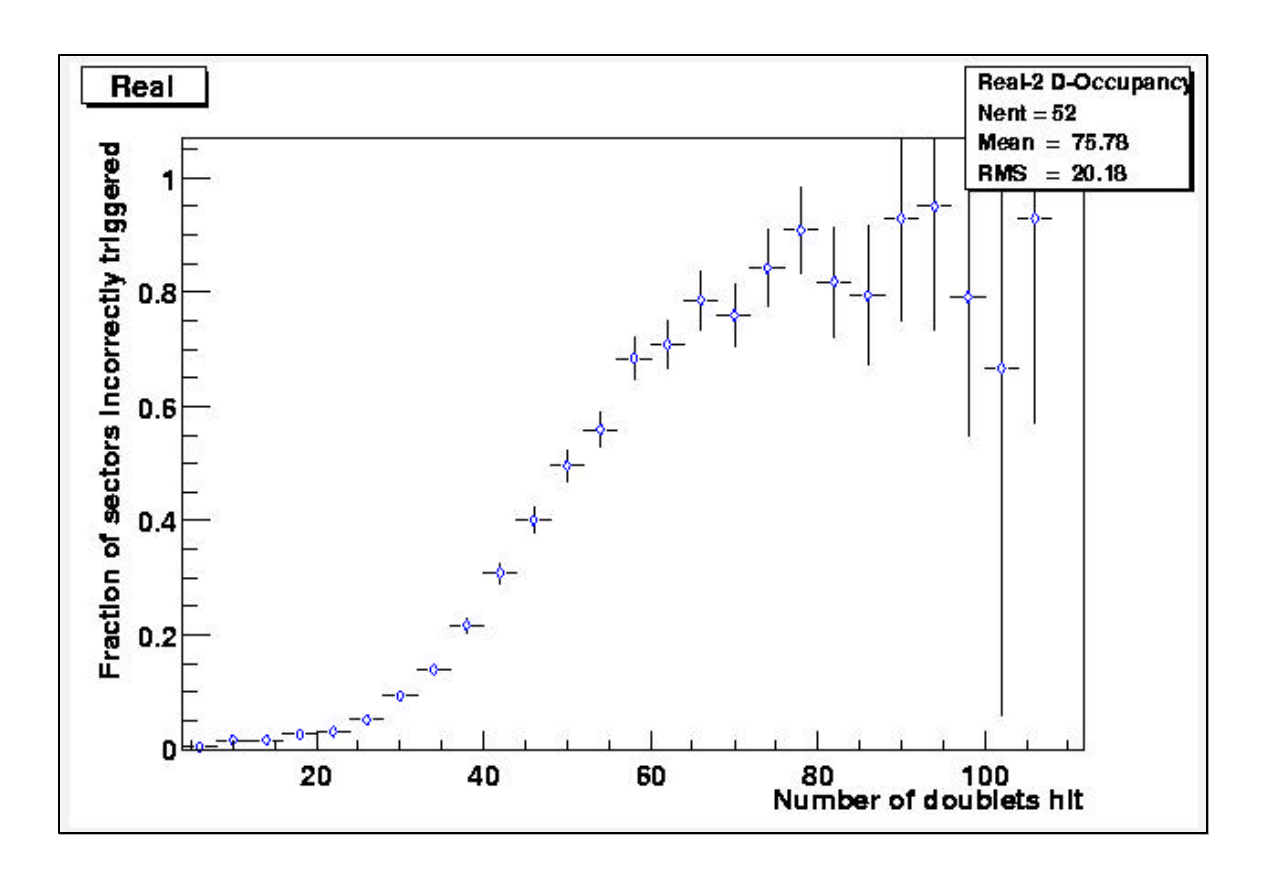


Figure 6. This graph shows the fake rate vrs fiber doublets hit, for W  $\rightarrow \mu \nu$  physics events, when we trigger on  $p_T > 5$  GeV/c tracks. The plot shows the clear impact of the doublet occupancy rate on the fake trigger rate, which rises dramatically as the sector of interest becomes "busier". The events used in this constructing this graph were generated using the PYTHIA Monte Carlo generator, and included a Poisson distribution of overlaid minimum bias interactions with a mean of 7.5 minimum bias interactions.

It is feasible that the strong dependency between the fake rate and the sector doublet occupancy may be used to combat the large background rate as we move into the regime of higher luminosities. This is demonstrated clearly in Figure 7; we can see from this graph that a straightforward cut on the sector doublet occupancy would reduce the background to more manageable levels while having little impact on the physics signal. It is certainly obvious from Figure 6 and Figure 7 that sectors with high levels of doublet occupancy have little real value in a trigger of this nature. While a cut of this type on it's own would not fully solve the inherent problems in a standalone track trigger at Run 2b it would be of certain value in separating the signal from background rates.

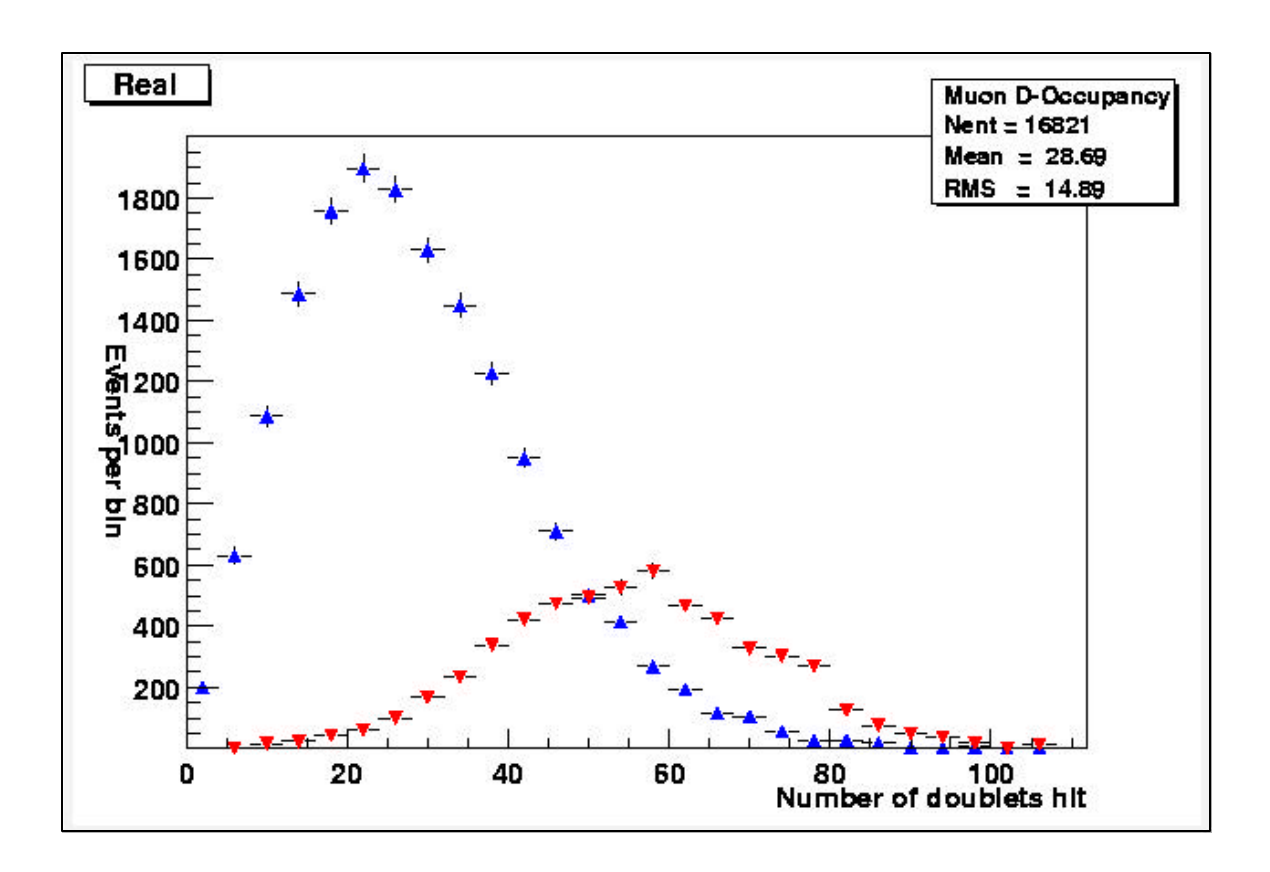


Figure 7. This graph shows the number of sectors reconstructed with a  $p_T > 5$  GeV/c track versus the number of doublets hit within that sector. The sectors where fake tracks have been reconstructed are shown in red; the sectors where the tracks have been properly reconstructed are shown in blue. This plot demonstrates that there is a significant difference between the sectors where fake tracks are reconstructed and those where the tracks are genuine muons.

### 3.4.1 Conclusions and implications for high luminosity

Based upon the simulations, it is believed that the significant numbers of background overlay events that will occur at Run 2b luminosities will cause substantial occupancy fractions in the CFT, and that the performance of the current tracking trigger will be compromised.

### 3.4.2 Comments on the CFT Lifetime

The Central Fiber Tracker (CFT) lifetime is basically determined by the robustness of the CFT's level 1 track trigger efficiency. Based on the CFT light yield as measured in the Lab 3 cosmic ray test and recently confirmed by data with beam, the L1 track trigger efficiency should remain above 95% for an integrated luminosity of 30 fb<sup>-1</sup>. We therefore see no need to replace any portion of the detector for the duration of Run 2, and it is not included in the project plan. Additional details on our studies of the CFT performance as a function of radiation dose are provided in the paragraphs below.

The primary radiation damage effect on the CFT is a reduction in the scintillating fiber attenuation length. There is essentially no change in the intrinsic light yield in the scintillator. The expected dose to the CFT as a function of radius was determined from analytical studies, GEANT simulations, and correlations to data taken at CDF during Run I on a prototype fiber system that was installed in the detector towards the end of Run I. From these data we determined that the total dose do the fibers on the CFT inner barrel (r=20cm) would be approximately 150 krad after 30 fb<sup>-1</sup>. In order to determine the radiation damage effect on the fiber, we performed both short-term high-rate exposures and long term (1 year), low-rate (14 rad/hr) exposures on sample fibers. Data from both these sets of measurements were in agreement and indicated that the attenuation length of our scintillating fiber would decrease from 5 m at 0 dose to 2.3 meters at 150 krad. The radiation damage effect is logarithmic in nature, so the effect at 1000 krad further reduces the attenuation length only to 1.6 m.

The light yield of the CFT has been studied with an extensive cosmic ray test that was performed with one of the production CFT cylinders mounted in the Lab 3 cosmic ray test stand. Selected ribbons on this cylinder were readout with waveguides of lengths corresponding to the actual lengths that would be used in the detector. The waveguide lengths varied from between 7.7 m and 11.4 m. The mean light yield (defined as the maximum yield in photoelectrons (pe) from a single fiber from within the fiber ribbon doublet) was approximately 12 pe for a waveguide length of 7.7 m and approximately 7 pe for 11.4 m. A Monte Carlo program was used to extrapolate these cosmic ray test results to beam conditions. The simulation used a single parameter fit to determine the intrinsic light yield from the fiber as determined by the cosmic ray test data. simulation then determine the photo-yield in beam conditions using this parameter and the beam conditions: tracks generate flat in rapidity, as-built fiber lengths for each cylinder and corresponding waveguide lengths for each trigger sector, measured fiber attenuation length for both the scintillating and waveguide fiber, and the fiber ribbon doublet geometry. The fiber attenuation length was degraded as a function of radiation dose following our actual radiation damage measurements on the fiber as given above. In order to calculate the actual trigger efficiency, the Monte Carlo also simulated the front-end electronics performance of the CFT analog-front-end board (AFE) and put in the nominal gains of the VLPCs used in the axial part of the detector. The fiber attenuation length was varied as a function of radiation dose as described above. The results are shown in Table 3 below. The trigger efficiency is given as a function of the fiber discriminator trigger threshold in fC (7 fC corresponds to approximately 1 pe) and radiation dose. The efficiency is for 8 out of 8 hits in the CFT axial layers. The CFT fiber discriminator trigger threshold is expected to be below 2 pe for all channels. The numbers in the left hand columns of the table correspond to the full rapidity coverage of the CFT (± 1.6), and those in the right hand columns correspond to the central  $\pm$  0.5 units of rapidity.

Table 3: Expected trigger efficiency as a function of fiber discriminator threshold for at various radiation exposures. Left hand (right hand) columns correspond to consideration of full (central) region of the tracker. See text for details.

Trig Thres (fC)	Eff	ficiency						
	0 f	b <sup>-1</sup>	2 f	b <sup>-1</sup>	30	fb <sup>-1</sup>	90	fb <sup>-1</sup>
7	0.997	0.996	0.997	0.995	0.996	0.994	0.994	0.987
10	0.995	0.989	0.992	0.986	0.987	0.979	0.982	0.965
13	0.993	0.985	0.992	0.984	0.986	0.973	0.976	0.955
16	0.987	0.970	0.984	0.968	0.969	0.939	0.953	0.902
21	0.975	0.941	0.969	0.932	0.937	0.874	0.902	0.802

### 3.5 Minimum Bias Models

As of this writing, the  $D\emptyset$  Monte Carlo is making a transition in its modeling of the minimum bias events. The old model uses the ISAJET Monte Carlo for QCD processes above  $p_T = 1.0$  GeV. The new model uses the **PYTHIA** Monte Carlo, with jets above p<sub>T</sub>=1.0 GeV, and includes some diffractive processes. As illustrated in Figure 8, the trigger rate results obtained using these two models are substantially different. Table 4 provides a comparison of results on the average occupancy of the fiber tracker (for layers on individual CFT cylinders) for minimum bias events from both models. The table also includes data that was gathered with the solenoid magnet on. The ISAJET model seems to result in higher occupancies than currently observed in minimum bias data, while the **PYTHIA** model generates substantially fewer hits than observed. However, the CFT readout electronics used to collect the data were pre-prototypes of the analog front end (AFE) boards. It is probable that noise on these boards could account for the some of the factor of two difference between the new PYTHIA model and data. It is not currently possible to determine whether the occupancies in the AFE data will eventually be a better match to results from the **ISAJET** or the **PYTHIA** model of the minimum bias events.

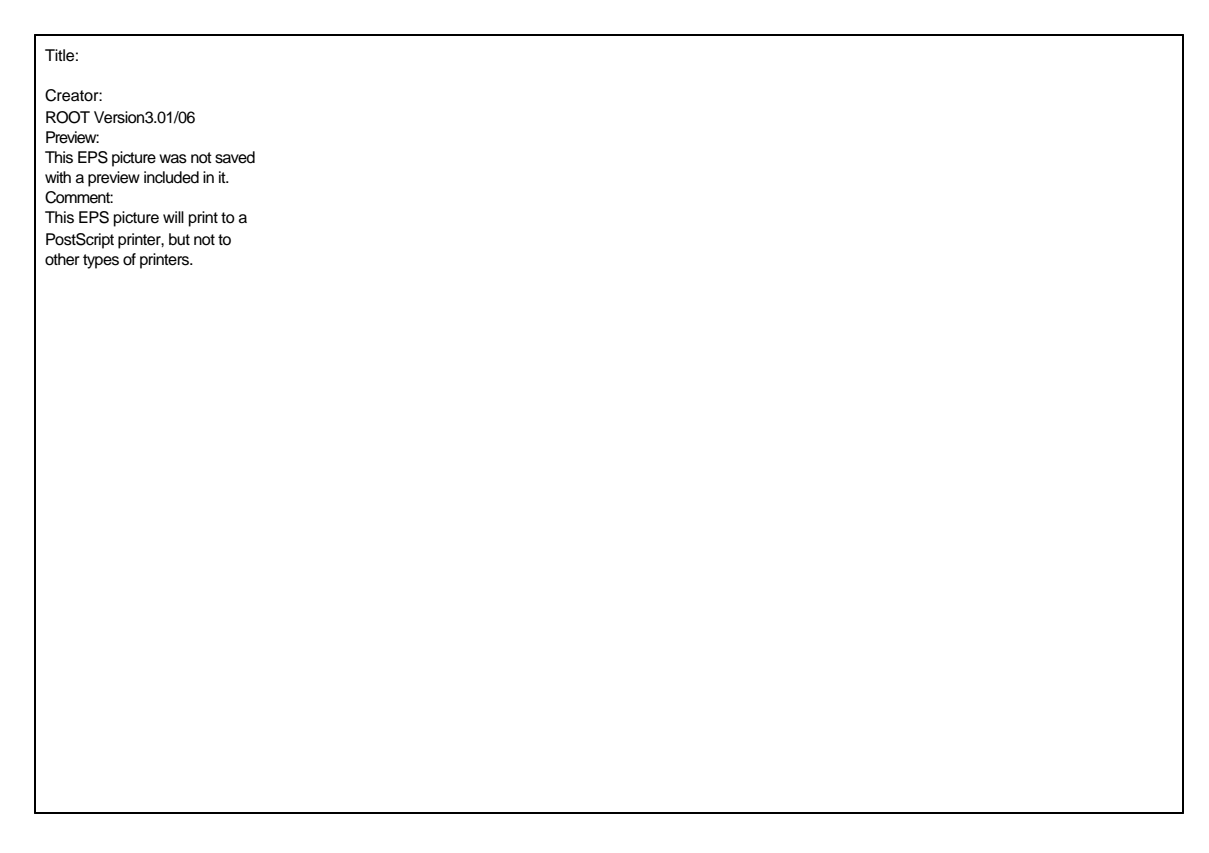


Figure 8. Comparison of the percent of Monte Carlo QCD events that satisfy the trigger as a function of the threshold of the track for events generated using **ISAJET** and **PYTHIA** models of overlaid minimum bias interactions.

Table 4. Comparison of the percentage occupancy of various layers of the CFT as calculated using two different minimum bias models of a single minimum bias interaction and as measured using low luminosity magnet on data.

CFT	ISAJET	PYTHIA	Data (%)	Old/Data	New/Data
Layer	(Old) Model (%)	(New) Model (%)			
Α	4.9	2.1	-	-	-
В	3.7	1.6	3.4	1.1	0.47
С	4.3	1.8	3.7	1.2	0.49
D	3.5	1.5	-	-	-
Е	2.9	1.2	2.3	1.3	0.52
F	2.5	1.0	-	-	-
G	2.1	0.87	1.6	1.3	0.54
Н	2.0	0.82	1.6	1.3	0.51

### 3.6 Overview of Options

As demonstrated above, the primary concern with the track trigger is the increase in rate for fake tracks as the tracker occupancy grows. Since the current track trigger requires hits in all 8 axial doublet layers, the only path to improving trigger rejection is to improve the trigger selectivity by incorporating additional information into the trigger algorithm. The short timescale until the beginning of Run 2b and resource limitations conspire to make it unlikely that the physical granularity of the fiber tracker can be improved, or that additional tracking layers can be added to the CFT.

One method of potentially increasing trigger selectivity in the axial tracking trigger without building additional detectors might be to treat the CPS axial layers as a ninth layer in the tracking trigger. This concept was explored as part of this study.

Another way to increase selectivity in the tracking trigger is to incorporate the information from the CFT stereo view fibers in the tracking trigger. A particular implementation of this concept is explored in this report.

A third method for increasing selectivity in the axial tracking would be to match the tracks to other surrounding detectors, and the studies of track calorimeter matching will be presented in the calorimeter trigger section of this report.

As detailed above, the current tracking trigger uses doublet hits, so it should be possible to improve the granularity of the tracking trigger (and consequently reduce the accidental background rates) by directly implementing the individual single fiber hits from the axial fibers in the trigger equations rather than using the doublets. Two particular implementations of the singlet equations are discussed in this report.

Another approach that may yield some relief under conditions of increasing luminosity might be to attempt to optimize the current set of axial trigger equations (e.g. drop the low probability track equations), or perhaps fit the track candidates to attempt to suppress accidentals. Occupancy requirements on trigger sectors may also be invoked to select against events that appear to be due to large numbers of interactions.

When all else fails, one is left with the undesirable options of either prescaling the tracking triggers or increasing the  $p_T$  thresholds to reduce trigger rates.

## 3.7 Axial CPS as Ninth Layer

### 3.7.1 Concept and Implications

The CPS detector has a similar structure to the CFT. As a consequence, the axial layer of the CPS might be employed as an effective ninth tracking layer for triggering purposes. If the AFE boards used to readout the CPS had dual threshold capability with one threshold set for efficient MIP recognition, this option could present minimal tradeoff. However, the current design of the AFE2

boards provides only one threshold per channel, and the minimum threshold that can be set is in the vicinity of 1-2 MIPs, too high to see minimum ionizing tracks efficiently. In any case, the  $\eta$  range of this nine-layer tracker would be  $\pm 1.3$ , while the eight-layer tracker extends out to  $\pm 1.6$ . This corresponds to an  $\approx 20\%$  reduction in acceptance.

### 3.7.2 <u>Implementation</u>

The implementation of the axial CPS layers as a ninth layer of the tracking trigger is a relatively straightforward task. The threshold of the CPS discriminators on the appropriate AFE boards would need to be lowered to a level such that minimum ionizing particles satisfy the discriminator threshold. A minimum ionizing particle deposits on average about 1.2 MeV in a CPS doublet, and as described below, ranges of thresholds below that level were studied.

## 3.7.3 Efficiency/Acceptance

The efficiency of this trigger was studied using samples of between 500 and 1000 single muon events which also contained a Poisson distribution of (ISAJET) minimum bias overlay interactions with a mean of five. Table 5 shows that this nine-layer trigger is better than 80% efficient for axial CPS hit thresholds below 0.25 MeV. The single muons in the Monte Carlo sample were generated in the range -1.2<  $\eta$  <1.2, to isolate the CPS acceptance issue from the performance of the nine layer tracking trigger.

Table 5. Efficiency of the tracking trigger for 15 GeV muons within the acceptance of the CPS (in percent) when the axial CPS information is used as the ninth layer in the tracking trigger.

Axial CPS Hit	9 Hit Track	≥8 HitTrack	9 Hit Track	≥8 HitTrack
Threshold	p <sub>T</sub> ≥10 GeV	p <sub>T</sub> ≥ 10 GeV	p⊤≥5 GeV	p <sub>T</sub> ≥5 GeV
1.0 MeV	52.4	93.2	53.6	94.0
0.5 MeV	75.5	95.3	76.0	95.3
0.25 MeV	82.1	94.9	83.7	94.9
0.15 MeV	79.7	95.4	81.3	96.3

### 3.7.4 Rates and Rejection Improvements

To study the potential improvements provided by this nine layer trigger, Monte Carlo samples of QCD events with a minimum  $p_T$  of 2 GeV were generated and overlaid with a Poisson distribution of (ISAJET) minimum bias interactions with a mean of five minimum bias interactions. The improvement in rejecting fake tracks is fairly minimal. The percent of time certain CTT terms were satisfied for these events are shown in Table 6. Using a threshold, which provides almost no efficiency for real tracks, the rejection of fake tracks is about

35%. If the threshold is reduced so that the efficiency for real tracks is larger than 80%, then the rejection of fake tracks is about 17%.

The fact that the fake rates do not increase as the CPS hit threshold is reduced from 025 MeV to 0.15 MeV indicates that perhaps there is a hidden minimum threshold in the current Monte Carlo, and may account for the observation that the efficiency of the nine hit tracks as reported in Table 5 fail to reach the same level as the 8 hit tracks.

Table 6. Percentage of events from the 2 GeV QCD sample that satisfy various trigger requirements as a function of the threshold for the hit in the axial CPS which is serving as the ninth layer of the tracking trigger in this simulation.

Axial CPS Hit	9 Hit Track	≥8 HitTrack	9 Hit Track	≥8 Hit Track
Threshold	p <sub>T</sub> ≥10 GeV	p⊤≥10 GeV	p <sub>T</sub> ≥5 GeV	p <sub>T</sub> ≥5 GeV
3.0 MeV	11.6	15.6	18.0	24.8
1.0 MeV	13.6	17.6	19.0	25.0
0.5 MeV	15.2	18.0	22.8	28.0
0.25 MeV	15.0	17.6	21.0	25.0
0.15 MeV	15.0	17.6	21.0	25.0

#### 3.7.5 Cost & Schedule

As long as one is willing to accept the loss of the CPS electron tagging in the trigger and reduce the acceptance of the tracking trigger, there are relatively minor costs or schedule impacts to consider. Note however that the CPS electron tagging capability could be resurrected if the AFE2 design allowed for dual thresholds, but such a decision would have serious implications

#### 3.7.6 Conclusions

The 15 to 20% background rate rejection achieved by using the axial CPS as a ninth layer in the tracking trigger is of minimal use; however, given the ease of implementation this option may be a useful stop-gap measure if other plans fall behind schedule, or do not quite achieve the necessary rejection.

#### 3.8 Stereo Track Processor

## 3.8.1 <u>Concept</u>

A second strategy to reduce the L1 CTT fake rate would implement a second fast digital processor that can incorporate the hits in the stereo layers of the CFT in the L1 CTT. This upgrade has the additional advantage that three-dimensional tracks would be available at Level 1 for matching to calorimeter hits and even allowing invariant mass calculations at L1.

The overall strategy for adding stereo hit information to the axial tracks is predicated on the availability of the axial track parameters ( $\phi$  and  $p_T$ ) in order to make the problem tractable. Then, a pattern of 7 or 8 stereo hits can be matched to the pre-determined trajectory of the axial track. The algorithm is shown schematically in Figure 9.

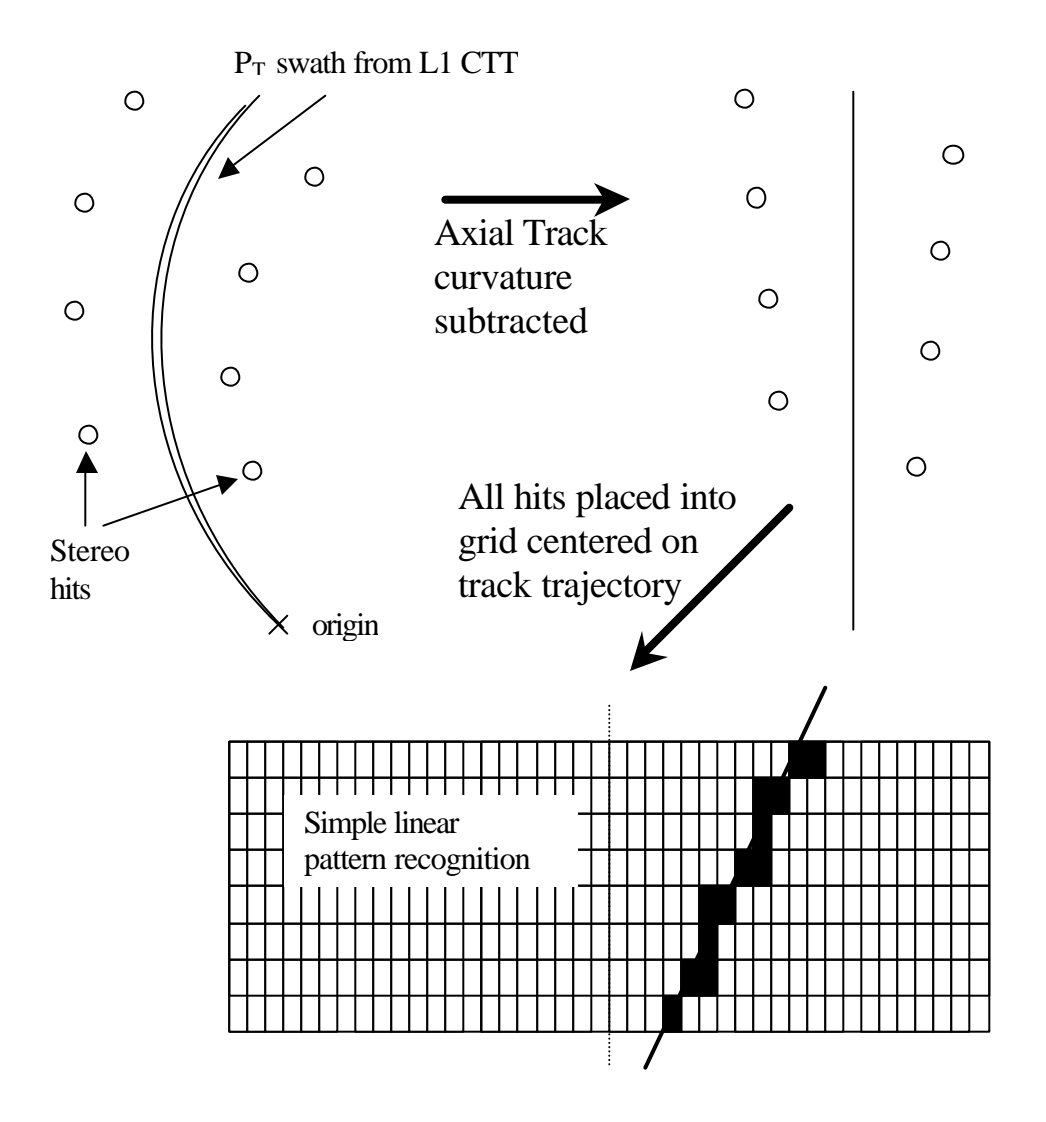


Figure 9. Schematic representation of the algorithm used to attach stereo hits to an axial seed track. See text for a detailed description.

The stereo tracking algorithm makes use of the linear relation between the difference in stereo  $(r\mathbf{f}_s)$  and axial  $(r\mathbf{f}_a)$  fiber indices and the vertex position  $(z_0)$  and  $\cot(\mathbf{q})$ :  $r\mathbf{f}_s - r\mathbf{f}_a = (z_0 + r\cot(\mathbf{q}))/\tan(\mathbf{l})$  where r is the radius of the layer and  $\tan(\mathbf{l})$  is the stereo angle. First, axial tracks are received from the current L1

CTT. The information contained in a "track" consists of a fiber index on the outermost CFT cylinder and, for high-momentum tracks, a range in p<sub>T</sub> allowed by the pattern of hits. The fiber index provides precise  $\phi$  focation. This, combined with the constraint that the track must pass through the origin, allows the definition of a crescent-shaped region in the rop plane, which should contain the true trajectory of the axial track. In order to reduce the complexity of the problem, the centroid of the trajectory is defined as the locus of the track in each axial layer. Then, all CFT stereo fibers that cross the central axial fiber are searched for hits. The difference in fiber indices between the stereo and axial fibers is computed for each stereo hit. In this space, the U and V hits form approximately straight lines on either side of the straightened axial track, as shown in Figure 9. The U-fiber hits, which have the opposite sign for tan(I), are flipped about the central trajectory, and the offset of all single-fiber hits from the central trajectory is entered into a grid. This is done for all accessible stereo The track-finding algorithm reduces to a simple search for 7 or 8 hits connected in a straight line. To reduce the combinatoric background, a  $\chi^2$  fit is done separately to U and V hits to determine whether or not they lie in straight lines around the central trajectory. (Small errors in the centroid position resulting from imprecise knowledge of the track pt can result in different slopes for the different sets of stereo hits.) In the results presented below, no attempt has been made to merge neighboring hits into clusters; only the single fiber hits are used for this track finding.

In the results that follow, the added stereo hits have only been used to confirm the validity of the input L1 CTT axial tracks. No attempt has been made to examine the stereo track parameters and place cuts on the z position where the track crosses the beam line or on the track  $\eta$ . In any case, the Monte Carlo studies show that tracks with extreme values of z or  $\eta$  are a relatively small fraction of the total number of fake tracks. The stereo tracking algorithm could potentially make available the z coordinate and track  $\eta$ .

### 3.8.2 Simulation

A simulation of the stereo tracking algorithm was inserted into the existing trigger simulation in order to make as realistic an estimate as possible of the actual operating conditions. Axial tracks from the L1 CTT simulation code were fed to a Stereo Track Processor (STP) that executed the algorithm described above. High efficiency (99%) was achieved for matching stereo hits to axial tracks found in high-  $p_T$  single muon events.

In order to estimate the additional rejection against fake tracks provided by the stereo hit information, the rate of tracks found by the STP is compared with that from the current L1 CTT. This is shown in Table 7 for single high-  $p_T$  muon events with *fixed* numbers of minimum bias interactions overlaid. The rate calculated corresponds to the number of fake tracks with  $p_T > 5$  GeV generated per event. The minimum bias events in these samples were generated by **ISAJET** and potentially overestimate the occupancy of the CFT by a small amount. For

this table, 8 out of 8 possible stereo hits are required to confirm an axial track. This information is shown graphically in Figure 10.

Table 7. The effect of minimum bias events on the track trigger rate. The fake track rate is the number of fake tracks with  $p_T > 5$  GeV generated per event. The column labeled "L1 CTT" is the rate of fake tracks from the default Level 1 track trigger. The column labeled "after Stereo Hits" gives the rate of fake tracks with the combined stereo and axial track triggers. The final column gives the fraction of fake tracks produced by the axial trigger that are rejected by the addition of stereo hits.

# min bias events	L1 CTT Fake track rate	Fake track rate after Stereo Hits	Extra rejection
1	0.136	0.001	0.99
2	0.235	0	1.00
3	0.347	0.057	0.84
4	0.578	0.199	0.66
5	0.972	0.377	0.61

#### **Reduction of L1CTT Rate with UV Information**

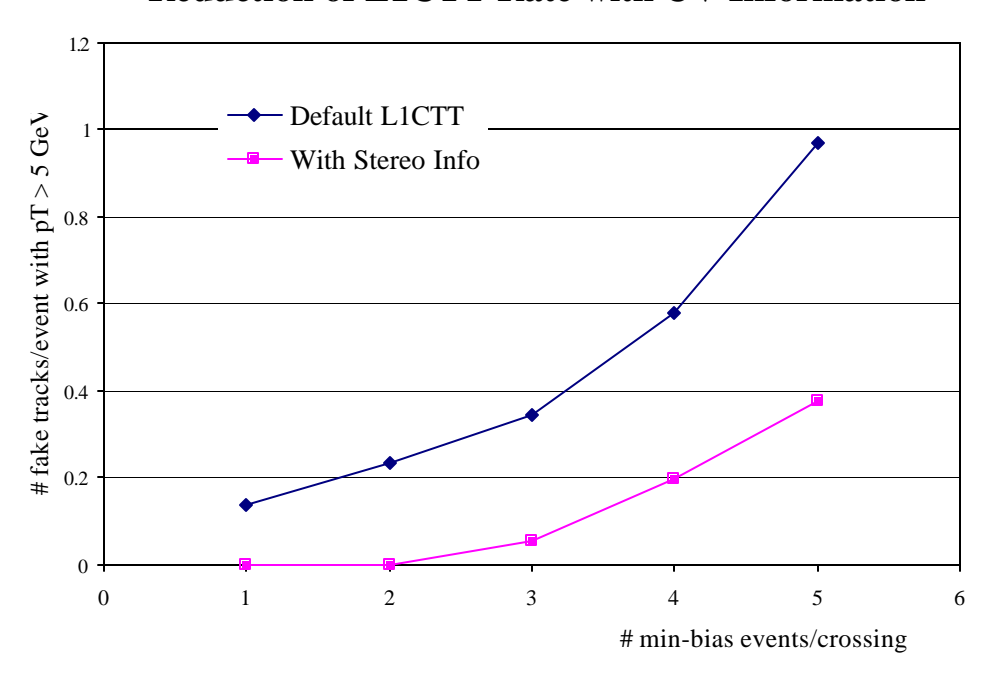


Figure 10. The additional rejection power provided by adding stereo hits to the found axial tracks. The rate of fake tracks with  $p_T > 5$  GeV generated per event is plotted for the default L1 CTT and after the addition of stereo hits.

Studies requiring only 7 out of 8 stereo hits to form a valid track show that the extra rejection provided by the stereo information drops from 61% to 26% for a sample of high-  $p_T$  muon events with exactly 5 minimum bias events overlaid.

#### 3.8.3 <u>Implementation</u>

Due to the stereo angle, each axial fiber can cross up to 300 fibers in the outer CFT layers, making the number of possible track-hit combinations very large. In addition, since such a large fraction of the CFT stereo hits will need to be compared to an arbitrary axial track, much of the total stereo hit information will need to be available on any Stereo track-finding board. These considerations lead one to an architecture where all of the stereo data is sent to a small number of processing boards where the actual track finding takes place. The data-transfer rate requirements are severe, but presumably tractable, especially since the stereo information can be transferred while waiting for the axial track parameters to arrive from the current axial track-finding boards. Large buffers and substantial on-board data buses would be required in order to hold and process the large quantity of data. A possible schematic is shown in Figure 11. Essentially, a parallel data path very similar to what will exist for the L1 CTT would need to be built, but without the added complexity of the "mixer box" that sorts the discriminator signals into sectors. Moving the SIFT signals from the

AFE boards for the stereo layers is relatively simple; sorting and processing them once they reach the track-finding boards will require a substantial engineering effort.

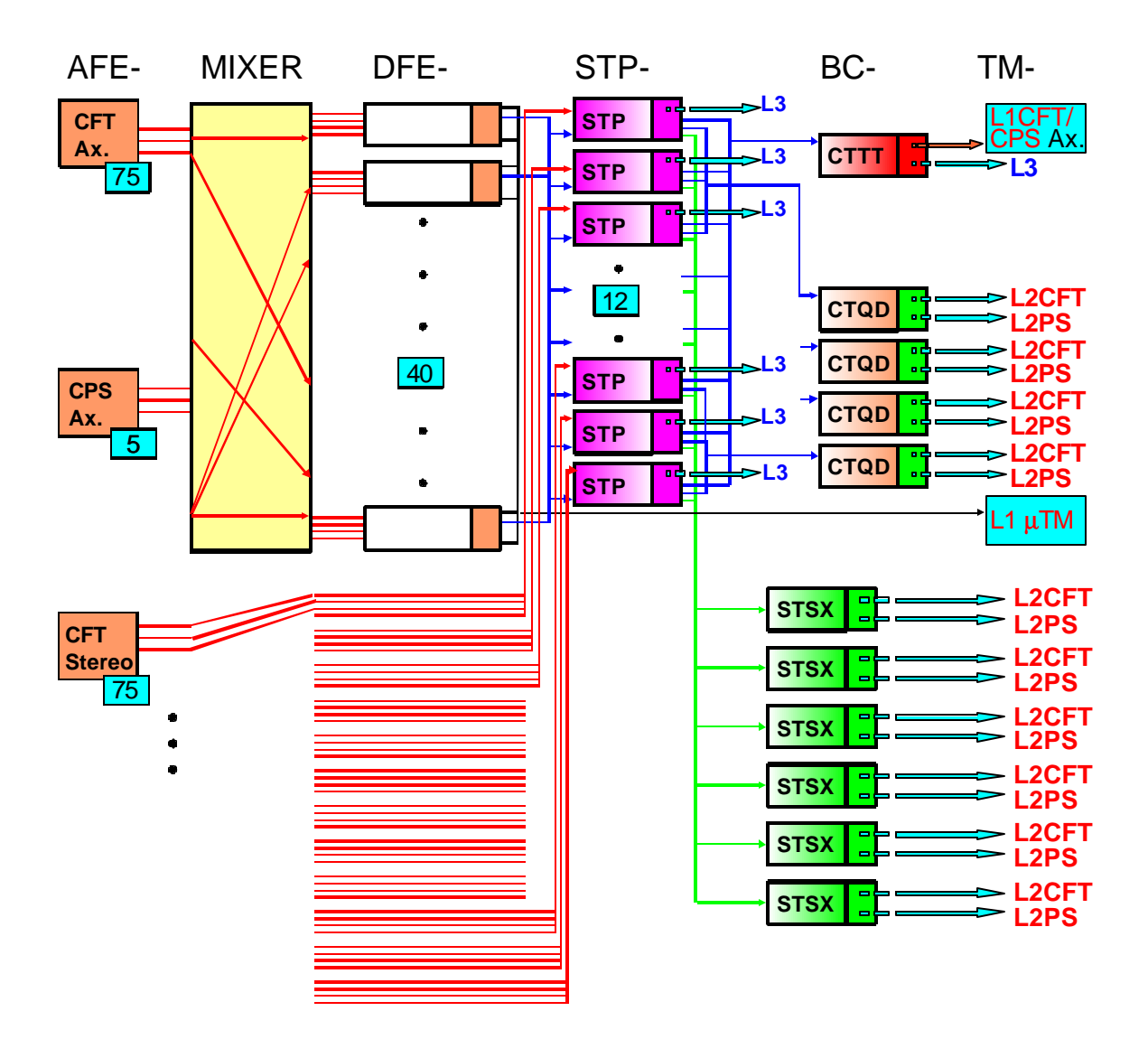


Figure 11. Schematic diagram of the implementation of stereo tracking in the trigger.

This upgrade would also require small modifications to the transition boards at the back end of the current L1 CTT system so that the axial track candidates

could be shipped to the new stereo track processor. The inputs to the L2STT would also be modified so that L2 could take full advantage of the refined track information.

#### 3.8.4 Conclusions

The addition of stereo information provides good rejection of fake tracks at high transverse momentum, but the large complexity and correspondingly large expense of the system probably does not justify its construction given the modest expected reduction in trigger rate.

### 3.9 Singlet Equations

### 3.9.1 <u>Concept</u>

The idea behind singlet equations is illustrated in Figure 3, which shows a fragment of a CFT doublet layer. The thick black lines mark the area corresponding to a doublet hit. As one can see from Figure 3, the doublet is a little larger than fiber diameter, which suggests that roads based on single fibers will be a little narrower and therefore have reduced fake probability. Also, if one requires a particular single fiber hit pattern in the doublet hit, the size of the hit becomes even smaller (thin dotted lines in Figure 3) promising even more background rejection.

It is clear, however, that increased granularity of the trigger leads also to an increase in the number of equations. The concrete estimate of the FPGA resources needed is yet to be done. Keeping in mind this uncertainty we considered two trigger configurations: all-singlet (i.e. 16 layer) and a case when four out of eight CFT layers are treated as pairs of singlet layers, giving effectively a 12 layer trigger. For this second case, the hits from axial fibers mounted on the inner four cylinders (cylinders A, B, C, and D) were treated as singlets, while the hits from axial fibers on the outer four cylinders (cylinders E through H) were treated as doublets in the same manner as the Run 2a CTT.

Equations for both configurations were generated. The probability that a track will have  $\geq 8$ ,  $\geq 10$ ,  $\geq 11$ ,  $\geq 12$  and 13 hits out of 16 possible for the first trigger scheme and  $\geq 8$ ,  $\geq 9$ ,  $\geq 10$ ,  $\geq 11$  and 12 hits out of the maximum of 12 in the second trigger scheme are shown in Figure 12 (it is assumed that fibers are 100% efficient).

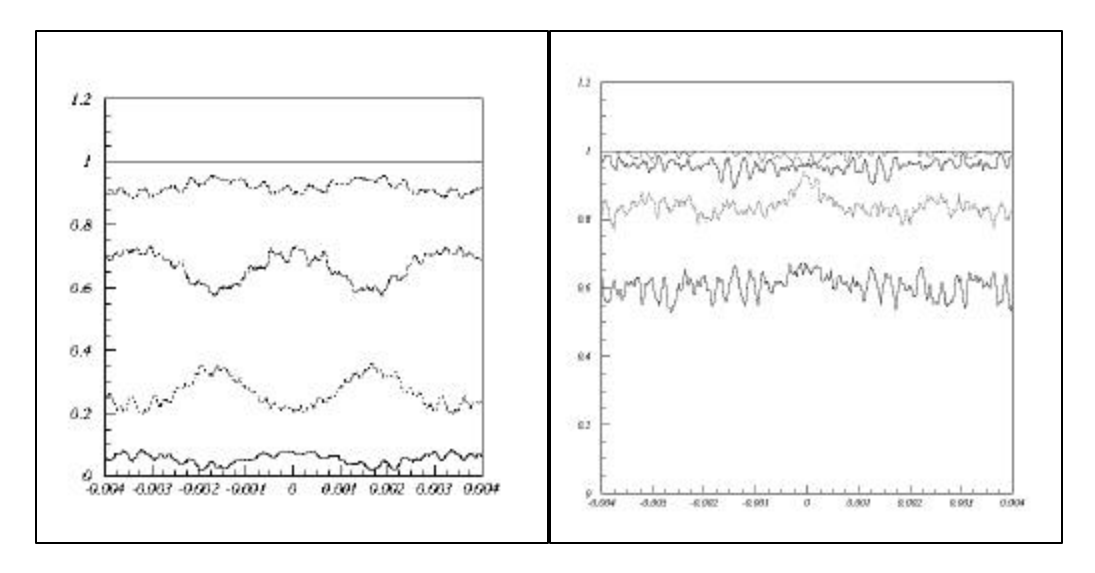


Figure 12. Left panel: geometrical acceptance for a charged particle to satisfy a  $\geq 8$  (solid line),  $\geq 9$  (dashed curve),  $\geq 10$  (dotted curve),  $\geq 11$ (dot-dashed curve) and 12 (solid curve) hit requirement in the 12-trigger layer configuration, versus the particle track sagita,  $s = 0.02 e^/ p_T$ . Right panel: similar plot for 16-layer trigger and  $\geq 8$ ,  $\geq 10$ ,  $\geq 11$ ,  $\geq 12$  and 13 hits per track.

The maximum rejection achievable, compared to the standard doublet equations, can be estimated without complicated simulation by comparing sets of singlet and doublet equations as follows. In an equation a doublet hit can originate from four different combinations of single fiber hits (see the four different regions indicated by the dashed lines between the thick black lines in Figure 3). The combination of pitch and active fiber diameter is such that all four combinations are about equally probable. Therefore each doublet equation can be represented as a set of  $4^4 = 256$  equations in the 12-layer trigger configuration. Some of these expanded equations will be identical to some of the true singlet equations. Some will just have eight or more hits in common with them. Since the background rate is proportional to the number of equations, the relative rate is given by the fraction of expanded equations that can be matched to the true singlet equations. We determined this fraction considering all true singlet roads, only those with nine or more hits and then those with ten or more hits to be 0.44, 0.18 and 0.03 respectively. From Figure 12 these three cases correspond to trigger efficiencies of 100%, ~93%, and ~65%.

These numbers, though encouraging, may be too optimistic in two ways. First, the impact of imperfect fiber efficiency is a little worse for singlet than for doublet equations. Second, singlet roads require that certain fibers not be hit, which can introduce inefficiency in a high occupancy environment<sup>3</sup>.

Both concerns can be addressed and their impact reduced. One can soften requirements on the match of the road with hit fibers. One can increase the

-

Note, that current triggering scheme also requires that some fibers will not be hit. Thi requirement is implemented in the doublet formation phase.

number of the roads to pick up the tracks that would otherwise be lost due to fiber inefficiency or extra hits. This presents an optimization problem that can be rigorously solved. The optimization parameters are the amount of FPGA resources (*i.e.* number of equations, matching algorithm and number of trigger layers), signal efficiency, and background rate.

Such an optimization has not yet been performed. For this document, we considered a conservative approach. The singlet road fires if 1) the doublet road which this singlet road corresponds to fires and 2) if more than eight elements of the singlet road fire. The second requirement was varied to optimize signal to background ratio. The first requirement guarantees that each of the doublet layers has a hit and is also a disguised veto requirement on certain neighboring fiber hits.

#### 3.9.2 Simulation

The existing trigger simulation was adapted to make a realistic estimate of the trigger performance. Single muons were generated, overlaid on events containing exactly five (ISAJET) minimum bias interactions and put through the detailed  $D\varnothing$  simulation. They were then put through the modified trigger simulator. Single fiber efficiency is still assumed to be perfect. The fraction of events that had a trigger track matching the muon measures the trigger efficiency, while the number of high  $p_T$  tracks that do not match the generated muons measures the accidental background rate.

## 3.9.3 Rates and Rejection Improvements and Efficiency

The results of the procedure described above for a 1300 event sample of 12 GeV muons are summarized in Table 8 for 12-layer and Table 9 for 16-layer trigger. For the case of 12-layer equations with ≥9 out of 12 hits, the background is reduced by a factor of about two without significant loss of efficiency. For 16-layer case the improvement is larger and is about factor of five for high pt tracks.

Note also, that the fraction of mis-reconstructed muons, *i.e.* muons which give trigger in the wrong  $p_T$  bin is also reduced when going to singlet equations, especially for 16-layer case. It is very important for STT, which depends on the quality of the seed tracks from L1CTT.

Table 8. Numbers of events (out of 1300) that satisfy various track trigger requirements for an implementation of the tracking trigger that uses singlets for the axial fibers on the inner four cylinders and doublets for the axial fibers on the outer four cylinders.  $TTK(n,p_T)$  is a trigger requiring n tracks with transverse momentum greater than  $p_T$ .

	Doublet Equations	Singlet Equations	Singlet Equations (≥9 of 12)	Singlet Equations (≥10 of 12)
# matched p <sub>T</sub> >10	1199	1200	1191	1019

# matched 5< p <sub>T</sub> <10	37	14	16	26
# fakes p <sub>T</sub> >10	91	61	50	31
# fakes 5< p <sub>T</sub> <10	206	136	124	77
Fake TTK(1,10)	79	55	45	31
Fake TTK(2,10)	10	5	4	0
Fake TTK(1,5)	159	115	103	69
Fake TTK(2,5)	34	18	18	7

Table 9. Numbers of events (out of 1300) that satisfy various track trigger requirements for a trigger based upon singlet equations for all sixteen possible axial layers.  $TTK(n,p_T)$  is a trigger requiring n tracks with transverse momentum greater than  $p_T$ .

	Doublet Equations	Singlet Equations (≥10 of 16)	Singlet Equations (≥11 of 16)	Singlet Equations (≥12 of 16)
# matched p <sub>T</sub> >10	1199	1210	1172	1046
# matched 5< p <sub>T</sub> <10	37	5	5	4
# fakes p <sub>T</sub> >10	91	26	16	10
# fakes 5< p <sub>T</sub> <10	206	70	33	21
Fake TTK(1,10)	79	26	16	10
Fake TTK(2,10)	10	0	0	0
Fake TTK(1,5)	159	63	47	30
Fake TTK(2,5)	34	7	2	1

## 3.9.4 Implementation, Cost & Schedule

The implementation, cost and schedule depends largely on the algorithm chosen and how much FPGA chip resources that algorithm requires. For an algorithm requiring a modest increase in resources, the present daughter boards

(DB) could be reworked and reused. This would be accomplished be removing the present FPGA chips that are in Ball Grid Array (BGA) packages and mounting new ones. If the algorithm were more complicated and larger, more powerful chips with new footprints were required, then the daughter boards would also have to be replaced. Preliminary cost estimates for these two options, which are based on our experience fabricating and instrumenting the current boards, are shown in Table 10 and Table 11 below.

Table 10: Preliminary cost estimate for upgrade to the track trigger associated with the handling of fiber singlets that does not include replacement of the daughter boards. A contingency of 50% is applied.

Item/process	Unit Cost (\$)	# Required	Total Cost (\$k)	Total Cost + 50% Contingency (\$k)
Remove FPGA	20	350	7	10.5
Remount FPGA	20	350	7	10.5
Purchase new FPGA	500	350	175	263
TOTAL			\$189k	\$284k

Table 11: Preliminary cost estimate for upgrade to the track trigger associated with the handling of fiber singlets that includes replacement of the daughter boards. A contingency of 50% is applied.

Item/process	Unit Cost (\$)	# Required	Total Cost (\$k)	Total Cost + 50% Contingency (\$k)
Fabricate/stuff new Daughter Boards	500	88	44	66
Purchase new FPGA	900	350	315	473
TOTAL			\$360k	\$540k

It should be pointed out that this upgrade affects only the 88 DFEA boards. All of the AFE, MB and other DFE type boards are not changed or modified in any way. The engineering time associated with this FPGA upgrade is consequently of limited scope and the production is limited to a single board series; much of the effort and resources will necessarily be focused on the algorithm logic and FPGA programming. In light of the relative simplicity of the design and fabrication, we see no obstacles to having this system in place for the Run 2b startup in early 2005. A resource-loaded cost and schedule is in the process of being developed.

#### 3.9.5 Conclusions

Increasing the capacity of the FPGA available for the implementation of the track trigger is among the most straightforward of the options to implement in the hardware. Upgrading the current track trigger in this fashion is likely to be both cost effective and to be possible to execute in the available timescale. Furthermore, this upgrade is among the most flexible, allowing for the implementation of additional improvements late in the game as insights gleaned from the operation of the current version of the trigger and additional detailed studies of possible singlet configurations become available. This upgrade looks most promising and detailed studies of this option should be pursued.

## 3.10 L1 Tracking Trigger Summary and Conclusions

Based upon current simulation results, it seems likely that the L1 CTT may need to be upgraded in order to maintain the desired triggering capabilities as a result of the anticipated Run 2b luminosity increases. Because of the tight timescales and limited resources needed to address this particular challenge, significant alterations to the tracking detector installed in the solenoid bore are not considered feasible.

Other possibilities to effectively enhance the coincidence level employed in the L1 CTT have been explored. Using the axial CPS detector as a ninth layer in the trigger may provide some small background suppression at the expense of the L1 CTT electron capability as well as a reduction in the  $\eta$  acceptance of the L1 CTT. The CPS threshold needed to see single MIP particles will be difficult to achieve. This does not appear to be an attractive option.

The stereo track processor could potentially be incorporated into the L1 CTT to enhance background rejection, and simulation results indicate that a substantial gain in background rejection could be achieved by this technique. Unfortunately, the implementation of the stereo trigger would likely require significant resources in the development phase as well as increases in the infrastructure including the cable plant on the platform. Since other less expensive techniques to achieve similar rejection rates has been identified, the stereo track processor is not considered a viable option.

Improving the resolution of the L1 CTT by treating at least some fraction of the CFT axial layers as singlets rather than doublet layers in the L1 trigger should improve the background rejection of an upgraded L1 CTT by a significant amount. Simulation studies that treat the fibers on the inner four CFT cylinders as singlet layers in the trigger indicate that about a factor of two improvement in the background rejection can be achieved (with only a small impact on the trigger efficiency). Studies that treat the hits from fibers on all axial layers as singlets in the trigger yield improvements in the fake rejection rate by more than a factor of five.

The performance of the Run 2b detector will almost certainly be enhanced if the FPGA are upgraded to allow for a significant increment in the number of equations that can be handled. This particular upgrade is very likely to facilitate a substantial improvement in the background rejection rate at a moderate cost. Even if singlet equations are not implemented in the FPGA, the FPGA upgrade provides a significant enhancement in flexibility of the track finding algorithms that may be implemented, and consequently should be given serious consideration.

# 4 Level 1 Calorimeter Trigger

#### 4.1 Goals

The primary focus of Run 2b will be the search for the mechanism of electroweak symmetry breaking, including the search for the Higgs boson, supersymmetry, or other manifestations of new physics at a large mass scale. This program demands the selection of events with particularly large transverse momentum objects. The increase in luminosity (and thus increasing multiple interactions), and the decreased bunch spacing (132ns) for Run 2b will impose heavy loads on the L1 calorimeter trigger. The L1 calorimeter trigger upgrade should provide performance improvements over the Run 2a trigger system to allow increased rejection of backgrounds from QCD jet production, and new tools for recognition of interesting signatures. We envision a variety of improvements, each of which will contribute to a substantial improvement in our ability to control rates at the Level 1 (L1) trigger. In the following sections we describe how the L1 calorimeter trigger upgrade will provide

- An improved capability to correctly assign the calorimeter energy deposits to the correct bunch crossing via digital filtering
- A significantly sharper turn-on for jet triggers, thus reducing the rates
- Improved trigger turn-on for electromagnetic objects
- The ability to make shape and isolation cuts on electromagnetic triggers, and thus reducing rates
- The ability to match tracks to energy deposition in calorimeter trigger towers, leading to reduced rates
- The ability to include the energy in the intercryostat region (ICR) when calculating jet energies and the missing ET
- The ability to add topological triggers which will aid in triggering on specific Higgs final states.

The complete implementation of all these improvements will provide us with the ability to trigger effectively with the calorimeter in the challenging environment of Run 2b.

### 4.2 Description of Run 2a Calorimeter Electronics

#### 4.2.1 Overview

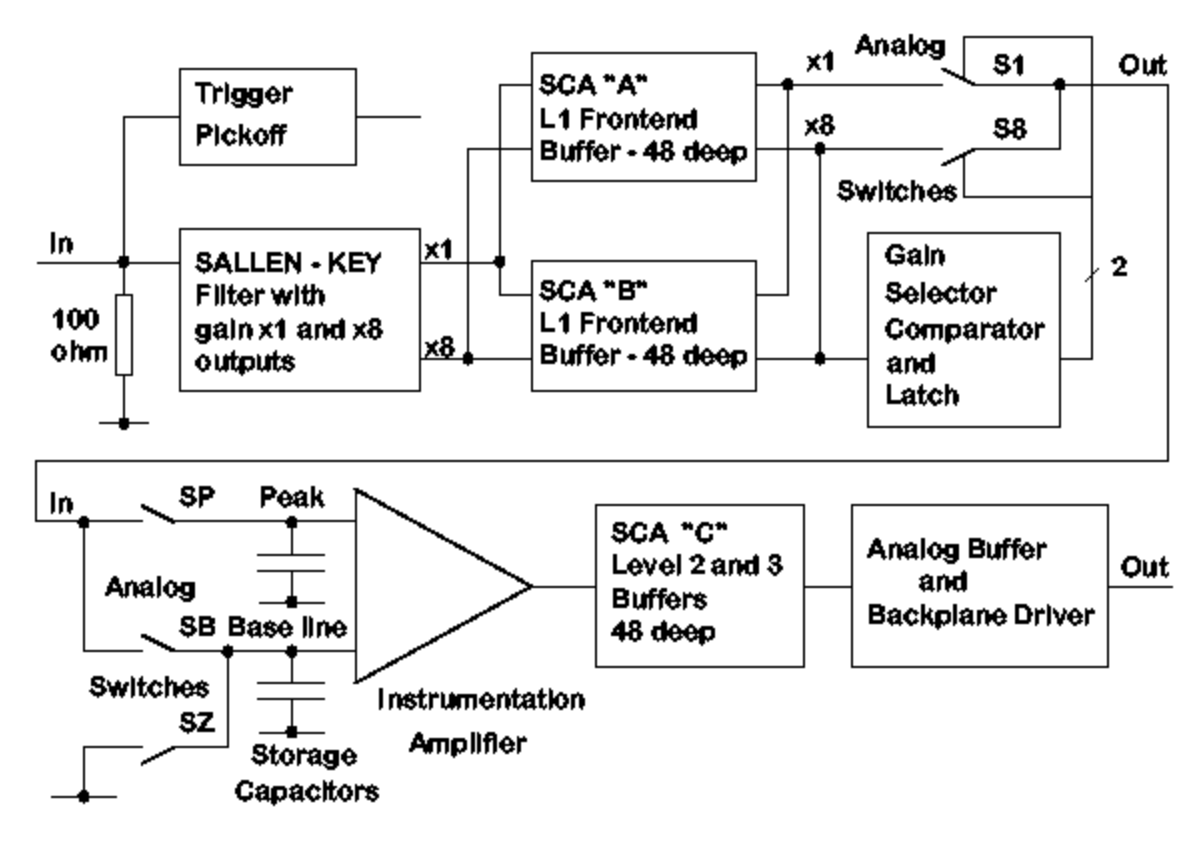


Figure 13. Functional diagram of the BLS system showing the precision readout path and the location of the calorimeter trigger pickoff signal.

The charge from the calorimeter is integrated in the charge sensitive preamplifiers located on the calorimeter. The preamplifier input impedence is matched to the 30  $\Omega$  coaxial cable from the detector (which have been equalized in length), and the preamplifiers have been compensated to match the varying detector capacitances, so as to provide signals that have approximately the same rise time (trace #1 in Figure 14). The fall time for the preamp signals is 15 µs. The signals are then transmitted (single ended) on terminated twisted-pair cable to the baseline subtractor cards (BLS) that shape the signal to an approximately unipolar pulse (see Figure 13 for a simple overview). The signal on the trigger path is further differentiated by the trigger pickoff to shorten the pulse width, leading to a risetime of approximately 120 ns (trace #2 in Figure 14). The signals from the different depths in the electromagnetic and hadronic sections are added with appropriate weights to form the analog trigger tower sums. These analog sums are output to the L1 calorimeter trigger after passing through the trigger sum drivers. The signals are then transported differentially (on pairs of  $80\Omega$  coaxial cable) 80m to the L1 calorimeter trigger (the negative side is shown in trace #4 in Figure 14). A set of oscilloscope pictures of some of these points is shown in Figure 14, see the figure caption for details. The key elements

of the calorimeter trigger path are described in more detail in the following sections.

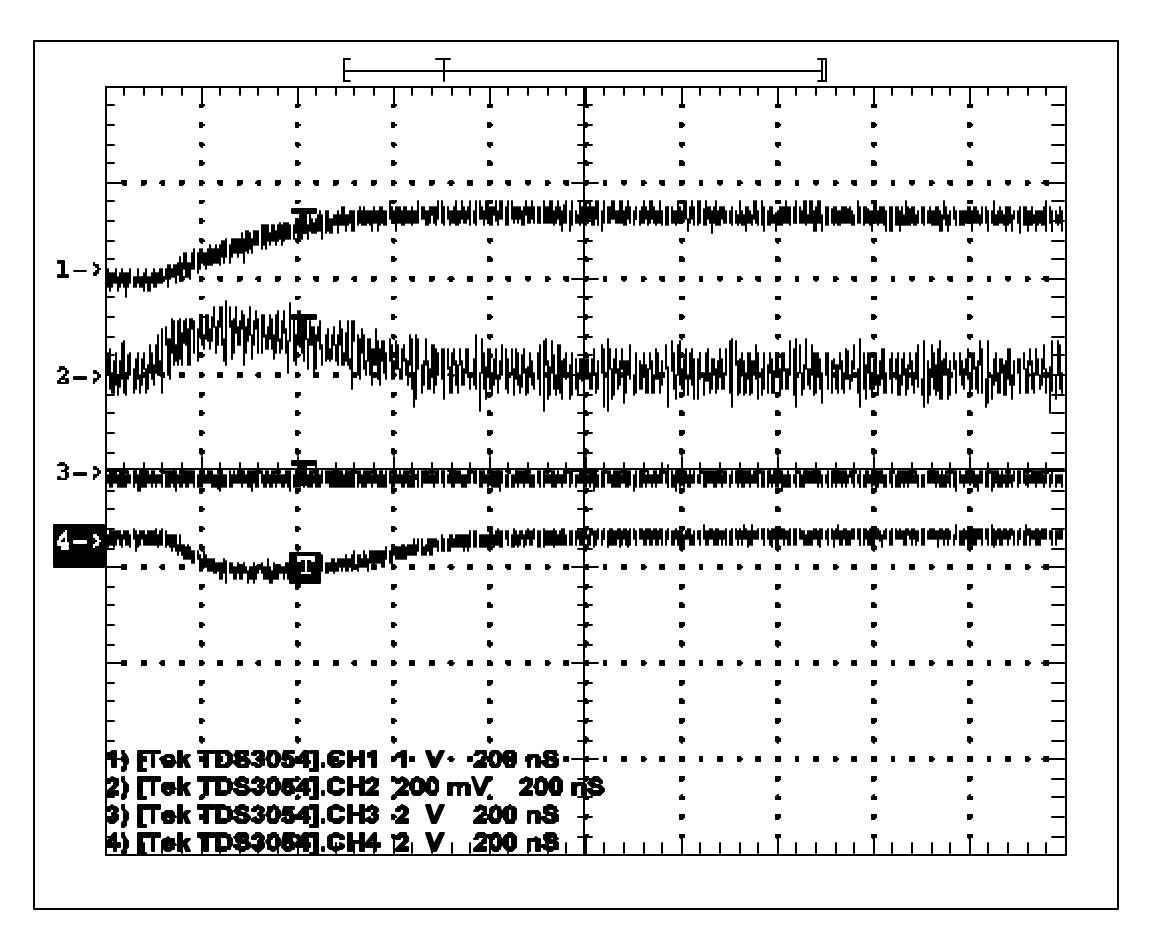


Figure 14. Scope traces for actual detector signals for an EM section. The horizontal scale is 200ns/div. The top trace (#1, 1V/div) is of a preamp output signal as seen at the input to the BLS. The second trace (#2, 200mV/div) is of the trigger pickoff output on the BLS card (the large noise is due to scope noise pickup, but is not real). The fourth trace (#4, 2V/div) is the negative side of the differential trigger sum driver signal at the BLS that is sent to the L1 calorimeter trigger.

## 4.2.2 Trigger pickoff

The trigger pickoff captures the preamplifier signal before any shaping. A schematic of the shaping and trigger pickoff hybrid is shown in Figure 15 (the trigger pickoff section is in the upper left of the drawing). The preamplifier signal is differentiated and passed through an emitter follower to attempt to restore the original charge shape (a triangular pulse with a fast rise and a linear fall over 400 ns). This circuitry is located on a small hybrid that plugs into the BLS motherboard. There are 48 such hybrids on a motherboard, and a total of 55,296 for the complete detector.

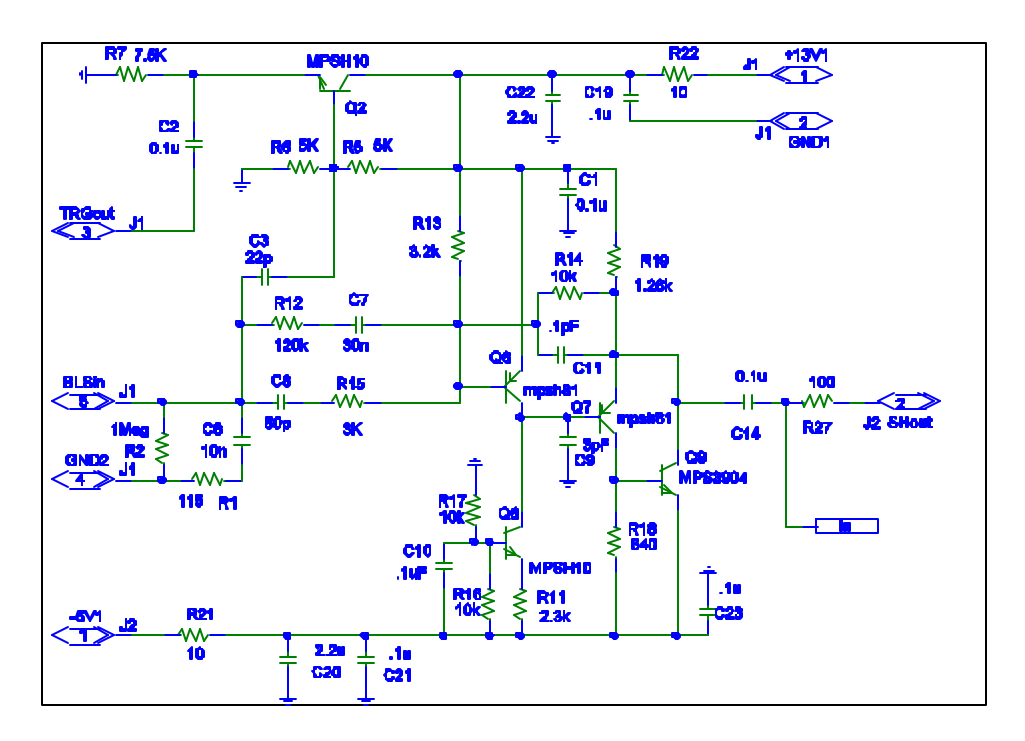


Figure 15. Schematic of the trigger shaper and trigger pickoff (upper left of picture). Pin 5 is the input, pin 3 is the trigger pickoff output, and pin 2 is the shaped precision signal output.

## 4.2.3 Trigger summers

The trigger pickoff signals for EM and HAD sections in individual towers (note these are not the larger trigger towers) are routed on the BLS board to another hybrid plug-in that forms the analog sums with the correct weighting factors for the different radial depth signals that form a single tower. The weighting is performed using appropriate input resistors to the summing junction of the discrete amplifier. A schematic for this small hybrid circuit is shown in Figure 16.

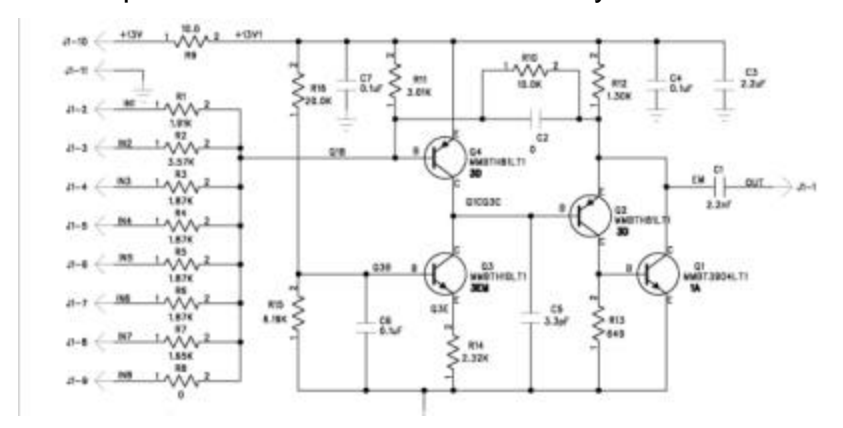


Figure 16. Schematic of the trigger summer hybrid. Up to 8 inputs from the various layers in a single tower can be summed with varying gains determined by the resistors to the summing junction (shown at left).

A single 48 channel BLS board has 8 trigger summer hybrids (4 EM towers and 4 HAD towers). There are a total of 9,216 hybrid trigger summers made up of 75 species. Since they are relatively easy to replace, changes to the weighting schemes can be considered. Recall, however, that access to the BLS cards themselves requires access to the detector as they are located in the area directly beneath the detector, which is inaccessible while beam is circulating.

### 4.2.4 <u>Trigger sum driver</u>

The outputs of the 4 EM trigger summers on a single BLS board are summed (except at high  $\eta$ ) once more by the trigger sum driver circuit (see the schematic in Figure 17) where a final overall gain can be introduced. This circuit is also a hybrid plug-in to the BLS board and is thus easily replaceable if necessary (with the same access restrictions discussed for the trigger summers). In addition the driver is capable of driving the coaxial lines to the L1 Calorimeter trigger. There are a total of 2,560 such drivers in 8 species (although most are of two types).

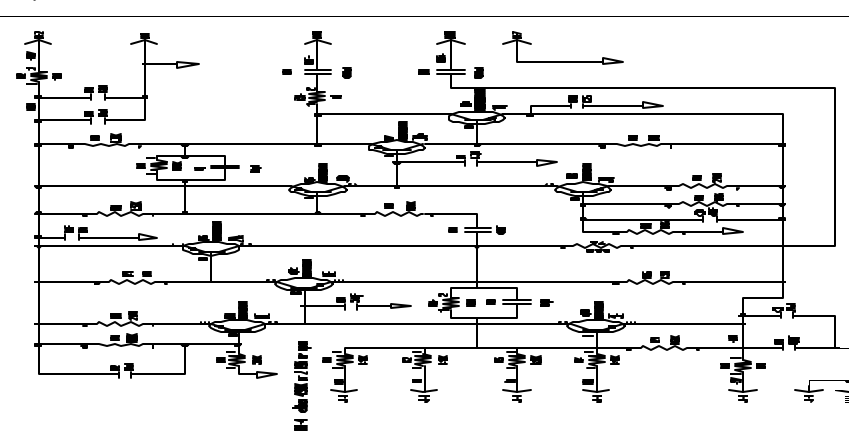


Figure 17. Schematic of the trigger sum driver hybrid. This circuit sums the outputs of up to 4 trigger summer outputs of the type shown in Figure 16.

If finer (x2) EM granularity in  $\phi$  is required for the calorimeter trigger, these hybrids could be replaced to handle the finer segmentation, since there are two output pins on the hybrid that are connected to two coax cables. We expect about 4 man months of work to modify and replace these hybrids. If further simple shaping of the trigger signal is required it could be implemented on this circuit or at the receiver end on the L1 calorimeter trigger.

#### 4.2.5 Signal transmission, cable dispersion

The signals from the trigger driver circuits are transmitted differentially on two separate miniature coax (0.1") cables. The signal characteristics for these cables are significantly better than standard RG174 cable. However first indications are that the signal seen at the end of these cables at the input to the L1 calorimeter trigger are somewhat slower than expected (an oscilloscope trace of such a signal is shown in Figure 18 for EM and Figure 19 for HAD). The cause of the deviation from expectations is not presently known and is under investigation. It

is possible that the signal dispersion in these coaxial cables is worse than expected and possible replacements are under investigation. In any case, we must deal with these pulses that are over 400ns wide (FWHM) and thus span a few 132ns bunch crossings. While there are possible intermediate solution to deal with this signal shape for 132ns bunch crossings, the most effective treatment calls for further processing of the signal through digital filtering to extract the proper bunch crossing. This option is described in more detail in later sections.

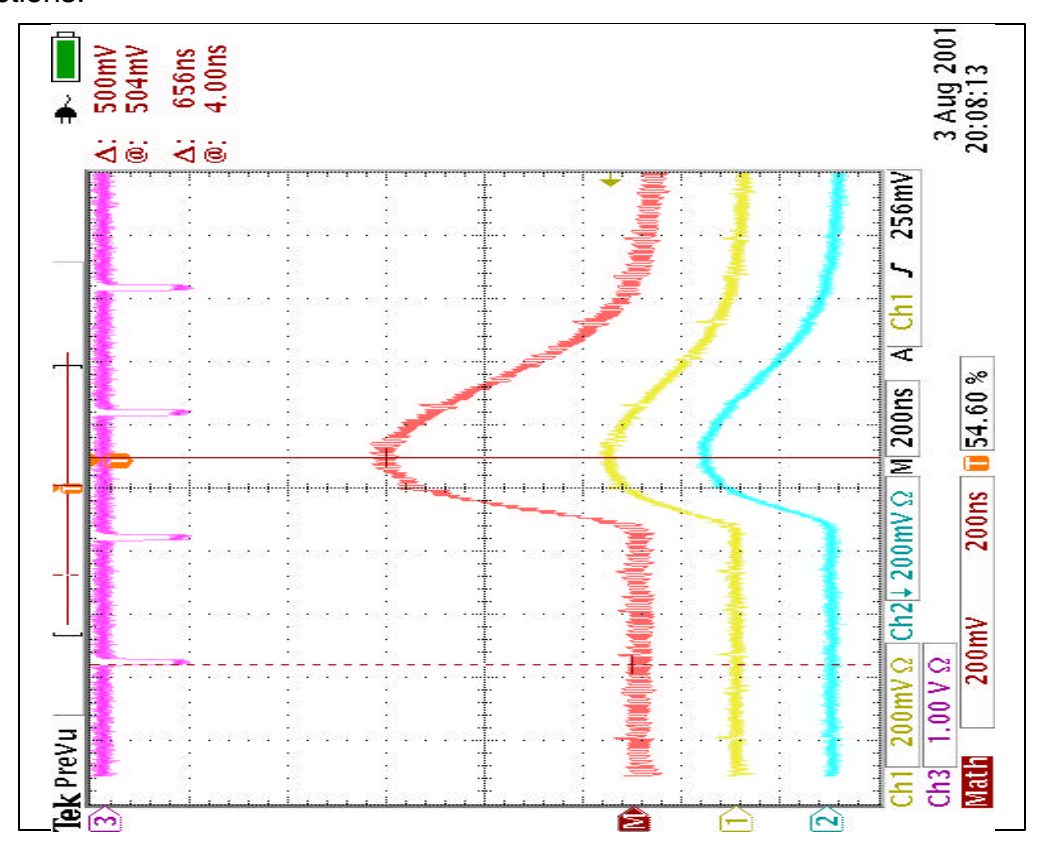


Figure 18. Actual traces of EM trigger tower (ieta=+1, iphi=17) data from the trigger sum driver signal as measured at the input to the L1 calorimeter trigger. The top trace (#3) shows the time of the beam crossings (396ns). The second trace (M) shows the addition of the two differential signals after inversion of the negative one. The third trace (#1) is the positive side of the differential pair. The fourth trace (#2) is the inverted trace for the negative side of the differential pair.

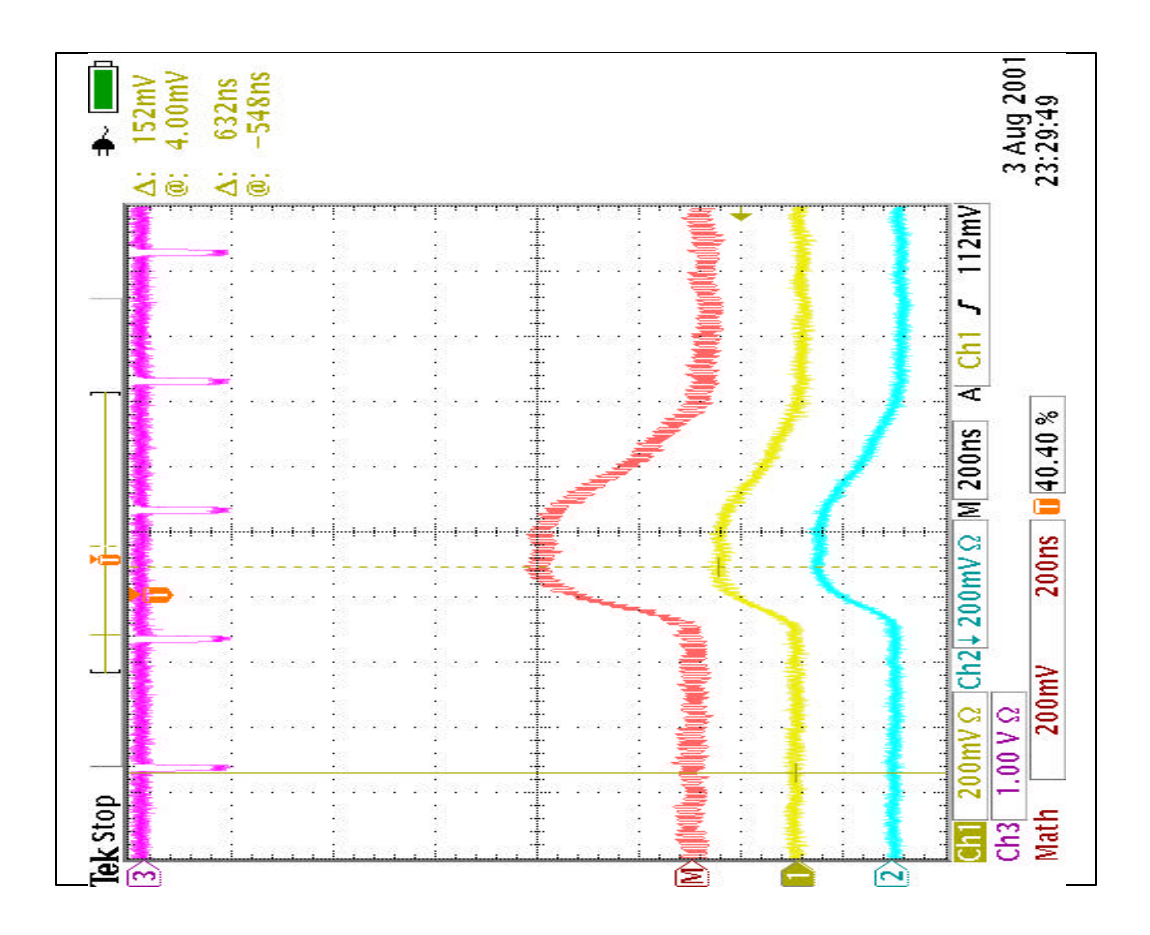


Figure 19. Actual traces of HAD trigger tower (ieta=+1, iphi=17) data from the trigger sum driver signal as measured at the input to the L1 calorimeter trigger. The top trace (#3) shows the time of the beam crossings (396ns). The second trace (M) shows the addition of the two differential signals after inversion of the negative one. The third trace (#1) is the positive side of the differential pair. The fourth trace (#2) is the inverted trace for the negative side of the differential pair.

## 4.3 Description of Current L1 Calorimeter Trigger

#### 4.3.1 Overview

The DØ uranium-liquid argon calorimeter is constructed of projective towers covering the full  $2\pi$  in the azimuthal angle,  $\phi$ , and approximately 8 units of pseudo-rapidity,  $\eta$ . There are four subdivisions along the shower development axis in the electromagnetic (EM) section, and four or five in the hadronic (H) section. The hadronic calorimeter is divided into the fine hadronic (FH) section with relatively thin uranium absorber, and the backing coarse (CH) section. In the intercryostat region  $0.8 < |\eta| < 1.6$  where the relatively thick cryostat walls give extra material for shower development, a scintillator based intercryostat detector (ICD) and extra 'masless gap' liquid argon gaps without associated absorber (MG) are located.

The calorimeter tower segmentation in  $\eta x \phi$  is 0.1 x 0.1, which results in towers whose transverse size is larger than the expected sizes of EM showers but, considerably smaller than typical sizes of jets.

As a compromise, for triggering purposes, we add four adjacent calorimeter towers to form trigger towers (TT) with a segmentation of 0.2 x 0.2 in  $\eta x \phi$ . This yields an array that is 40 in  $\eta$  and 32 in  $\phi$  or a total of 1,280 EM and 1,280 H tower energies as inputs to the L1 calorimeter trigger.

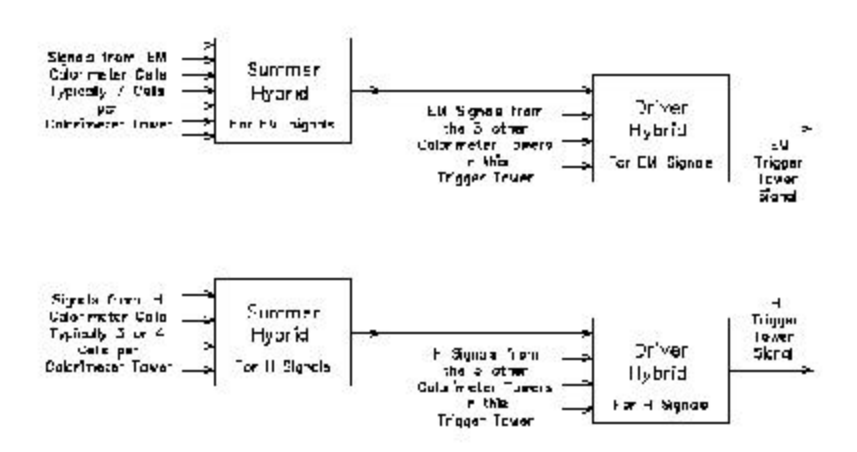


Figure 20. Trigger tower Formation.

The analog summation of the signals from the various calorimeter cells in a trigger tower into the EM and H TT signals takes place as described on page 54. This arrangement for summing the calorimeter cells into trigger towers is shown schematically in Figure 20.

Long ribbons of coaxial cable route the 1280 EM and H analog trigger tower signals from the detector platform through the shield wall and then into the first floor of the moving counting house (MCH) where the Level 1 calorimeter trigger is located. The first step in the Level 1 calorimeter trigger is to scale these signals to represent the  $E_T$  of the energy deposited in each trigger tower and then to digitize these signals at the beam-crossing rate (132ns) with fast analog to digital converters. The digital output of these 2560 converters is used by the subsequent trigger logic to form the Level 1 calorimeter trigger decision for each beam crossing. The converter outputs are also buffered and made available for readout to both the Level 2 Trigger system and the Level 3 Trigger DAQ system.

The digital logic used in the Level 1 Calorimeter Trigger is arranged in a "pipe-lined" design. Each step in the pipe-line is completed at the beam crossing rate and the length of the pipe-line is less than the maximum DØ Level 1 trigger latency for Run 2a which is 3.3  $\mu$ sec. This digital logic is used to calculate a number of quantities that are useful in triggering on specific physics processes. Among these are quantities such as the total transverse energy and the missing transverse energy, which we will designate as "global" and information relating to "local" or cluster aspects of the energy deposits in the calorimeter. The latter

would include the number of EM and H-like clusters exceeding a set of programmable thresholds.

### 4.3.2 Global Triggers

Interesting global quantities include:

the total transverse energies:

Total 
$$E_TEM = \sum_{i=1}^{1280} E_T EM_i$$

Total E<sub>T</sub>H = 
$$\sum_{i=1}^{1280} E_T H_i$$

and

Total  $E_T$  = Total  $E_T$ EM + Total  $E_T$ H

the missing transverse energy:

$$MP_T = \sqrt{(E_x^2 + E_y^2)}$$

where:

$$\mathsf{E}_{\mathsf{X}} = \sum_{i=1}^{1280} (E_{T} E M_{i} + E_{T} H_{i}) \cos(\mathbf{f}_{i})$$

and

$$\mathsf{E}_{\mathsf{y}} = \sum_{i=1}^{1280} (E_{T} E M_{i} + E_{T} H_{i}) \sin(\mathbf{f}_{i})$$

Any of these global quantities can be used in constructing triggers. Each quantity is compared to a number of thresholds and the result of these comparisons is passed to the Trigger Framework where up to 128 different Level 1 triggers can be formed.

## 4.3.3 Cluster Triggers

The DØ detector was designed with the intent of optimizing the detection of leptons, quarks and gluons. Electrons and photons will manifest themselves as localized EM energy deposits and the quarks and gluons as hadron-like clusters.

Energy deposited in a Trigger tower is called EM-like if it exceeds one of the EM  $E_T$  thresholds and if it is not vetoed by the H energy behind it. Up to four EM  $E_T$  thresholds and their associated H veto thresholds may be programmed for each of the 1280 trigger towers. Hadronic energy deposits are detected by calculating the EM  $E_T$  + H  $E_T$  of each Trigger tower and comparing each of these 1280 sums to four programmable thresholds.

The number of Trigger towers exceeding each of the four EM thresholds (and not vetoed by the H energy behind it) is calculated and these four counts are compared to a number of count thresholds. The same is done for the four EM  $E_T$  + H  $E_T$  thresholds. The results of these count comparisons on the number

of Trigger towers over each threshold is sent to the Trigger Framework where they are used to construct the Level 1 Triggers.

## 4.3.4 <u>Hardware Implementation</u>

#### 4.3.4.1 Front End Cards

The analog signals from the calorimeter, representing energies, arrive at the Calorimeter Trigger over coaxial differential signal cables and are connected to the analog front end section of a Calorimeter Trigger Front End Card (CTFE). A schematic diagram of one of the four cells of this card is shown in Figure 21.

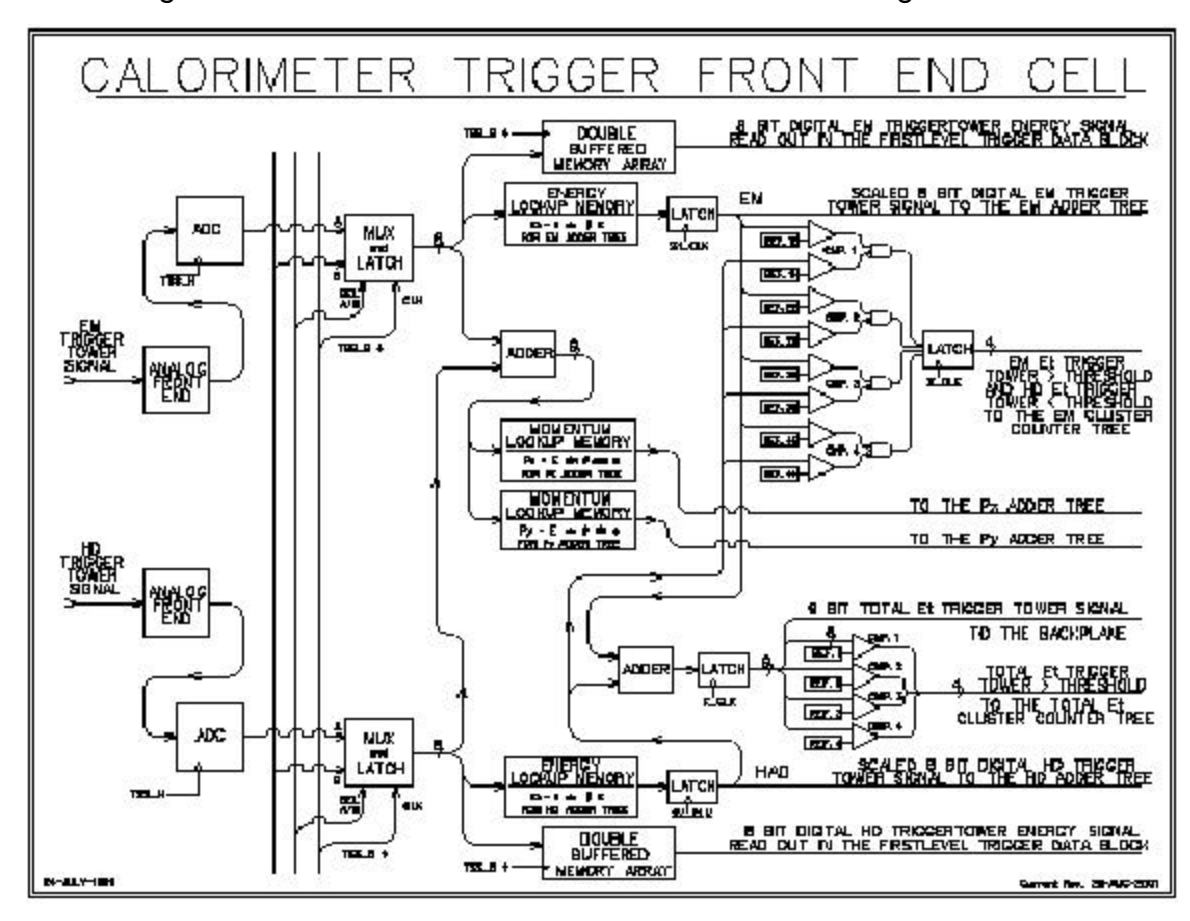


Figure 21. Calorimeter Trigger Front End Cell.

The front-end section contains a differential line receiver and scales the energy signal to its transverse component using a programmable gain stage. The front end also contains digital to analog circuitry for adding a positive bias to the tower energies in accord with downloaded values.

Immediately after the analog front end, the EM or H signal is turned into an 8 bit number by fast (20 ns from input to output) FADC's. With our current choice of 0.25 GeV least count this gives a maximum of 64 GeV for the single tower transverse energy contribution.

The data are synchronized at this point by being clocked into latches and then follow three distinct parallel paths. One of these paths leads to a pipeline

register for digital storage to await the L1 trigger decision and subsequent readout to the Level 2 Trigger system and the Level 3 Trigger DAQ system.

On the other two paths, each 8-bit signal becomes the address to a look up memory. The content of the memory at a specified address in one case is the transverse energy with all necessary corrections such as lower energy requirements etc. In the other case, the EM + H transverse energies are first added and then subjected to two look-ups to return the two Cartesian components of the transverse energy for use in constructing  $MP_T$ . The inherent flexibility of this scheme has a number of advantages: any energy dependent quantity can be generated, individual channels can be corrected or turned off at this level and arbitrary individual tower efficiencies can be accommodated.

The CTFE card performs the function of adding the  $E_T$ 's of the four individual cells for both the EM and H sections and passing the resulting sums onto the Adder Trees. In addition it tests each of the EM and EM+H tower transverse energies against the four discrete thresholds and increments the appropriate counts. These counts are passed onto the EM cluster counter trees and the total  $E_T$  counter trees, respectively.

#### 4.3.4.2 Adder and Counter Trees

The adder and counter trees are similar in that they both quickly add a large number of items to form one sum. At the end of each tree the sum is compared to a number of thresholds and the result this comparison is passed to the Trigger Framework. A typical adder tree is shown in Figure 22.

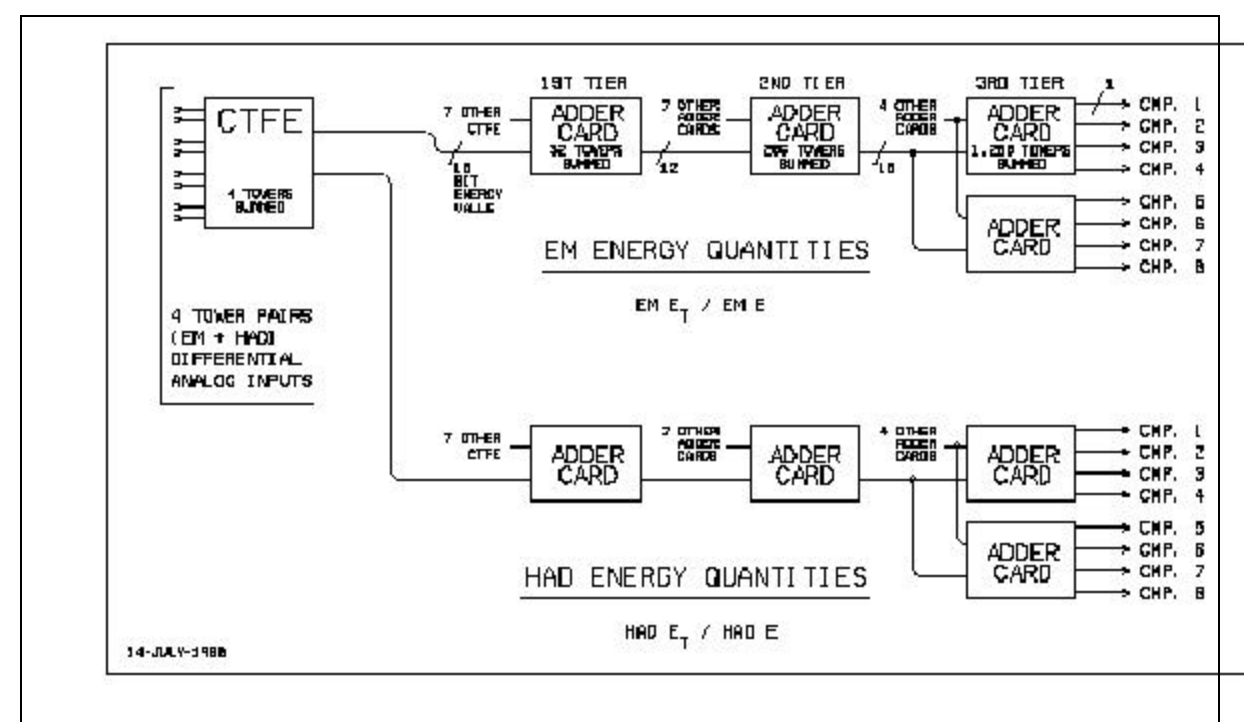


Figure 22. Adder Tree for EM and H.

### 4.3.5 Physical Layout

Ten racks are used to hold the Level 1 Calorimeter Trigger in the first floor moving counting house. The lower section of each rack contains the CTFE cards for 128 Trigger towers (all 32  $\phi$ 's for four consecutive  $\eta$ 's). The upper section of each rack contains a component of one of the Adder or Counter Trees.

## 4.4 Performance of the Current Calorimeter Trigger

In order to compare the performance of the present L1 calorimeter trigger, the following simulation is used. The jet performance is studied using a Monte-Carlo sample of QCD. A cone algorithm with a radius of 0.4 in  $\eta x \phi$  is applied to the generated stable hadrons in order to find the generated jets and their direction. The direction of each generated jet is extrapolated to the calorimeter surface; leading to the "center TT" hit by the jet (TT stands for Trigger tower). The highest  $E_T$  TT in a 3x3 trigger tower region (which is 0.6x0.6 in  $\eta x \phi$  space) around this center is then used to define the "trigger  $E_T$ " corresponding to the jet.

### 4.4.1 Energy measurement and turn-on curves

In the present L1 calorimeter trigger, the trigger towers are constructed using fixed  $\eta x \phi$  towers. Thus we expect that a trigger tower only captures a small fraction of the total jet energy since the size of the 0.2 x 0.2 trigger towers is small compared to the spatial extent of hadronic showers. This is illustrated in Figure 23, which shows, for simulated 40 GeV  $E_T$  jet events, the ratio of the  $E_T$  observed by the trigger to the generated  $E_T$ . It can be seen in Figure 23that this transverse energy is only 25% of the jet  $E_T$  on average. Therefore we must use low jet trigger thresholds if we are to be efficient even for relatively high energy jets. Moreover the trigger  $E_T$  has poor resolution, as can be seen in Figure 23. As a result, the trigger efficiency (the efficiency for having at least one TT with  $E_T$  above a given threshold) rises only slowly with increasing jet  $E_T$ , as shown in the turn-on curves in Figure 24. A similar effect occurs for the EM triggers as well; even though a typical EM shower can be reasonably well contained within a TT, often the impact point of an electron or photon is near a boundary between TTs.

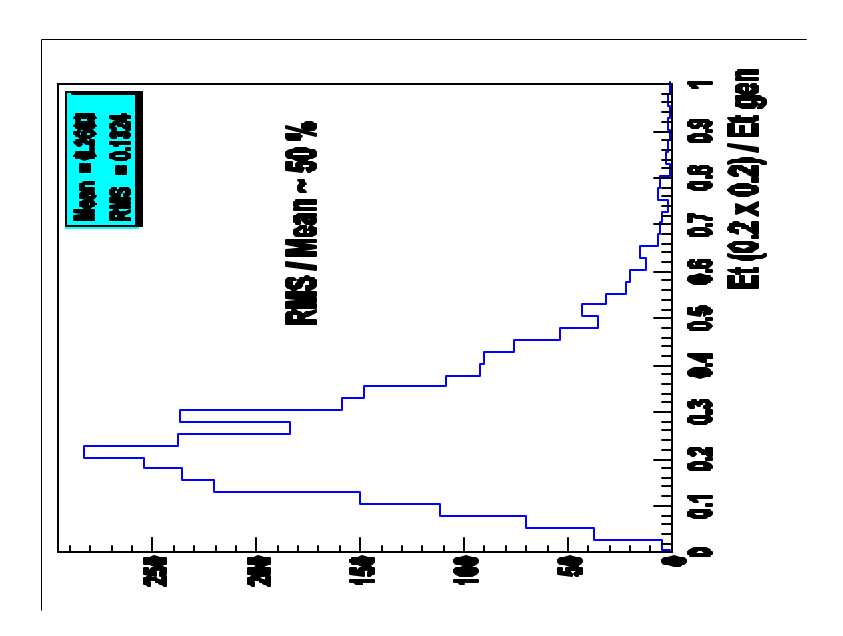


Figure 23. Ratio of the trigger  $E_T$  to the transverse energy of the generated jet. Only jets with  $E_T \approx 40$  GeV are used in this figure.

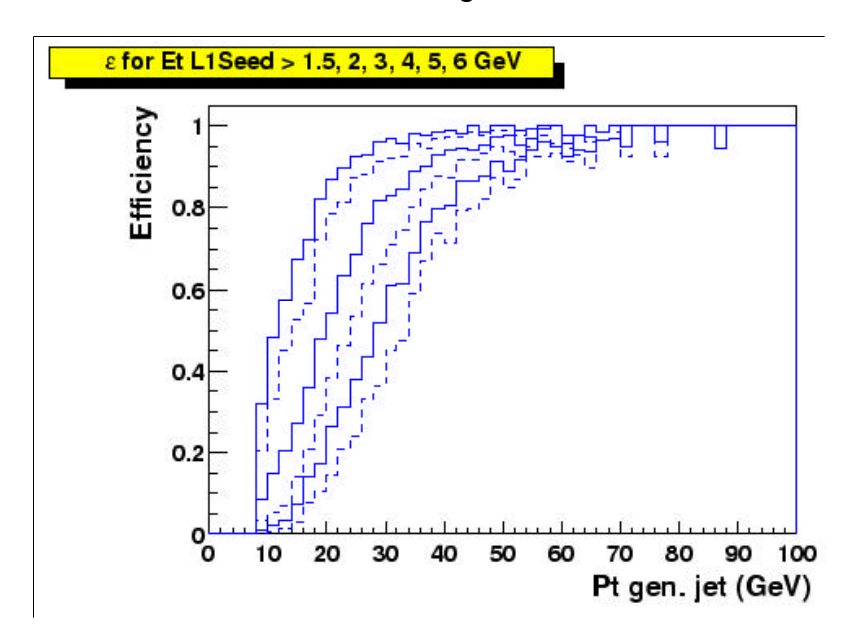


Figure 24. Trigger efficiency as a function of the transverse energy of the generated jet. The curves correspond to thresholds of 1.5, 2, 3, 4, 5 and 6 GeV (respectively from left to right).

# 4.4.2 <u>Trigger rates</u>

The trigger  $E_T$  resolution, convoluted with the steeply falling  $p_T$  spectrum of QCD events, leads to, on average, the "promotion" of events to larger  $E_T$ 's than the actual  $E_T$ . The number of QCD events which pass the L1 trigger is thus larger

than what it would be with an ideal trigger E<sub>T</sub> measurement. Due to the very large cross-section for QCD processes, this results in large trigger rates<sup>4</sup>. example, as shown in Figure 25, an inclusive unprescaled high E<sub>1</sub> jet trigger, requiring at least one TT above a threshold defined such that the efficiency for 40 GeV jets is 90%, would yield a rate for passing the L1 calorimeter trigger of at least 10 kHz at 2x10<sup>32</sup> cm<sup>2</sup> s<sup>-1</sup>. Maintaining this rate below 1 kHz would imply an efficiency on such high E<sub>T</sub> jets of only 60%. Trigger rates increase faster than the luminosity due to the increasing mean number of interactions per bunch crossing. Trigger rates are shown in Figure 26 as a function of the mean number of minimum bias events which pile up on the high  $p_T$  interaction. These are shown for two multi-jet triggers: the first requiring at least two TT above 5 GeV (indicated as CJT(2,5)); the second requiring at least two TT above 5 GeV and at least one TT above 7 GeV (indicated as CJT(1,7)\*CJT(2,5)). These triggers correspond to reasonable requirements for high p<sub>T</sub> jets because, as can be seen in Figure 25, a threshold of 5 GeV leads, for 40 GeV jets, to an 80 % efficiency. The rates in Figure 26 are shown for a luminosity of 2 10<sup>32</sup> cm<sup>-2</sup> s<sup>-1</sup>. For the higher luminosity of 5 10<sup>32</sup> cm<sup>2</sup> s<sup>-1</sup> expected in Run 2b, the L1 bandwidth would be saturated by such dijet conditions alone, unless large prescale factors are applied.

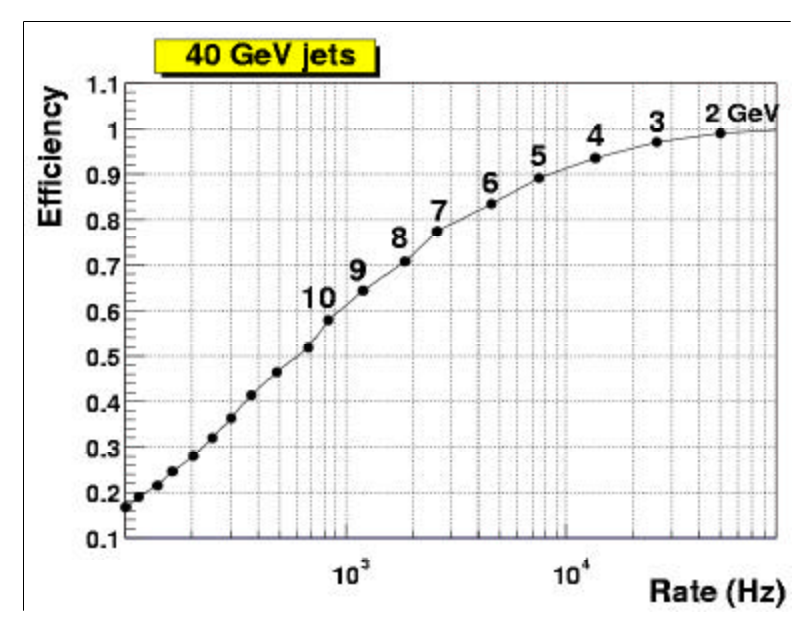


Figure 25. Efficiency to trigger on 40 GeV jets as a function of the inclusive trigger rate, when one TT above a given threshold is required. Each dot corresponds to a different threshold as indicated. The luminosity is 2x10<sup>32</sup> cm<sup>-2</sup> s<sup>-1</sup>

<sup>&</sup>lt;sup>4</sup> These rates are estimated here from samples of Monte-Carlo QCD events, passed through a simulation of the trigger response.

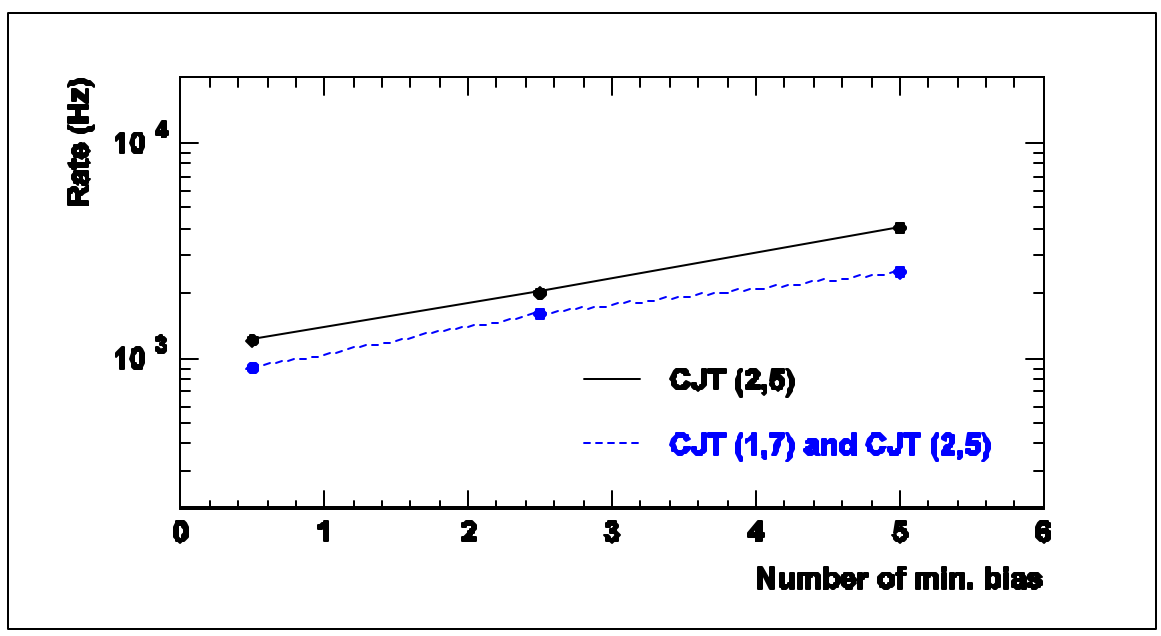


Figure 26. The inclusive trigger rate as a function of the mean number of minimum bias events overlaid on the high  $p_T$  interaction. The rates are shown for two di-jet trigger conditions corresponding to two TTs above 5 GeV (CJT(2,5)) and two TTs with above 5GeV and at least one above 7 GeV (CJT(1,7)\*CJT(2,5)). The luminosity is  $2x10^{32}$  cm<sup>-2</sup> s<sup>-1</sup>.

A more exhaustive study of the evolution of the L1 trigger rate with increasing luminosity has been carried out<sup>5</sup>. In that document a possible trigger menu was considered, in which ~75 % of the L1 bandwidth is used by multijet triggers. Results are shown in Table 12. It can be seen that, at the luminosity foreseen for Run 2b, the trigger rates should be reduced by at least a factor of two in order to maintain a reasonably small dead time.

Table 12. The overall level 1 trigger rates as a function of luminosity.

Luminosity	High Pt L1 rate (Hz)	Total L1 rate (Hz)
1x10 <sup>32</sup> cm <sup>-2</sup> s <sup>-1</sup> .	1,700	5,000
2x10 <sup>32</sup> cm <sup>-2</sup> s <sup>-1</sup> .	4,300	9,500
5x10 <sup>32</sup> cm <sup>-2</sup> s <sup>-1</sup> .	6,500	20,000

# 4.4.3 Conclusions/implications for high luminosity

From these studies, it is clear that there is a need to significantly improve the rejection of the L1 calorimeter trigger (while maintaining good efficiency) if we are to access the physics of Run 2b. One obvious way to help achieve this is to migrate the tools used at L2 (from Run 2a) into L1. In particular, the ability to

\_

<sup>&</sup>lt;sup>5</sup> B. Bhattacharjee, PhD Thesis.

trigger on "objects" such as electromagnetic showers and jets would help significantly. The "clustering" of TT at L1, could reduce the trigger rates by a factor 2 to 4 as will be shown later. The principal reason for this gain comes from the improvement in the quality of the energy cut, when applied to a cluster of trigger towers. Transferring to level 1 some of the functions that currently belong to level 2 would also permit the introduction of new selection algorithms at the L1 trigger level. So while it is clear that there are additional gains to be made through EM trigger tower shape cuts and missing  $E_T$  filtering, they will require further study to quantify the specific gains. These studies remain to be done.

From a conceptual viewpoint, an important consequence of selecting physics "objects" at level 1 is that it allows a more "inclusive" and hence less biased selection of signatures for the more complicated decays to be studied in Run 2b. Thus we expect that the trigger menus will become simpler and, above all, less sensitive to biases arising from the combinations of primary objects.

## 4.5 Overview of Options for Improvement

## 4.5.1 Global view of options considered

To accomplish the goals listed above, the L1 calorimeter trigger will need to be completely replaced – it is not possible to modify the existing trigger to incorporate the new features. We have studied various ways to improve the L1 rejection rates. Although a final design implementation is not complete, we discuss these in turn below. They include:

- the necessary hardware improvements in filtering to allow proper triggering on the correct bunch crossing;
- studies of the gains from a "sliding window" algorithm for jets and electrons;
- the ability to better correlate tracks from the fiber tracker to calorimeter trigger towers;
- the addition of presently unused calorimeter energy information from the intercryostat region (ICR) region and massless gaps (MG) in the L1 trigger;
- optimizing trigger tower thresholds;
- some topological cuts.

Following the discussion of each of these improvements, we outline an implementation that can provide the upgraded calorimeter trigger, with an estimate of the scale of cost and resources needed to accomplish it.

### 4.6 Digital Filtering

### 4.6.1 Concept & physics implications

The pulse shape, and particularly the rise time, of the trigger pickoff signal is not optimized for 132ns beam bunch crossing operation (see Figure 18 and Figure 19). Since the trigger pickoff pulse width significantly exceeds the 132ns bunch spacing time of Run 2b, the ability to correctly identify the correct trigger bunch crossing is compromised. There may be intermediate solutions to address this problem at the lower luminosities, but the only reasonable long-term solution is to apply more stringent shaping. This could be done by means of an analog filter with shorter shaping, but this is only achieved with a further loss in signal. A digital filter is a better solution because it is much more flexible for a similar cost.

The trigger pickoff signal is at the end of the calorimeter electronic chain described above. The ideal energy deposition shape is a "saw-tooth" (infinitely fast rise and a linear ~400ns fall) pulse from energy deposited in the cells of the calorimeter at each beam crossing. This is modified by the transfer function of the electronics. The inverse transfer function will transform the pickoff signal back to original energy deposition pulse shape. This inverse function can be implemented by a FIR (Finite Impulse Response) filter. In the presence of noise, the digital filter offers an additional advantage: one can use the theory of *optimal filtering* to minimize the noise contribution.

In order to define the exact form of a digital filter best suited to the task, a measurement of noise in the trigger pickoff signals is needed. As such measurements become available, a refined design will be undertaken.

## 4.6.2 Pileup rejection

Two different "pile-up" effects arise with increasing luminosity, the first being of physical origin, and the second affecting the signal measurement:

In the first case, we find that as the luminosity increases, then for each triggered beam crossing there are several minimum bias events that appear in that same beam crossing. The number of such additional events is Poisson distributed with a mean proportional to the luminosity. The energy added by these events has a distribution close to that of a double exponential (Laplacian). It is possible to minimize the contribution of this noise by using an appropriate digital filter (Matched Median Filter).

In the second case, because the width of the pick-up signal extends over several beam crossing (6 at 132ns on the positive side of the signal), then when two such pulses are close in time, there is some overlap and thus the shape of the pickoff signal becomes more complicated than that of a single isolated pulse. The inverse filter, by definition, will extract from this signal the two original pulses. Consequently, the problems caused by overlapping pulses are minimized if one uses digital filtering.

#### 4.6.3 Simulation

Simulations of the FIR response will be performed once the noise measurements are obtained. These simulations will result in a set of coefficients for the filter algorithm. The most reasonable way to compute coefficients is to use the mean squared (LMS) optimization. This proceeds by minimizing the sum of the square of the differences between many input excitations and their filtered outputs; each input excitation produces a pulse at the input of the ADC and contributes several terms to the sum: one for each beam crossing where the pulse is non-zero. A realistic simulation of the noise must be added to the theoretical pulse (derived from the transfer function of the calorimeter).

### 4.6.4 <u>Implementation</u>

An effective range of 8 bits for the transverse energy of each trigger tower seems sufficient to meet the desired performance and is technically practical. The calorimeter pulses are proportional to the energy deposited in the calorimeter while the trigger algorithms use transverse energy (rather than energy) in their calculations. Thus the L1 calorimeter trigger must convert the calorimeter energy measurements to transverse energy. It is possible to carry out this conversion with a programmable analog circuit placed in front of each ADC but a digital solution is more practical and flexible. In order to preserve a dynamic range of 8 effective bits for signals in transverse energy, one should use a 10 bit ADC to digitize the analog energy signals.

The conversion rate needs to be at least equal to the beam-crossing rate, but it can be higher than that. On the other hand, if the over-sampling rate is too high, then it does not provide any more improvement because of the relatively slow input signals from the trigger sum drivers.

Such 10 bit ADCs have a "pipelined" architecture, with a latency of 4 to 6 cycles. Since the level 1 trigger operates on a very tight latency budget, one is driven to conversion rates that are larger than the beam-crossing rate because otherwise the data conversion would have too large a latency. ADCs in the 20-60 MHz range are now common and inexpensive. If only a fraction of the samples produced by each ADC are required for filtering, then the additional samples can be ignored. One should note that because the signal may be over-sampled, then it would seem natural to use that data to improve the overall performance of the digital filtering operation. Recalling Shannon's sampling theorem, it can be shown that a FIR filter implementation of the exact inverse transfer function considered must have at least a sampling frequency that is twice that of the beam crossing. However in this particular application where the trigger sum pickoff signal is relatively slow, the over-sampling may not provide much benefit. Further study is needed.

#### 4.6.5 Conclusions

Given the relatively slow trigger sum driver pulse shapes observed in Figure 18 and Figure 19, we believe that a digital filter is required to suppress the contributions from signals in nearby bunch crossings to that containing a high pT

trigger. The exact implementation details and the final performance specifications require further study.

## 4.7 Sliding Trigger tower Windows for Jets and Electrons

A "sliding window" algorithm has the potential to significantly sharpen the trigger turn on curves.

### 4.7.1 Concept & physics implications

Various algorithms can be used to cluster the trigger towers and look for "regions of interest" (RoI), i.e. for regions of fixed size, S, in  $\eta x \phi$  in which the deposited  $E_T$  has a local maximum. To find those RoIs, a window of size S is shifted in both directions by steps of 0.2 in  $\eta$  and  $\phi$ . By convention each window unambiguously anchored on one trigger tower T and is labeled S(T). Examples are shown in Figure 27.

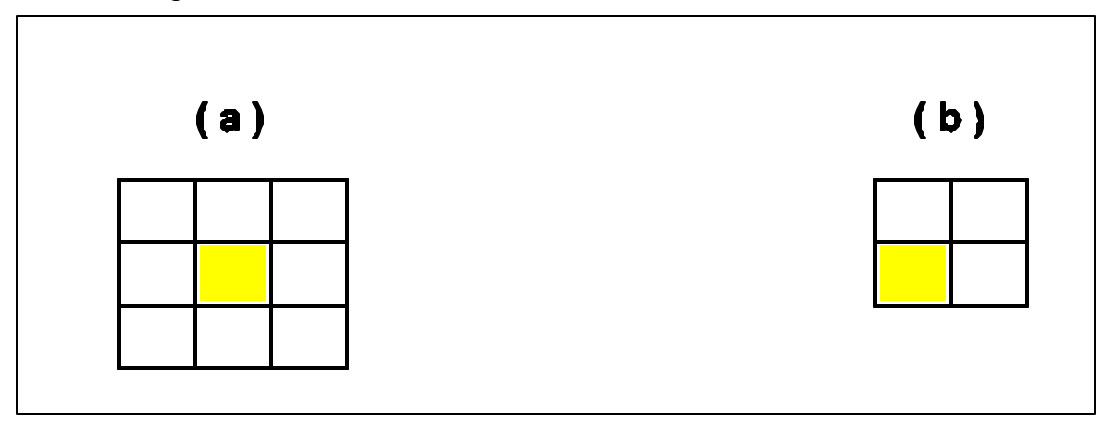


Figure 27. Examples of (a) a 3x3 and (b) 2x2 sliding window S(T) associated to a trigger tower T. Each square represents a  $0.2 \times 0.2$  trigger tower. The trigger tower T is shown as the shaded region.

The sliding tower algorithm aims to find the optimum region of the calorimeter for inclusion of energy from jets (or EM objects) by moving a window grid across the calorimeter  $\eta$ ,  $\phi$  space so as to maximize the transverse energy seen within the window. The window of towers so found, together perhaps with a specified set of neighbors, is called the region of interest, R, and is referenced by a specific TT within R as indicated in Fig. 15 for a 3x3 or a 2x2 window. The total  $E_T$  within R and in the defined neighbor region is termed the trigger  $E_T$  relevant to the jet or EM object. A specific example of how the local maximum could be defined is shown in Figure 28.

2	>	>	>	>
N	2	>	>	>
2	2	S (T)	>	>
2	2	2	>	>
2	2	2	2	>

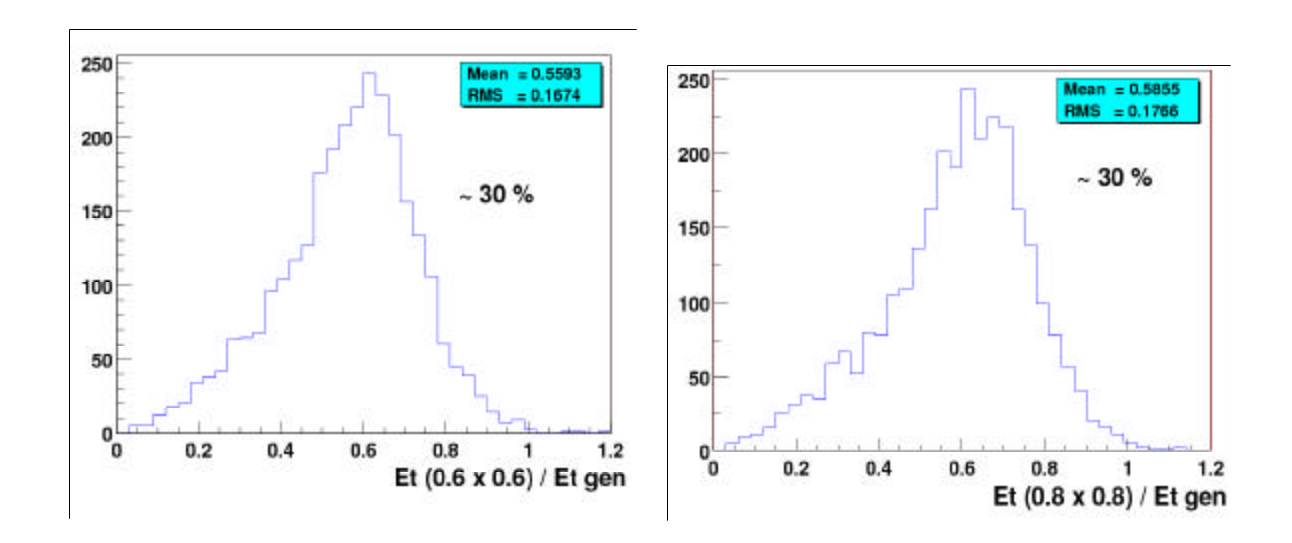
Figure 28. An illustration of a possible definition of a local  $E_T$  maximum for a R candidate. The 0.2x0.2 cluster is accepted if it is more energetic than the neighboring clusters marked as ">" and at least as energetic as those marked " $\geq$ ". This method resolves the ambiguities when two equal clusters are seen in the data.

#### 4.7.2 Simulation

Several algorithms defining the regions of interest have been considered and their performance has been compared using samples of simulated events:

- a) The R size is 0.6 x 0.6 (Figure 27a) and the trigger  $E_T$  is the  $E_T$  contained in the Rol.
- b) The R size is 0.4 x 0.4 (Figure 27b) and the trigger  $E_T$  is the  $E_T$  contained in the 0.8 x 0.8 region around the Rol.
- c) The R size is 1.0 x 1.0 and the trigger  $E_T$  is the  $E_T$  contained in the R.

In each case, the algorithm illustrated in Figure 28 is used to find the local maxima R. For each algorithm, the transverse energy seen by the trigger for 40 GeV jets is shown in Figure 29. This is to be compared with Figure 23, which shows the  $E_T$  seen by the current trigger. Clearly, any of the "sliding window" algorithms considerably improve the resolution of the trigger  $E_T$ . For the case of the 40 GeV jets studied here, the resolution improves from an rms of about 50% of the mean (for a fixed  $0.2x0.2~\eta x \phi$ ?trigger tower) to an rms of 30% of the mean (for a sliding window algorithm), and the average energy measured in the trigger tower increases from ~26% to 56-63% (depending on the specific algorithm).



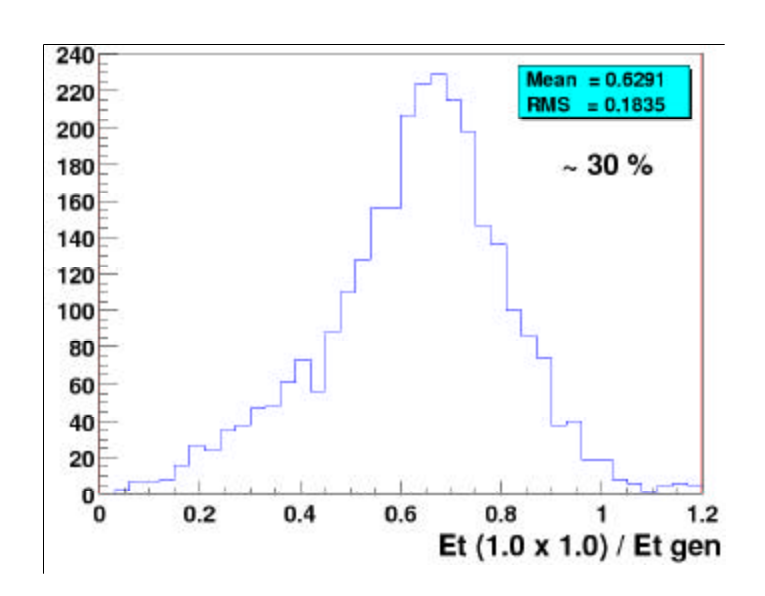


Figure 29. Ratio of the trigger  $E_T$  to the transverse energy of the generated jet, using three different algorithms to define the regions of interest. Only jets with  $E_T \approx 40$  GeV are used here. The ratio of the rms to the mean of the distribution ,the value 30%, is written on each plot.

Since the observed resolution is similar for all three algorithms considered, then the choice of the *R* definition (i.e. of the algorithm) will be driven by other considerations including hardware implementation or additional performance studies. In the following, we will only consider the (b) algorithm.

## 4.7.3 Efficiency

The simulated trigger efficiency for the (b) algorithm, with a threshold set at 10 GeV, is shown as a function of the generated  $E_T$  in Figure 30. The turn-on of the efficiency curve as a function of  $E_T$  is significantly faster than that of the

current trigger, also shown in Figure 30 for two values of the threshold. With a 10 GeV threshold, an efficiency of 80% is obtained for jets with  $E_T$  larger than 25 GeV.

In order to understand which part of these new algorithms are providing the improvement (the sliding window or the increased trigger tower size), we have studied the gain in efficiency which is specifically due to the sliding window procedure by considering an algorithm where the TTs are clustered in fixed 4 x 4 towers (i.e. 0.8x0.8 in  $\eta x \phi$ ), without any overlap in  $\eta$  or  $\phi$ . The comparison of the "fixed" and "sliding" algorithms is shown in Figure 31. One observes a marked improvement for the "sliding" windows compared to the "fixed" towers, indicating that the added complexity of implementing sliding windows is warranted.

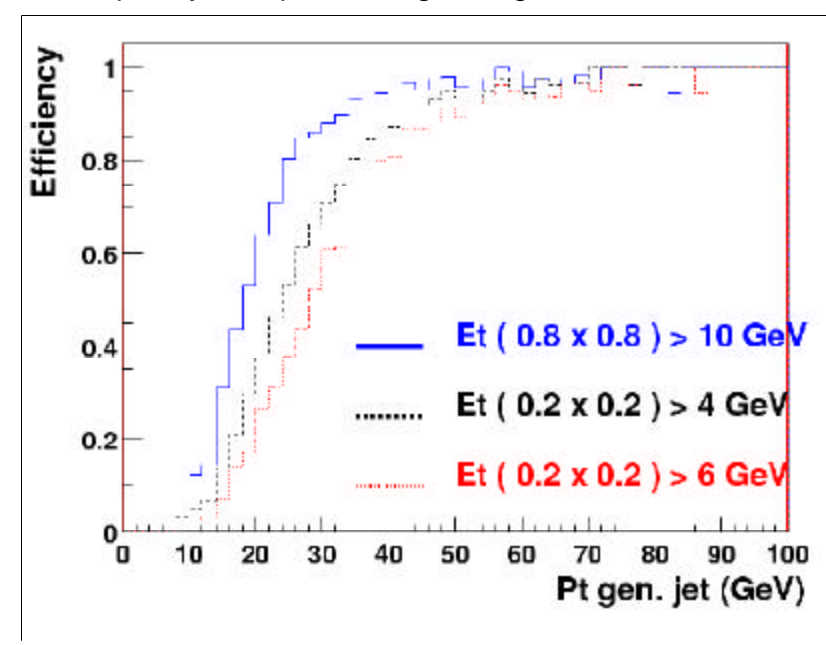


Figure 30. Trigger efficiency as a function of the transverse energy of the generated jet, for the (b) algorithm for  $E_T > 10$  GeV (the solid line) and for the current trigger (fixed trigger towers with thresholds of 4 and 6 GeV shown as dashed and dotted lines respectively).

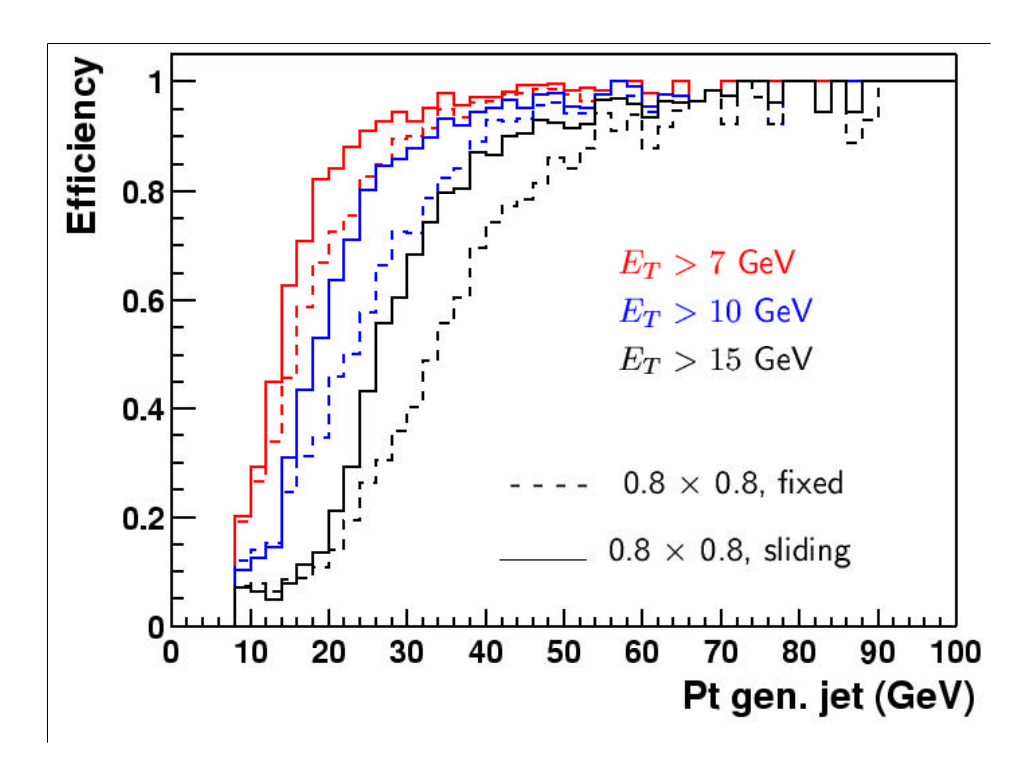


Figure 31. Trigger efficiencies as a function of the generated jet  $p_T$  for trigger thesholds  $E_T > 7 \, \text{GeV}$ , 10 GeV and 15 GeV (curves from right to left respectively). The solid curves are for the 0.8 x 0.8 "sliding window" algorithm, and the dashed curves are for a fixed 0.8 x 0.8 trigger tower in  $\eta x \phi$ .

# 4.7.4 Rates and rejection improvements

In this section, we compare the performance of the sliding window and the existing trigger algorithms. We compare both of these algorithms' trigger efficiencies and the associated rates from QCD jet events as a function of trigger  $E_{\mathsf{T}}$ .

In these studies we require that for the sliding window (b) algorithm there be at least one Rol with a trigger E<sub>T</sub> above threshold which varies from 5 to 40 GeV in steps of 1 GeV. Similarly, for the current trigger algorithm, we require at least one TT above threshold which varies from 2 GeV to 20 GeV in steps of 1 GeV. For both algorithms and for each threshold, we calculate the corresponding inclusive trigger rate and the efficiency to trigger on relatively hard QCD events, i.e. with parton  $p_T > 20$ GeV and  $p_T > 40$ GeV respectively. To simulate high luminosity running, we overlay additional minimum bias events (a mean of 2.5 or 5 additional minimum bias events) in the Monte Carlo sample used to calculate the rates and efficiencies. While the absolute rates may not be completely reliable given the approximate nature of the simulation, we believe that the relative rates are reliable estimators of the performance of the trigger algorithms. Focusing on the region of moderate rates and reasonable efficiencies, the results are plotted in Figure 32 where lower curves (dashed line) in the plots is for the current trigger algorithm and the upper curve (solid line) corresponds to the sliding window (b) algorithm. It is apparent from Figure 32 the sliding window

algorithm can reduce the inclusive rate by a factor of 2 to 4 for any given efficiency. It is even more effective at higher luminosities (i.e. for the plots with 5 overlaid minimum bias events).

The improvement in jet triggering provided by the proposed algorithm is important for those physics processes that do not contain a high  $p_T$  lepton. Since the sliding window algorithm would be implemented in FPGA-type logic devices, it opens up the possibility of including further refinements in the level of trigger sophistication, well beyond simple counting of the number of towers above threshold. We have studied the trigger for two processes which demonstrate the gains to be expected from a sliding window trigger over the current trigger:

- The production of a Higgs boson in association with a b-bbar pair. This process can have a significant cross-section in supersymmetric models with large tanβ, where the Yukawa coupling of the b quark is enhanced. Thus when the Higgs decays into two b quarks this leads to a 4b signature. The final state contains two hard jets (from the Higgs decay) accompanied by two much softer jets. Such events could easily be separated from the QCD background in off-line analyses using b-tagging. But it will be challenging to efficiently trigger on these events while retaining low inclusive trigger rates.
- The associated production of a Higgs with a Z boson, followed by H → bb and Z →vv. With the current algorithm, these events could be triggered on using a di-jet + missing energy requirement. The threshold on the missing energy could be lowered if a more selective jet trigger were available.

Figure 33 shows the efficiency versus inclusive rate for these two processes, where three different trigger conditions are used:

- 1. At least two fixed trigger towers of 0.2 x 0.2 above a given threshold.
- 2. At least one TT above 10 GeV and two TT above a given threshold.
- 3. At least two "trigger jets" whose summed trigger  $E_T$ 's are above a given threshold.

It can be seen that the third condition is the most efficient for selecting signal with high efficiency but low rates from QCD jet processes.

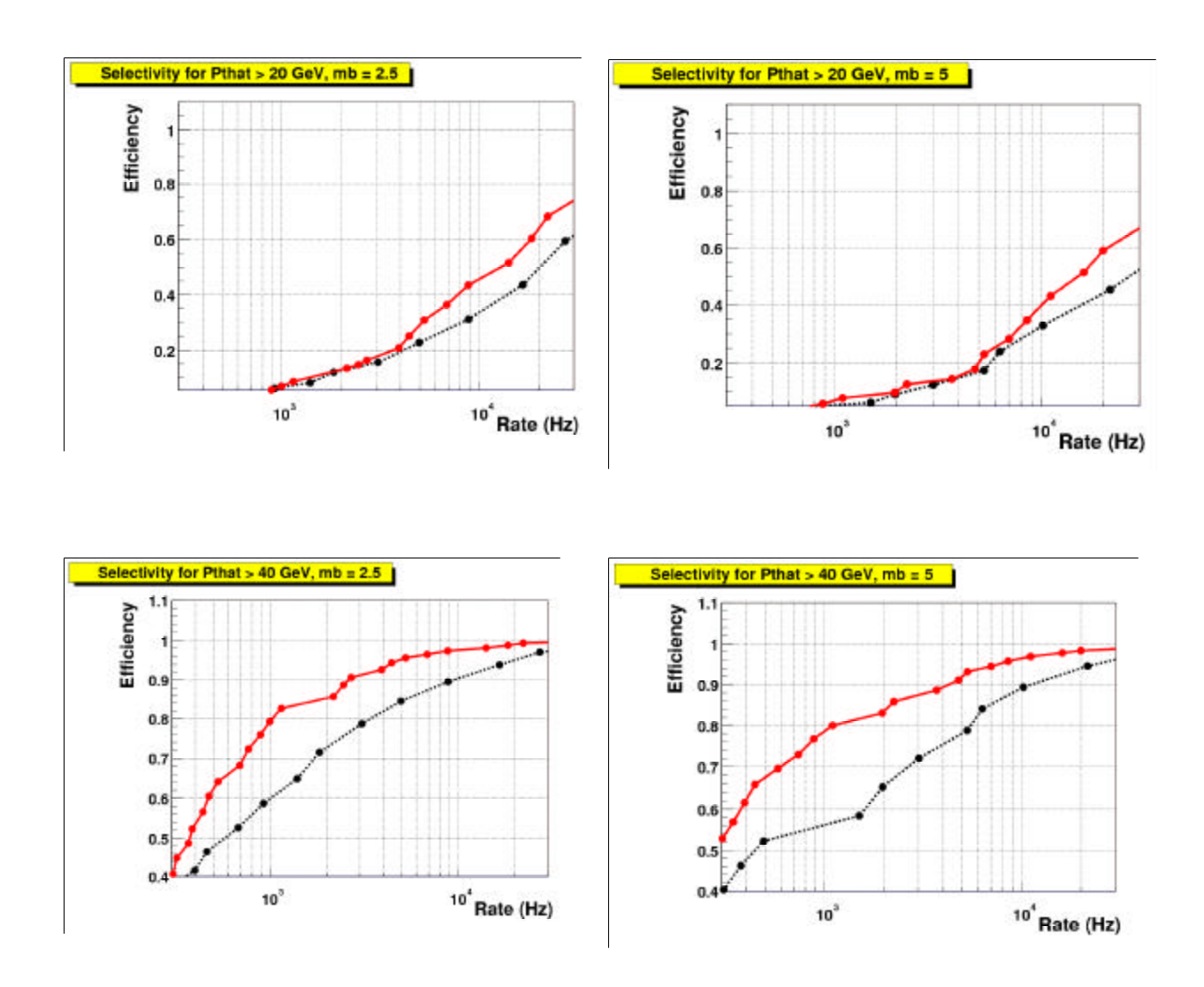


Figure 32. Trigger efficiency for events with parton  $p_T > 20$  GeV (top) and parton  $p_T > 40$  GeV (bottom) as a function of the inclusive trigger rate, for the (b) algorithm (solid curves) and the current algorithm (dashed curves). Each dot on the curves corresponds to a different trigger threshold. The luminosity is 2  $10^{32}$  cm<sup>-2</sup> s<sup>-1</sup> and the number of overlaid minimum bias events follows a Poisson distribution of mean equal to 2.5 (upper plots) or to 5 (lower plots).

# 4.7.5 <u>Implementation</u>

These triggering algorithms can be implemented in Field Programmable Gate Arrays on logical processing cards. Each of these cards has responsibility for a region of the calorimeter. Necessarily, there are overlapping areas of these regions as the algorithms must see data belonging to neighboring towers to the tower being analyzed. We can assume that for the processing of one tower, it is

necessary to have access to data from a region of maximum size  $(\Delta \eta \times \Delta \phi) = 1.0$  x 1.0 centered on the tower. This mandates overlap regions of size  $\Delta \eta/\Delta \phi = 1.6$  or  $\Delta \eta/\Delta \phi = 0.8$  between processing cards, depending on the ultimate  $\phi$  segmentation.

We estimate that the size of electronic circuits available in one year will be large enough to contain the algorithms for a region  $(\Delta \eta \times \Delta \phi) = 4.0 \times 1.6$ . Choosing the largest possible elementary region has the salutary consequence of minimizing the duplication of data among cards. With this choice, the new trigger system will consist of only eight logical processing cards (to be compared with the more than 400 cards in the old system).

### 4.7.6 Conclusions

The improvement in the trigger turn on curves and the reduction of QCD backgrounds lead us to conclude that a sliding window trigger algorithm should be adopted for Run 2b. The details of the implementation will require further study.

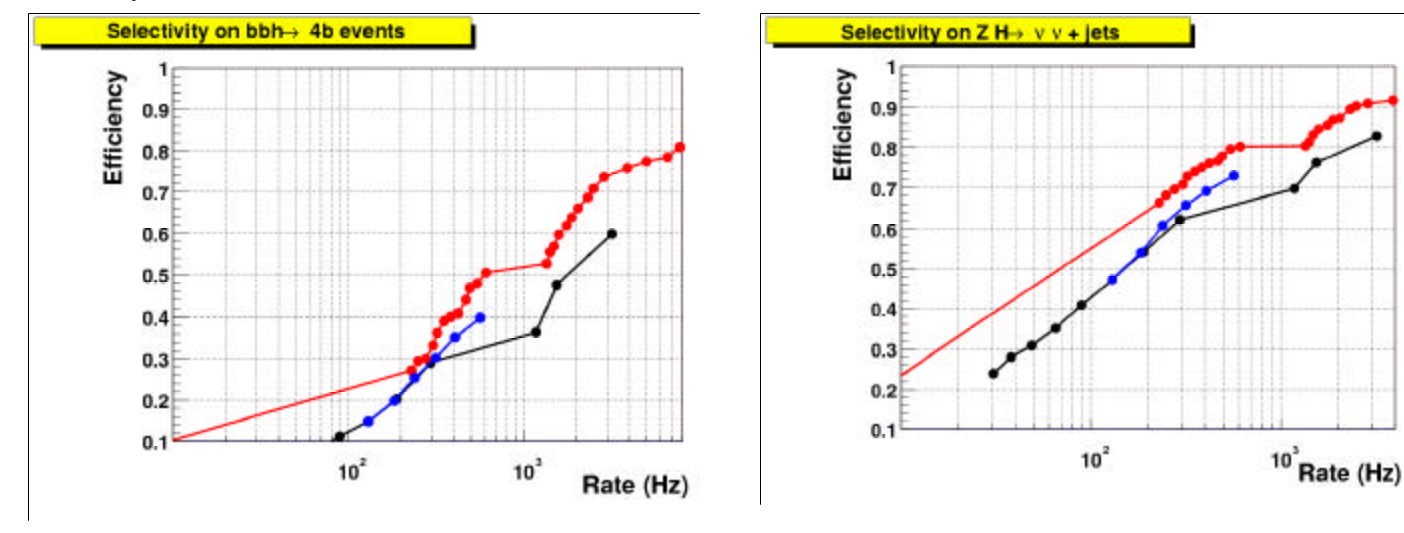


Figure 33. Efficiency to trigger on bbh (left) and ZH (right) events as a function of the inclusive rate. The three conditions shown require: at least two TT above a threshold (black curves), at least one TT above 10 GeV and two TT above a threshold (blue curves), at least two trigger jets such that the sum of their trigger E<sub>T</sub>'s is above a given threshold (red curves).

## 4.8 Track Matching and Finer EM Segmentation

#### 4.8.1 Concept & physics implications

The capability to match tracks that are found in the central fiber tracker (CFT) with trigger towers (TT) in the calorimeter is available at a very coarse level in the

Run2a detector. The matching of calorimeter trigger towers to CFT tracks is limited to  $\phi$  quadrants and takes up valuable "and-or" in terms in the trigger framework (TFW). In this section we explore the benefits of significantly increasing the CFT  $\phi$  granularity used in track matching to the much finer level of track sectors. For comparison we have also studied the gains that can be achieved with the much coarser available quadrants (rather than the finer track sectors). Such an upgrade would be a significant augmentation of the DØ detector's triggering ability, which may provide a crucial handle to some of the more difficult but desirable physics we wish to study in Run2b, such as H $\rightarrow \tau\tau$ .

### 4.8.2 Simulation

In this section, we consider first the problem of a calorimeter-centric trigger in which thresholds are placed on tower EM  $E_T$ , and ask what the gains are by matching to tracks. The calorimeter trigger granularity is currently 2.5 times coarser in  $\phi$  than one tracking sector. For most of the results reported here, we have matched all three of the sectors which at least partially overlap a trigger tower. If there is at least one track with  $p_T>1.5$  GeV pointing at the trigger tower, we consider there to be a match. In our studies for this section, we have utilized five QCD samples. Four of these were generated with QCD jets of  $p_T>2$  GeV, 5 GeV, 20 GeV and 80 GeV, respectively, and 0.7 min-bias interactions from ISAJET overlayed. One sample was a 20 GeV QCD sample with 5 interactions overlayed. There was also a QCD sample used with 2 GeV jets and 10 interactions from PYTHIA.

For comparison, we have also studied the gains from quadrant track matching, where we have again taken the QCD sample with jets of Pt>20 GeV and 5mb overlays. We group sectors into their respective quadrants and match these to overlapping trigger towers.

We note that in these studies there was no attempt made to simulate the sliding tower algorithm, so we might expect some improvements in the final system over what is reported here.

### 4.8.3 Rates and rejection improvements

Since triggers will likely select jets of different inherent  $P_T$ 's with several different tower  $E_T$  thresholds, we have explored the dependency of trigger tower track occupancy on these parameters (see Table 13 and Figure 34). For instance, considering trigger towers with non-zero EM+HAD  $E_T$ , we find that towers in the 2 GeV QCD sample match tracks 2.4% of the time, while 24.2% match in the 80 GeV sample. A more useful understanding for the point-of-view of the trigger can be gotten by looking at the dependence of this occupancy on tower  $E_T$  within these samples (for studies in the rest of this section, we match to EM towers).

Table 13. Trigger tower track occupancy for different tower ET thresholds and jet PT's, where the first line for every ET threshold corresponds to the total number

of towers (denominator) and the number of track-matched towers (numerator). The second line gives the fractional occupancy.

EM E <sub>T</sub> (GeV)	Jet Pt >2GeV	Jet Pt>5GeV	Jet Pt>20GeV	Jet Pt>80GeV
>0.5	9k/197k	18k/240k	42k/161k	73k/147k
	4.6%	7.5%	26.1%	49.7%
>2	69/297	300/1147	4k/7506	16k/19k
	23.2%	26.2%	53.3%	84.2%
>5	5/9	27/63	920/1587	7800/9121
	55%	42.9%	58%	85.5%
>10		3/7 42.9%	157/273 57.5%	4070/4579 88.9%

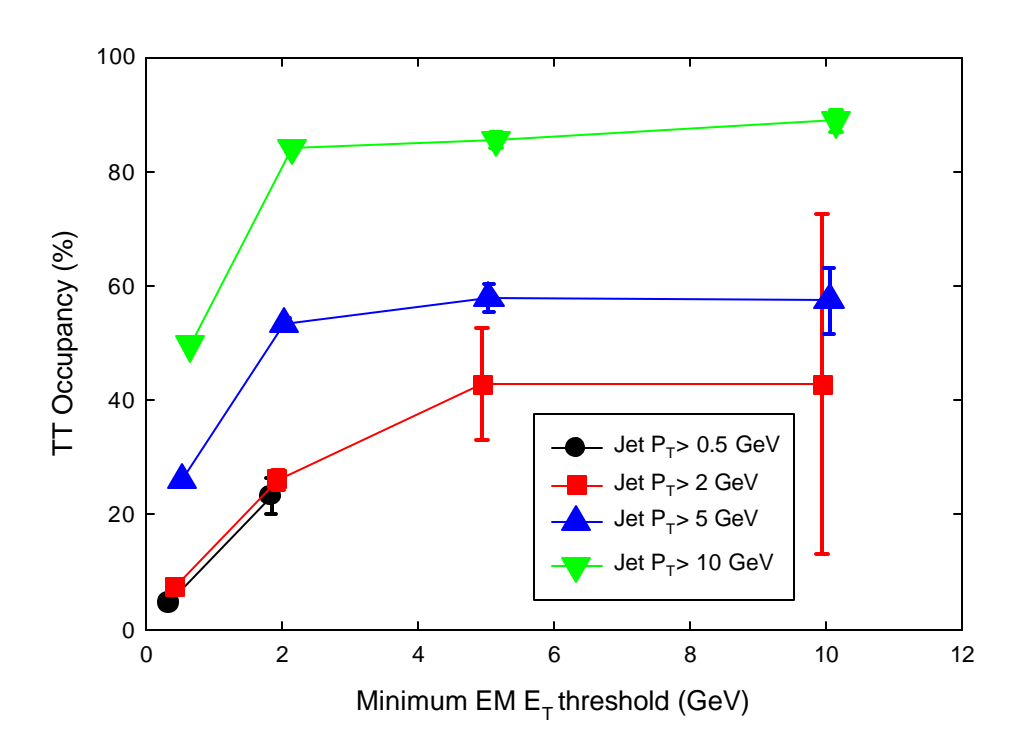


Figure 34. Trigger tower track occupancy for the values of Table 13.

Since these results are based on samples corresponding to low-luminosity conditions, it is important to ensure that these rejection factors are robust against the additional interactions that we expect to typically see. Using QCD events with parton threshold ~20GeV, we compare two samples with 0.7 and 5.0 minimum bias interactions, respectively. The results are shown in Table 14.

Table 14. Trigger tower track occupancy for 2 GeV and 20 GeV jet  $P_T$  and different tower  $E_T$  thresholds and low (average of 0.7 min bias) and high

luminosity conditions (average of 5 ISAJET minimum bias events, or 10 tuned PYTHIA minimum bias events), where the first line for every  $E_{\rm T}$  threshold corresponds to the total number of towers (denominator) and the number of track-matched towers (numerator). The second line gives the fractional occupancy. For trigger towers of  $E_{\rm T}$  greater than 2 GeV, the dependence of rejection on the number of interactions is marginal.

EM E <sub>T</sub> (GeV)	2 GeV	20 GeV	2 GeV	20 GeV
	0.7 min bias	0.7 min bias	10 min bias	5 min bias
>0.5	9k/197k	42k/161k	200k/1520k	92k/291k
	4.6%	26.1%	13.1%	32.6%
>2	69/297	4k/7506	1100/3711	2130/3482
	23.2%	53.3%	29.6%	61.2%
>5	5/9	920/1587	52/132	480/703
	55%	58%	39.4%	68.3%
>10		157/273 57.5%		96/125 76.8%

It is likely in actual triggering that the track  $P_T$  threshold used will be greater than 1.5 GeV, and more like 3 or 5 GeV, and maybe 10 GeV. Since the number of fake high  $P_T$  tracks rises dramatically with multiple interactions, we consider our 20 GeV sample with 5 minimum bias interactions. This sample has 2147 events. We calculate the matching probabilities for how many times a given TT overlaps sectors with tracks with  $P_T > 1.5$  GeV, > 3 GeV, > 5 GeV, and > 10 GeV. These results are shown in Table 15. The second half of this table indicates the analogous behavior for a 2 GeV QCD sample with 10 interactions overlaid from PYTHIA.

Table 15. Trigger tower track occupancy for 20 GeV and 2 GeV jet  $P_T$  and different tower  $E_T$  thresholds and varying track  $P_T$ 's, where the first line for every  $E_T$  threshold corresponds to the total number of towers (denominator) and the number of track-matched towers (numerator). The second line gives the fractional occupancy.

EM E <sub>T</sub> (GeV)	Track P <sub>T</sub> >1.5GeV	Track P <sub>T</sub> >3GeV	Track P <sub>T</sub> >5GeV	Track P <sub>T</sub> >10GeV		
	20 GeV jet P <sub>T</sub>					
>0.5	92k/291k 32.6%	50k/291k 17.2%	25k/291k 8.6%	15k/291k 5.2%		
>2	2130/3482 61.2%	1630/3482 46.8%	1100/3482 31.6%	400/3482 11.5%		
>5	480/703	380/703	290/703	140/703		

	68.3%	54.1%	41.3%	19.9%
>10	96/125	80/125	68/125	37/125
	76.8%	64%	54.4%	29.6%
		2 GeV jet F	Рт	
>0.5	200k/1520k	70k/1520k	30k/1520k	10k/1520k
	13.2%	4.6%	2%	0.7%
>2	1100/3711	600/3711	211/3711	60/3711
	29.6%	16.2%	5.7%	1.6%
>5	52/132	34/132	19/132	11/132
	39.4%	25.8%	14.2%	8.2%
>10	4/12	4/12	2/12	2/12
	33.3%	33.3%	1.7%	1.7%

The first column in the table is from Table 14. The first column gives the number of TTs matching tracks of the lowest  $p_T$  or greater divided by the total number of TT's of that  $E_T$ . Each of the other columns is relative to the denominator in column 1. This shows, moving left to right, that the tightening of the  $p_T$  cut does reduce the rate substantially, particularly for the lower  $p_T$  towers. In the 2 GeV sample, which is closer to the sample we will be attempting to reject at Level 1, we find that the relative rejections from tightening the track  $p_T$  threshold are much larger.

For comparison, we have also carried out a study of the relative benefits of sector-level matching of tracks to trigger towers vs. quadrant-level matching, we have again taken the QCD samples having 2 GeV jets and 10 minimum bias event overlays or 20 GeV jets and 5 minimum bias. We group sectors into their respective quadrants and match these to overlapping trigger towers. The relative rejections per trigger tower for two different track  $p_T$  thresholds of 1.5 and 10 GeV are shown in Table 16 and Table 17.

Table 16. Comparison of the rejection for track sector matching and quadrant matching with calorimeter trigger towers for the 20 GeV sample.

EM E <sub>T</sub>		p <sub>T</sub> > 1.5Ge <sup>v</sup> quadrants)	$V p_T > 10G$ (sectors)	$\text{SeV}  p_T > 10 \text{GeV}$ (quadrants)
2 GeV	2130/3482	2920	400	700
5 GeV	480/703	600	140	180
10 GeV	96/125	111	37	43

Table 17. Comparison of the rejection for track sector matching and quadrant matching with calorimeter trigger towers for the 2 GeV sample.

EM E <sub>T</sub>	Pt : 1.5GeV (sectors)	> Pt 1.5GeV (quadrants)	> Pt > 10Ge (sectors)	eV Pt > 10GeV (quadrants)
2 GeV	2470/3711	1100	225	60
5 GeV	103/132	52	21	11
10 GeV	8/12	4	2	2

This indicates that for the low  $p_T$ , high multiple interaction samples we will be trying to reject at Level 1, there are rejection factors of 2 to 3 to be gained by going to sectors matching. In the higher  $p_T$  sample, for low  $p_T$  towers, there is still up to a factor of 2 better rejection by going to sectors. In addition, we also note that the multiple interaction simulation in the 20 GeV sample case is based on the ISAJET model which is known to be a poor rendering of what we will see in the data (see the earlier sections of this document). It is very possible that the track backgrounds are significantly worse than we have seen in this study.

# 4.8.4 Track matching gains for tracking

While we have explored the issue of matching calorimeter and fiber tracker information from the starting point of triggers based mainly on calorimeter information, it is important for some physics to attempt to trigger on the tracking. Unfortunately, these triggers suffer from a large background of fake tracks, even for track  $p_T$  >10 GeV. As has been indicated elsewhere in this document, this problem worses substantially as the number of multiple interactions increases. If we look in our QCD  $p_T$  >20 GeV sample with 5mb overlay, we find that out of 2147 total events, 2105 have at lease one sector with a track of  $p_T$  >1.5 GeV. This occupancy improves only slowly with track  $p_T$  selection such that 1877, 1372, and 728 events have at least one track with  $p_T$  greater than 3, 5, and 10 GeV, respectively. For our 2GeV sample with 10mb overlays, we find that out of a total of 18500 events, 15027, 6559, 2817, and 1515 have at least one track with  $p_T$  > 1.5, 3, 5, and 10 GeV, respectively. The matching of calorimeter information has the ability to verify these tracks and also their momentum measurement.

Our matching involves considering individual sectors with at least one track of a given minimum Pt, and matching them in  $\phi$  to whatever trigger towers they overlap. By doing this, we avoid double counting some of the redundant track solutions that cluster near to each other. In about one third of the sectors, these tracks will overlap two different trigger tower  $\phi$ s, and each match is counted separately. The results of this matching are shown in Table 18.

Table 18. Number of sectors with tracks as a function of the track  $p_T$  and the calorimeter trigger tower threshold using 2 GeV and 20 GeV samples.

track Pt w	Nsct ⁄tracks	Tot $E_T > 1$ GeV	> 2 GeV	> 5 GeV	> 10 GeV
		2GeV sa	mple		
> 1.5 GeV	52991	16252	3218	200	13
> 3 GeV	12818	5188	1529	144	13
> 5 GeV	4705	1562	476	73	9
> 10 GeV	2243	655	141	31	5
		20 GeV s	ample		
> 1.5 GeV	16445	8860	4224	1279	299
> 3 GeV	7232	4639	2653	925	232
> 5 GeV	3639	2242	1347	594	166
> 10 GeV	1513	831	411	213	82

In this situation, we find substantial rejections from even mild trigger tower thresholds. For the 2 GeV sample, a 10 GeV track matching to a 5 GeV trigger tower provides a factor of  $\sim$ 70 rejection. Matching any track threshold to a 2 GeV tower provides approximately a factor of 10 rejection. For the 20 GeV sample, we find a factor of 2 or 4 reduction in background by matching a 10 GeV track to a 1 or 2 GeV trigger tower, respectively. A more likely trigger selection might have 10 GeV track and 5 GeV tower  $E_T$ , which gives a rejection of about a factor of 7.

## 4.8.5 Change of EM granularity to $\Delta \phi = 0.1$

Given the significant rejection factors and robustness to multiple interactions the sector-level matching gives, we would like to know if there is a further way of improving the rejection by segmenting the EM calorimeter towers more finely to better match the CFT granularity. Since the finer granularity causes energy sharing among neighboring towers to be large, the simplest study one could envision involves segmenting the EM energy appropriately and then crudely clustering it. Ideally, we would like to apply the moving window scheme described elsewhere, but instead for expediency we settle for this study with a simpler algorithm. We take EM trigger tower seeds above 1 GeV and add the E<sub>T</sub>'s of the surrounding eight towers. We also calculate the E<sub>T</sub> weighted phi for the cluster in this 3x3 window. This simple algorithm is applied for both the 0.2 and 0.1 granularity scenarios. Naively, we expect about a factor of 2 in improved rejection due to the improved geometry. In practice, the granularity has

an effect on how the energy is clustered (ie. what  $E_T$  one calculates per cluster) in addition to the positioning of the cluster.

The sample we used was the QCD 20 GeV jet sample (1684 events) with no min-bias overlay. We did the matching starting from sectors having tracks and matching to EM clusters. For the match, we require that the sector center be within half the EM phi granularity of the EM cluster phi centroid. We get rates given in Table 19.

Table 19. Comparison of the calorimeter-track matching rates for 0.1 and  $0.2 \Delta \phi$  granularities vs. the track  $p_T$  and EM cluster threshold. The second column gives the number of sectors with tracks above the given threshold, and the next four columns give the ratio of the number of sectors matching EM clusters of the given  $E_T$  threshold for 0.1/0.2 granularities respectively.

track Pt	sectors w/trks	EM>1GeV	EM>2GeV	EM>5GeV	EM>10GeV
>1.5GeV	7171	896/2101	740/1945	241/1139	52/379
>3GeV	3085	531/1201	451/1152	151/736	31/275
>5GeV	1107	240/493	210/483	89/326	21/136
>10GeV	217	60/98	52/97	39/77	10div42

The main feature of these results is that there seems to be a factor of 1.5 to 3 gain in rejection by going to 0.1 granularity in EM  $\phi$ . This is likely just the geometrical gain from avoiding tracks randomly distributed in the jet containing the EM cluster. Surprisingly, larger relative rejections seem to be attained when we consider matching low Pt tracks with high  $E_T$  towers. These may be situations where the EM cluster is dominated by photon deposition from a leading pi-zero, which may be anti-correlated with the low Pt tracks in the jet from charged hadrons. This requires further study.

### 4.8.6 <u>Implementation</u>

The track matching hardware could be accommodated in the proposed designs of the L1 calorimeter trigger system (see the hardware implementation section later on in the document). However, there are significant cost, design and manpower issues that are raised if finer (x2) EM trigger towers are implemented. The BLS trigger sum driver hybrid would be replaced with a new hybrid capable of driving (single-ended) the cable to the L1 calorimeter trigger system through the existing cable plant. The factor of two increase in the number of EM signals would essentially double the electronics count for those channels and add complexity to the system. The full ramifications of this finer segmentation are not yet fully understood and require further study.

#### 4.8.7 Conclusions

The track matching studies show that there are considerable gains to be made by implementing this algorithm. Depending on the precise type of track matching (sectors vs quadrants) there are gains from two to four in the rejection of many backgrounds we will be triggering on at L1, relative to not carrying out

any track-calorimeter. It is not clear at the moment what the implementation tradeoffs are between these two scenarios – they require further study. The effect of multiple interactions on this result does not appear to be large.

There are also significant benefits from the point of view of the tracker, where track matching is used to verify track triggers rather than calorimeter triggers.

The further improvements contemplated by further segmenting the EM trigger towers in 0.1 in phi might provide a potential factor of three further improvement. Also, if one tightens the track Pt requirement beyond 1.5GeV, then the rejection improves substantially again.

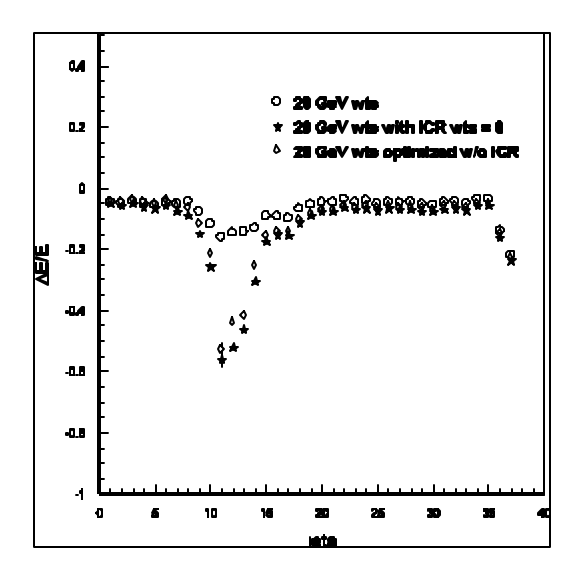
Our conclusion is to support the implementation of a track matching algorithm, although the precise details of the algorithm will require further study, and the question of the EM trigger tower segmentation should be deferred until more studies are completed.

# 4.9 Improving Missing E<sub>T</sub> Triggering using ICD Energy at Level 1

# 4.9.1 Concept & physics implications

Global tower  $E_T$  sums such as missing  $E_T$  or scalar  $E_T$ , while very useful, suffer from several significant problems at the L1 trigger. One significant issue is that the ICR sampling layers are not available in the calculation at Level 1. h addition, the imprecision of the tower  $E_T$ 's gets compounded for global sums, resulting in significantly degraded effectiveness. This is particularly true in a multiple interaction environment. There are two main possible solutions to these problems. First we can take advantage of work done for Run2a to make the ICR layers available at Level 2 and add these towers back into the global sums at Level 1 in Run2b. Second, we can attempt to come up with a scheme which discriminates towers which are from multiple interactions and avoid adding them into the sum.

The region around  $0.8 < |\eta| < 1.5$  encompasses the transition from showers contained within the CC and showers contained within the EC. There is a gap in EM coverage and a major thinning of FH coverage in this area. Since these are the layers which comprise standard trigger towers, there is a major degradation in Level 1 calorimeter response and resolution in this region. This is exacerbated by the presence of significant dead material in the solenoid in Run2. Simulations of single pions and jets in this region indicate that the energy scale in this region goes as low as 40% of the CC/EC scale (as shown in Figure 36), and the resolution is as bad as 6 times worse than in the CC or EC (as shown in Figure 37). These results are very consistent with findings from Run1 Level 1 missing  $E_T$  analyses (see Figure 38). One of the major results of this deficiency is that the efficiency and rejection of a Level 1 missing  $E_T$  selection are noticeably degraded. These simulations also indicate that adding ICD and MG cells into trigger towers can improve the scale by a factor of 2, while optimizing the resolution by a factor of 3.



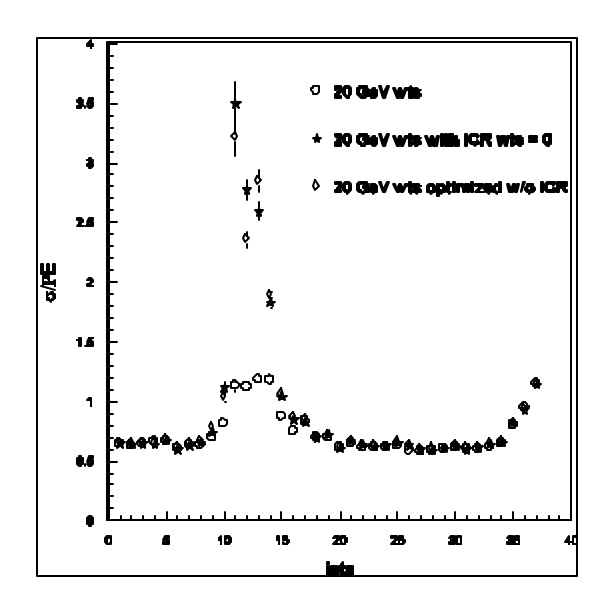


Figure 35. The relative calorimeter energy response in the ICR region for incident 20 GeV pions as a function of  $\eta x10$ . The stars are the response if the ICR weights are set to zero, the open diamonds are the response if the ICR energies are ignored and the remaining calorimeter weights are re-optimized, and the open circles are the response when the ICR region is included and the weights are optimized.

Figure 36. The calorimeter energy resolution in the ICR region for incident 20 GeV pions as a function of ηx10. The stars are the response if the ICR weights are set to zero, the open diamonds are the response if the ICR energies are ignored and the remaining calorimeter weights are re-optimized, and the open circles are the response when the ICR region is included and the weights are optimized.

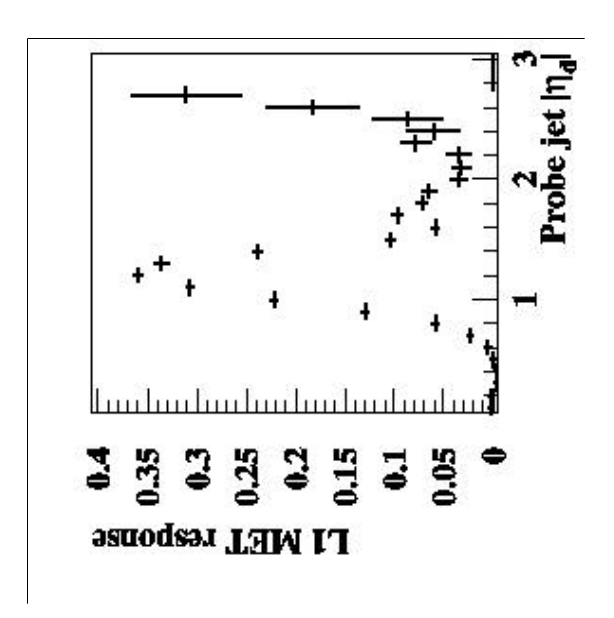


Figure 37. The L1 missing  $E_T$  response as a function of  $\eta$  for 85 GeV jets using the Run I D0 detector simulation.

### 4.9.2 Simulation

In principle, it is straightforward to estimate the effect of the ICD and MG to the missing  $E_T$  calculation. Unfortunately, the Run2 software currently suffers from three major problems in producing a trustworthy study of this matter. The sampling weights valid for the trigger towers, as opposed to the precision readout, are not applied to cell-level energies when trigger towers are constructed for the trigger simulator. Also, there has been no opportunity yet to determine whether the detector simulation accurately reproduces the behavior in the ICR, and this is especially important for the ICD which was substantially more difficult to calibrate than the LAr gaps in Run1. Lastly, the mapping of calorimeter cells has not been instituted into our standard Monte-Carlo sample generation. The last of these problems is easily solved, but the first two present a larger problem.

Until such time as we have resolved these problems, we will estimate the expected improvement based on other studies.

### 4.9.3 Rates and rejection improvements from ICR energies

To estimate the effect of adding the ICR detectors into the missing  $E_T$ , we consider the fact that in the region of  $1.0 < |\eta| < 1.4$ , the sampling weight simulations indicate approximately half of the energy will be deposited in the EM+FH, and the other half in the ICD+MG. As a crude estimate of the magnitude of the effect of adding the ICR layers, we will merely consider the missing  $E_T$  measurement with and without the EM+FH layers in this region and assume the ICR improvement will be similar. Although the sample used for this calculation is a QCD sample with jet Pt>20 GeV and 0 min-bias events overlayed, for historical reasons it is a different sample than that mentioned in the

rest of this document with the same specifications. The missing  $E_T$  mean and RMS in this sample behave as follows:

if remove all ICR TTs:  $\mu$ /rms = 6.7 GeV / 4.8 GeV

if only use EM+FH TTs:  $\mu/\text{rms} = 5.5 \text{ GeV} / 3.9 \text{ GeV}$ 

The number of events passing various Level 1 missing  $E_T$  cuts in this sample are shown in Table 20.

Table 20. Events passing L1 missing E<sub>T</sub> cuts when the ICR energy is included and when it is removed from the trigger towers.

L1 ME <sub>⊤</sub>	Without ICR	With ICR
> 5GeV	948	766
> 10 GeV	337	185
>15 GeV	95	40
> 20 GeV	37	11
> 25 GeV	9	4

Thus, the region is important to the missing  $E_T$  calculation and the rates of passing 15 or 20 GeV selection can change by factors of around 3. A proper treatment of the gains from adding in the ICD and MG, however, will have to await a satisfactory treatment of the relative weights of various layers.

# 4.9.4 Improving Missing $E_T$ for Multiple interaction Events

Our experience in Run1 indicated the Level 1 missing  $E_T$  to be very sensitive to the number of multiple interactions. This results from several factors, including the fact that the fundamental trigger tower fractional energy resolution is poor, especially for very low  $E_T$  towers, and the numbers of these towers increases substantially with the number of multiple interactions. As a result, we have explored a few ways in which we might improve the Missing  $E_T$  resolution to reduce this problem in Run2b.

First, we varied the low threshold on the  $E_T$  of towers going into the global sum. In Run1, this threshold was 0.5 GeV and was not studied in detail in the light of multiple interactions. Again, we have used the QCD  $p_T>2$  GeV and  $p_T>20$  GeV samples with 0mb, and 5mb and 10mb, respectively, for high luminosity overlays. We have used the ttbar sample with 2.5 mb overlays for signal. If we calculate the missing  $E_T$  mean and RMS in these samples for various  $E_T$  thresholds, we find the results shown in Table 21.

Table 21. Change in the means and rms for the missing  $E_{\Gamma}$  for background (QCD) and signal (ttbar) samples as a function of the trigger tower (TT) threshold. A selection of 1.5 GeV on trigger towers removes most of the multiple

interaction variation for the QCD samples, while having little effect on the signal top sample.

ME <sub>T</sub> calc	2GeV QCD (μ/rms) in GeV	20 GeV QCD 0mb (μ/rms) in GeV	2GeV 10 mb QCD (μ/rms) in GeV	20 GeV QCD 5mb µ/rms) in GeV	ttbar (μ/rms) in GeV
TT>0.5GeV	1.0/1.0	5.1/3.8	3.1/2.2	6.5/4.2	35.9/25.4
TT>1GeV	0.6/0.9	5.2/3.9	2.3/1.9	5.8/4.0	35.4/24.7
TT>1.5GeV	0.3/0.7	5.3/4.1	1.6/1.9	5.6/4.0	35.0/24.1
TT>2GeV	0.1/0.6	5.2/4.2	1.0/1.7	5.4/4.2	34.6/23.6

The error on the mean and RMS for the QCD samples is approximately 0.1 GeV. The cut of 2GeV reduces the mean of the QCD sample noticeably. If we consider the 20 GeV sample, the trigger tower cut of 1.5 GeV provides a 20% to 30% lower pass rate for moderate missing  $E_T$  selections. Although scalar  $E_T$  is generally considered a poor variable at Level 1 because of its sensitivity to multiple interactions, we have studied its mean and rms (see Table 22) for the same thresholds to see what is happening:

Table 22. Change in the means and rms for the E<sub>T</sub> scalar sum for background (QCD) and signal (ttbar) samples as a function of the trigger tower (TT) threshold.

Sum E <sub>T</sub> calc	2GeV QCD, 0.7 mb (μ/rms) in GeV	QCD 0mb (μ/rms) in GeV	2GeV QCD, 0.7 mb (μ/rms) in GeV	QCD 5mb μ/rms) in GeV	ttbar ( <u>µ/rms)</u> in GeV
TT>0.5GeV	2.9/3.3	23.5/13.0	21.2/18.1	57.7/39.3	179.7/68.8
TT>1GeV	0.8/1.5	17.9/11.9	6.5/7.1	26.6/15.8	161.1/66.4
TT>1.5GeV	0.3/1.1	14.7/11.4	2.8/4.2	18.0/12.5	151/64.9
TT>2GeV	0.2/0.8	12.5/11.1	1.5/3.1	14.2/11.6	143.6/63.8

Comparison of the two QCD samples indicates that low thresholds let in an enormous amount of energy which has nothing to do with the hard scatter interaction.

Because the typical low Pt QCD event E<sub>T</sub> is distributed flat in eta, we might not expect a degradation in global sum behavior from including forward trigger towers in the calculation of these quantities. In fact, when looking in simulated

events even with large numbers of multiple interactions, one finds very little transverse energy in this region. However, our experience in Run1 indicated strongly that use of forward towers (ie. those around  $|\eta|$  ~3 or more) substantially degraded the missing  $E_T$  behavior. This was especially true in a multiple interaction environment. As a result, we suspect strongly that there is a benefit from being able to easily select what the range is for the calculation, or perhaps include the  $\eta$  parameter into a weighting scheme with the trigger tower  $E_T$ . This requires further study only possible once data is available.

Another concern for the missing  $E_T$  measurement involves the truncation of trigger tower  $E_T$ 's into 0.5 GeV bins. Since one to two hundred towers are typically added into the Missing  $E_T$ , this resolution loss can start to be noticeable. Taking the QCD Pt>20 sample with mb=0 and 1648 events, we can use the simulator described above in the ICR discussion and toggle truncation on and off. The results are shown in Table 23.

Table 23. Comparison of the effect of TT truncation on the MET. The table lists the number of events (out of a sample of 1648, QCD with Pt> 20GeV and no minimum bias overlaid events) that pass the listed Missing E<sub>T</sub> thresholds.

Missing E <sub>T</sub> >	no truncation	no truncation, TT>0.5GeV	with truncation
5 GeV	947	868	766
10 GeV	309	261	185
15 GeV	76	51	40
20 GeV	22	17	11
25 GeV	7	5	4

The first column indicates truncation turned off and no threshold applied to trigger towers. The second column also has no truncation and zeros out all towers with  $E_T$  <0.5. The third column employs the normal 0.5 GeV truncation. Since truncation lowers tower  $E_T$ 's only to the next lowest 0.5 GeV increment, it effectively deweights all of the poorly measured  $E_T$  in low  $E_T$  towers. In fact, if we consider the QCD Pt>20 GeV sample with 5mb already discussed, the missing  $E_T$  mean and RMS are mildly improved over the straight 1.5GeV threshold by a simple weighting scheme. If we choose weights of 5%, 25%, and 75% for  $E_T$  = 0.5, 1.0, and 1.5 GeV, respectively, we find the results shown in Table 24.

Table 24. Comparison of simple TT threshold vs. weighting scheme for 20GeV QCD jet sample.

if TT Et>1.5 GeV:	$\mu/\text{rms} = 5.41 \text{ GeV} / 4.20 \text{ GeV}$
if weight TT:	$\mu/\text{rms} = 5.41 \text{ GeV} / 3.96 \text{ GeV}$

If the capability exists in an FPGA to enforce a weighting scheme, then one might devise a scheme which does better than this.

Because the trigger tower threshold seems to be the simplest solution that shows progress, and the weighting also seems to help, one might ask whether rejecting low  $\mathsf{E}_\mathsf{T}$  towers unless they are near significant neighbors might help. Looking again in the 5mb QCD sample at missing  $\mathsf{E}_\mathsf{T}$  means and sigmas, we find the results shown in Table 25. These results point to a significant degradation in missing the  $\mathsf{E}_\mathsf{T}$  mean and resolution.

Table 25. Comparison of effect of rejection low ET towers unless they are near trigger towers (NN) with significant energy deposits.

no cut:	$\mu/\text{rms} = 6.45 \text{ GeV} / 4.17 \text{ GeV}$
if NN E <sub>T</sub> > 0.5 GeV:	$\mu/\text{rms} = 6.45 \text{ GeV} / 4.37 \text{ GeV}$
if NN E <sub>T</sub> > 1.5 GeV:	$\mu/\text{rms} = 6.56 \text{ GeV} / 4.37 \text{ GeV}$
if NN $E_T > 3.0$ GeV:	$\mu/\text{rms} = 6.72 \text{ GeV} / 4.86 \text{ GeV}$
if NN E <sub>T</sub> > 10 GeV:	$\mu/\text{rms} = 5.62 \text{ GeV} / 4.57 \text{ GeV}$
if NN E <sub>T</sub> > 1k GeV:	μ/rms = 5.41 GeV / 4.20 GeV

## 4.9.5 Conclusions

In this section, we have explored several different ways to improve the calorimeter missing  $E_T$  measurement at Level 1. Studies leading to the optimization of the Run2a trigger have indicated a large improvement in the scale and resolution of jets in this region if the ICD and MG are used. Although our current simulation samples do not have a proper treatment of this region, a crude estimate indicates that this amount of energy should have a noticeable improvement on the missing  $E_T$  resolution.

Several attempts were also made to improve the behavior of missing  $E_T$  in a multiple interaction environment. The most promising appears to be a simple tightening of the  $E_T$  threshold on a trigger tower to around 1.5 GeV which would reduce the background by around 20% in our QCD sample. The actual degradation in the real data may be larger than we see here, however, and the corresponding gain may also increase. We will be in a better position to evaluate this when we have reliable data at various luminosities. There is some evidence that a weighting scheme would provide further benefits.

# 4.10 Finer EM Tower Segmentation for electrons

## 4.10.1 Concept & physics implications

The gains from larger trigger towers and the sliding window algorithm is apparent for jets. Given the much smaller extent of electromagnetic showers we

were led to explore the possible gains from smaller EM towers with or without a sliding window algorithm.

### 4.10.2 <u>Simulation</u>

Monte Carlo single electrons have been used to compare the performances of the various options:

- Fixed trigger towers of 0.2 x 0.2 (the current system)
- Fixed trigger towers of 0.2 x 0.1
- Trigger towers of size 0.2 x 0.2 which slide in either the  $\eta$  or  $\varphi$  direction by steps of 0.1.

The direction of the generated electron is extrapolated to the calorimeter surface and trigger regions are looked for in the neighborhood of the intersection point.

Figure 38 shows the transverse energy seen in the trigger region for cases 2) and 3), normalized to that seen by the current trigger. It can be sen that fixed trigger towers of size 0.2 x 0.1 will see ~ 5% less  $E_T$  than the current TTs. A slightly larger energy is deposited in windows which are sliding in the  $\eta$  rather than in the  $\varphi$  direction. This is due to the fact that when the Zvertex is not zero, the calorimeter geometry is not projective in  $\eta$  (while it is always projective in  $\varphi$ ). Figure 39 shows that indeed, when electrons are emitted at Zvertex  $\approx$  0, overlaps in  $\eta$  and overlaps in  $\varphi$  yield similar energy deposits in the trigger regions.

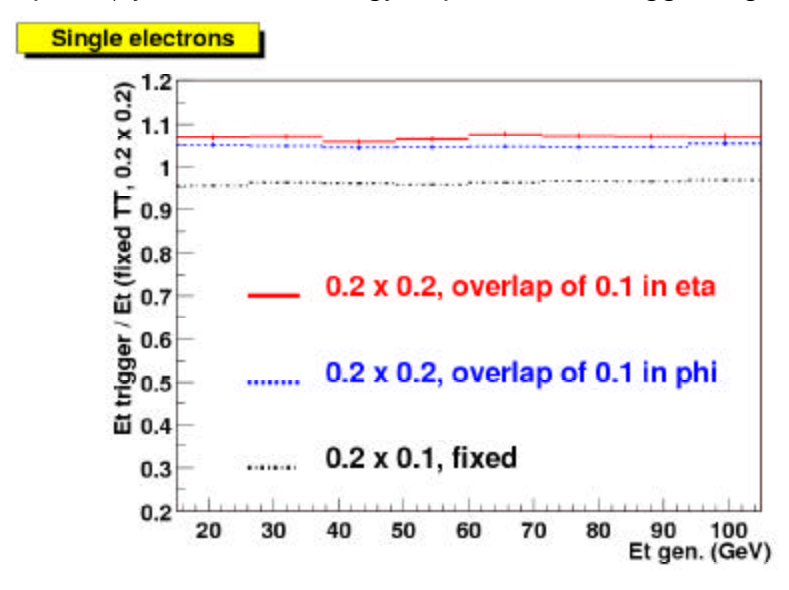


Figure 38. Ratio of the  $E_T$  measured in various possible trigger regions to the  $E_T$  seen by the trigger when using fixed 0.2 x 0.2 TTs.

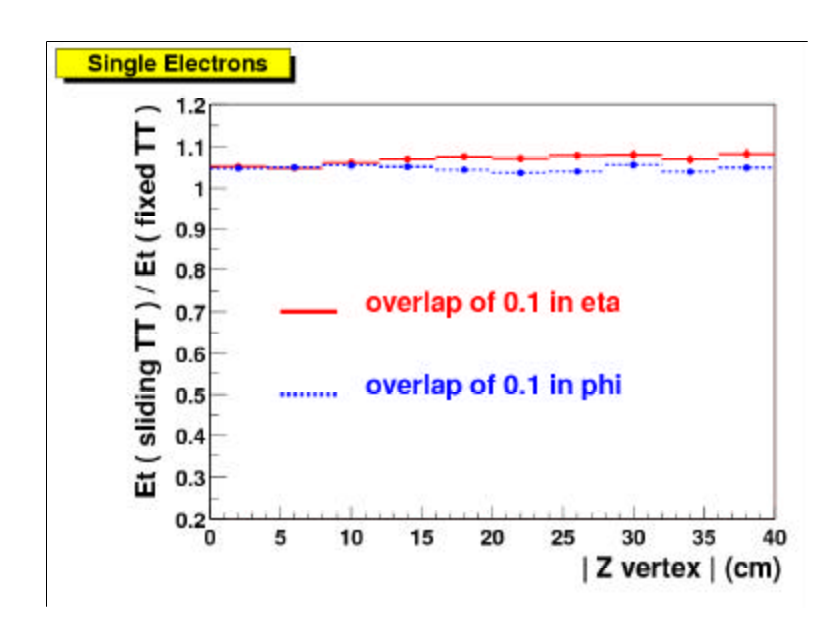


Figure 39. Ratio of the trigger Et seen by using sliding windows of 0.1 in  $\eta$  or in  $\varphi$  to the E<sub>T</sub> seen in the current trigger towers, as a function of the Zvertex.

# 4.10.3 Efficiency

The efficiencies on single electron events are summarized in Table 26.

Table 26. Efficiencies for single electron events.

E <sub>T</sub> ,e (GeV)	Trigger threshold (GeV)	0.2 x 0.2 (fixed)	0.2 x 0.2 sliding in η	0.2 x 0.2 sliding in $\phi$	0.1 x 0.2	0.2 x 0.1
10	5	91.1%	94.5%	94.5%	86.1%	89.0%
10	7	69.6%	78.0%	76.4%	57.4%	59.1%
20	10	90.5%	93.4%	93.9%	86.9%	88.6%

The single electron efficiency vs. the inclusive QCD rate has also been studied. In these studies three of the above algorithms have been compared using a trigger requirement that demanded at least one EM TT above a given threshold (with no hadronic fraction veto). The rate is calculated assuming a luminosity of  $2x10^{32}$  cm<sup>-2</sup> s<sup>-1</sup> with an average of 2.5 overlaid minimum bias events. The efficiency for the central region,  $|\eta|$ <1.2, is shown in

Figure 40. The three algorithms perform similarly at the smaller thresholds, but the 0.2x0.1 fixed window algorithm is somewhat more efficient at large trigger thresholds.

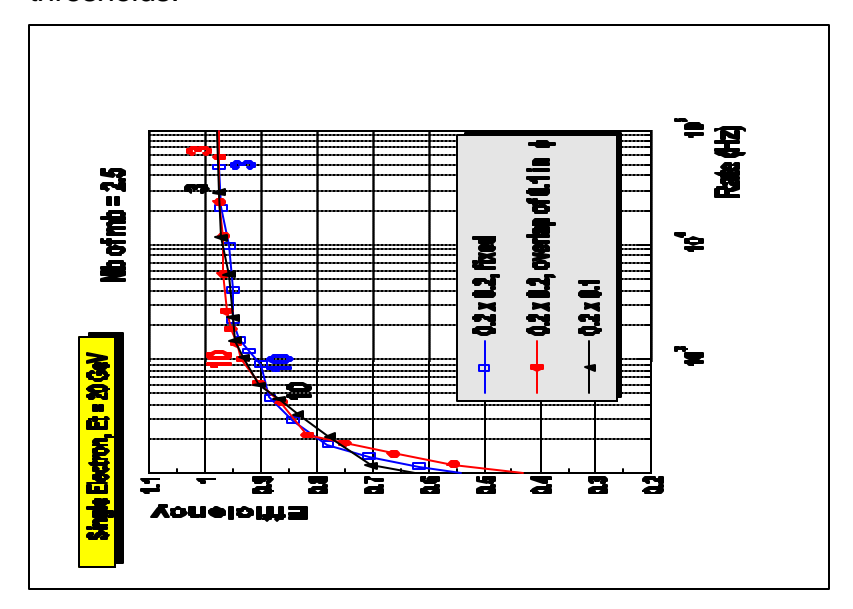


Figure 40. The single electron efficiency for  $|\eta|<1.2$  vs. the QCD inclusive rate for a luminosity of  $2x10^{32}$  cm<sup>-2</sup> s<sup>-1</sup> for three different algorithms. The algorithms are 0.2x0.2 fixed window (open squares), 0.2x0.2 sliding window with a 0.1 overlap (solid circles), and a fixed window of 0.2x0.1 (solid triangles). The points represent different trigger thresholds (in steps of 1 GeV) with 3 and 10 GeV indicated for reference.

## 4.10.4 Implementation

The implementation of finer EM segmentation has considerable impact on the complexity, size and cost of the L1 calorimeter trigger. The required changes start with the BLS trigger sum driver hybrid and propagate through essentially a doubling of numbers of boards in the L1 calorimeter trigger. The full implications of implementing this finer granularity has not yet been fully studied.

### 4.10.5 Conclusions

We do not yet have a complete understanding of the gains that a finer EM segmentation would afford. Since the cost (in complexity, funds and manpower) of implementing this option is quite high, we conclude that more must studies be done before making a final decision on the granularity. In addition, these studies must be completed soon because of the large impact on the system design.

# 4.11 Topological Considerations

# 4.11.1 Concept & physics implications (acoplanar jets)

The search for Higgs boson is the central element of the Run 2b physics program. The Run II Higgs workshop report<sup>6</sup> concluded that the channel p pbar - > HZ -> b bbar  $\nu$  vbar was critical. This final state poses a difficult topology, two relatively soft jets ( $p_T < M_{h/2}$ ) with modest missing  $E_T$ . For a Runl style di-jet plus ETmiss trigger, the nominal calorimeter trigger tower and missing  $E_T$  thresholds are such that the efficiency for the b bbar  $\nu$  vbar channel is compromised. The trigger efficiency is driven by the allowable Level 1 rate. While b-tagging can be used at Level 2 to control the rate, it is important to note that b tagging will not be possible at Level 1. Thus, it is clear that this channel relies on alternative triggering techniques at Level 1.

# 4.11.2 Efficiency

To efficiently trigger on the HZ channel one can exploit the unique topology: the higgs is recoiling off of a massive particle decaying invisibly, thereby leading to an acoplanar jet topology. From Monte Carlo based studies, it has been demonstrated that the L1CTT can be used to identify acoplanar topologies using the fiber tracker. The algorithm is based on identifying the 4.5 degree wide sector having the highest track p<sub>T</sub> sum within the two 45 degree wide octants having the highest track p<sub>T</sub> sum. In Figure 41, the opening angle between the leading partons is shown, the binning reflects the CFT azimuthal segmentation. The red histogram represents the true opening angle and the blue is the corresponding angle reconstructed from charged tracks in the CFT using the above algorithm. Note the QCD background is predominately back-to-back (i.e. the most probable opening angle is 40 sectors or 180 degrees) whereas the Higgs signal has a substantial acoplanar component. Figure 42 shows the correlation between delta phi and the ETmiss of the event for signal and representative QCD backgrounds. The figures demonstrate that combining an acoplanar toplogy cut (Nsector < 35) with a looser missing ET requirement can maintain good signal efficiency while still suppressing most of the QCD background.

6 Report of the Higgs Working Group of the Tevetr

<sup>&</sup>lt;sup>6</sup> Report of the Higgs Working Group of the Tevatron Run 2 SUSY/Higgs Workshop, M. Carena et al, hep-ph/0010338

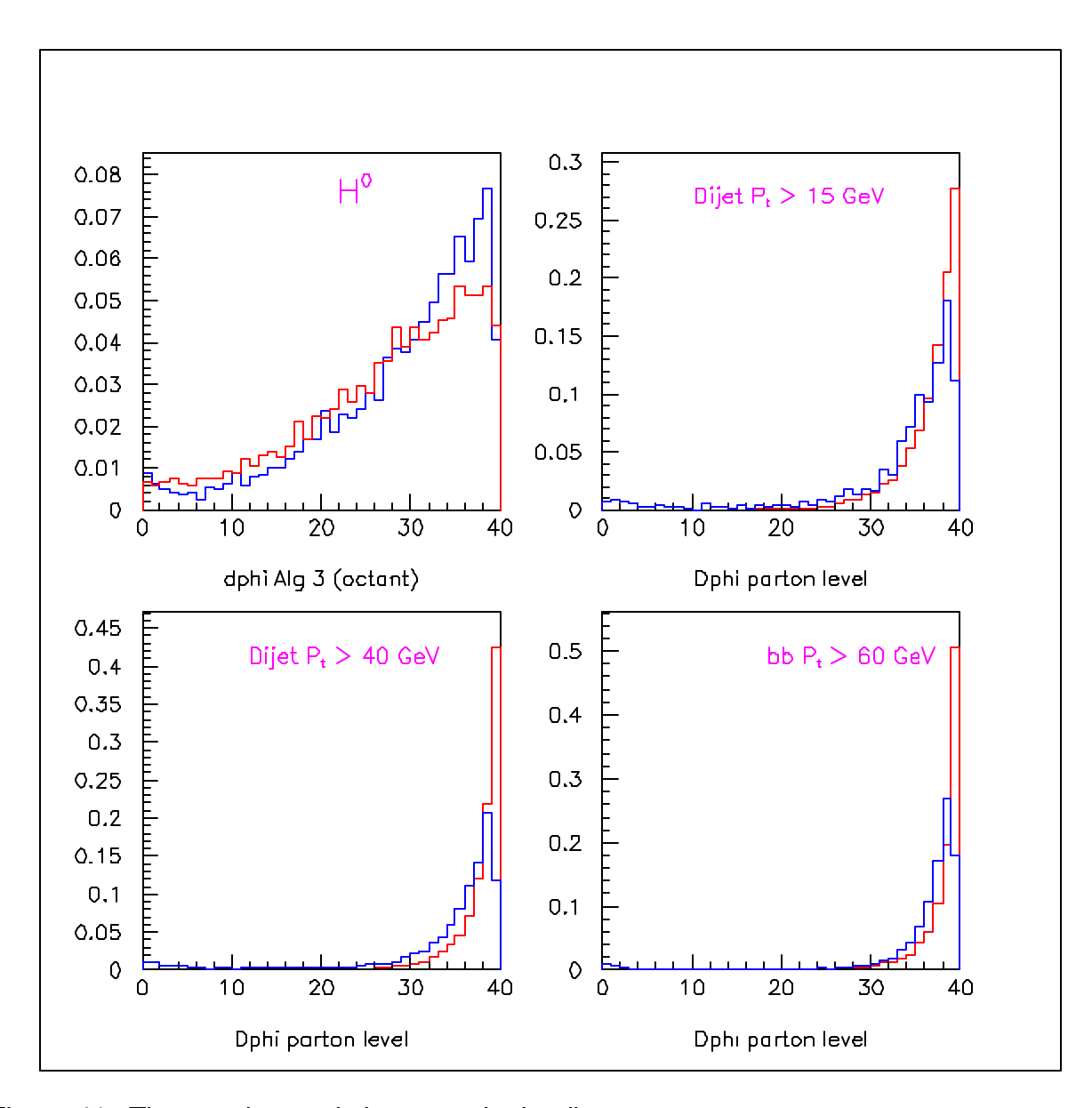


Figure 41. The opening angle between the leading partons.

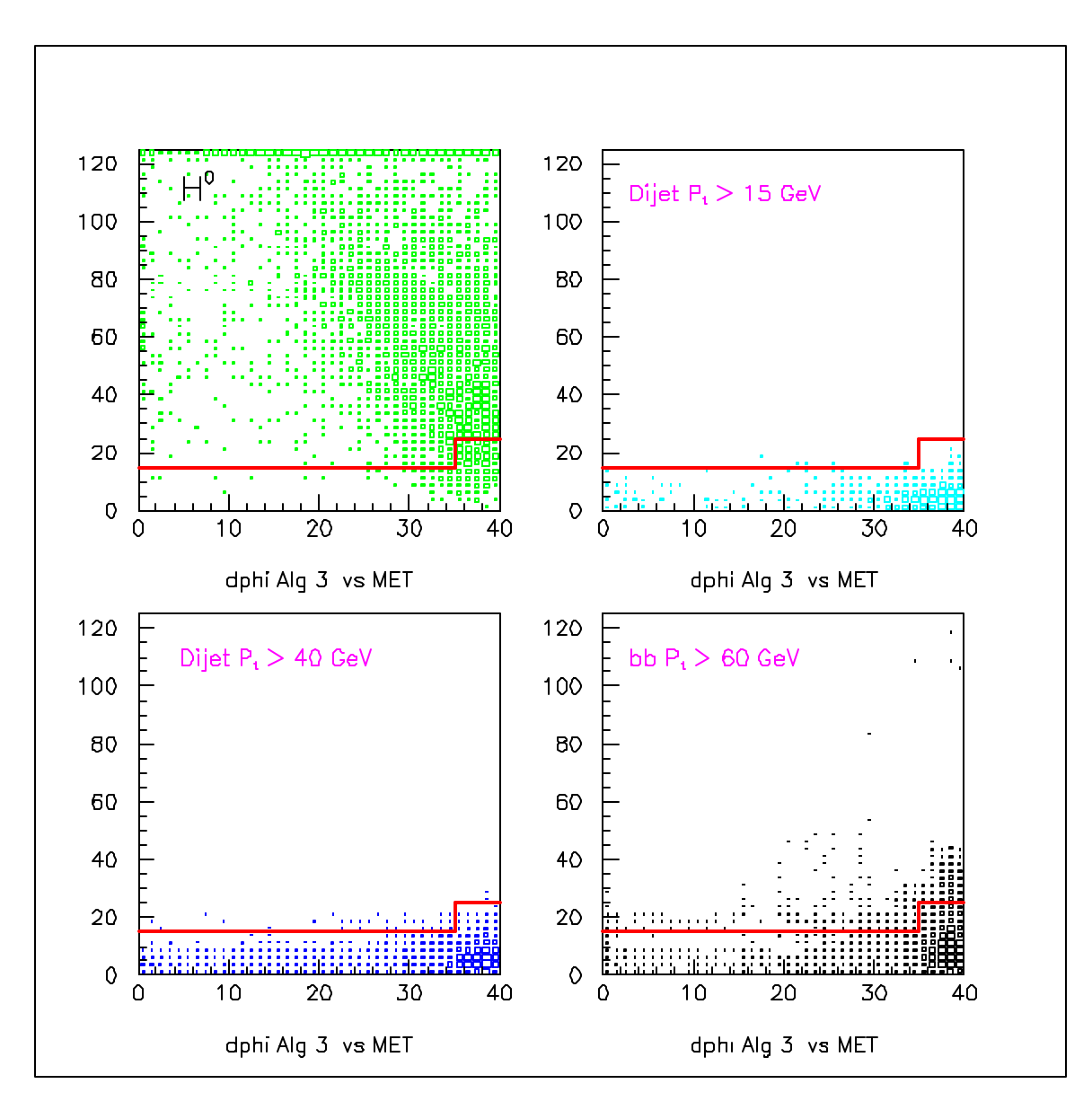


Figure 42. The correlation between delta phi and the ETmiss of the event for signal and representative QCD backgrounds

# 4.11.3 Rates and rejection improvements

The use of the CFT phi correlations becomes compromised at high instantaneous luminosity. as shown in Figure 43. Only for relatively high  $p_T$  jets does the correlation remain. At high luminosity one has to rely on the calorimeter to confirm the CFT jets. Modest trigger thresholds are able to reduce the rate from low  $p_T$  scatters.

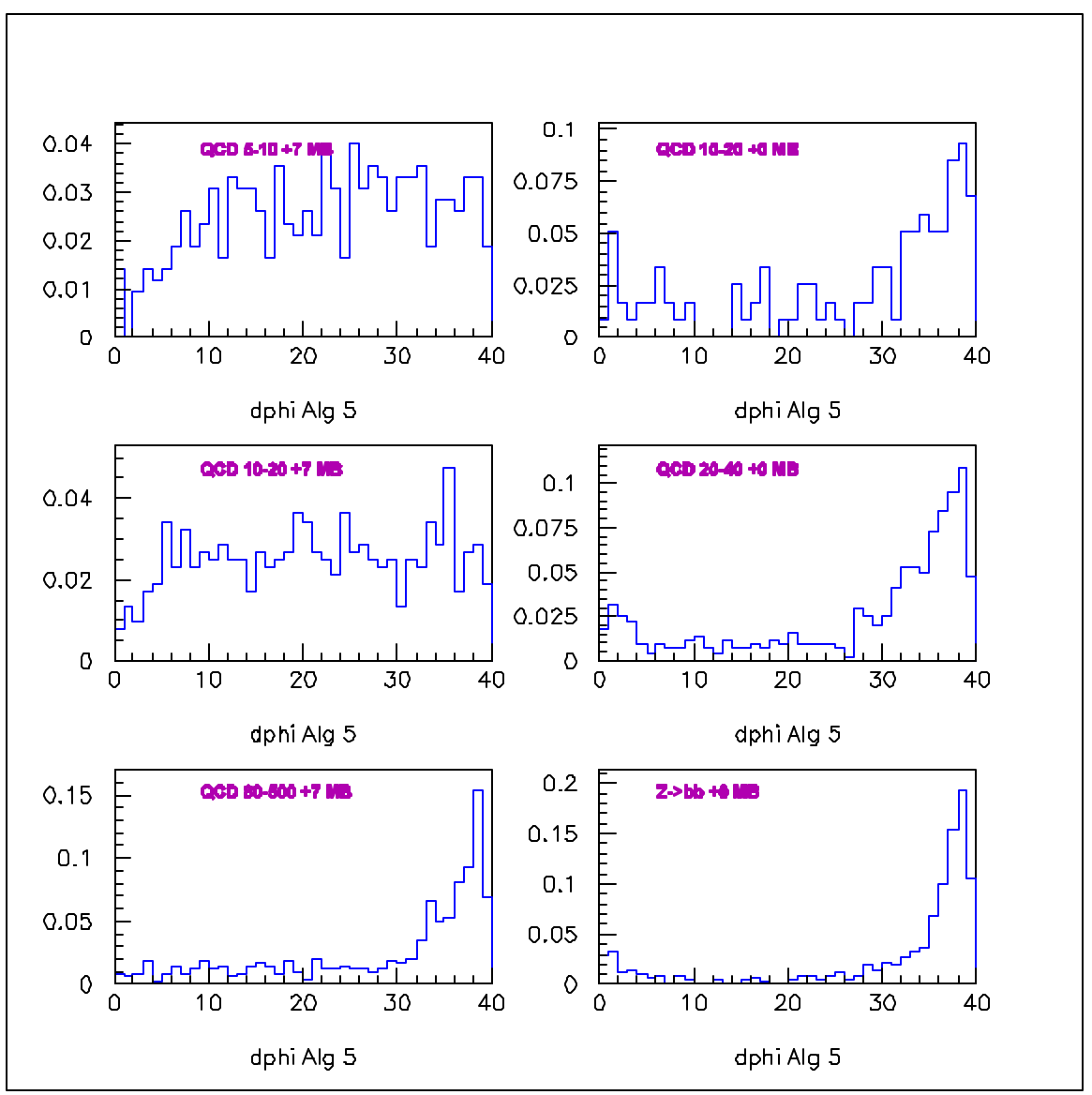


Figure 43. Correlation of  $\Delta \phi$  in high luminosity conditions (left hand plots with 7 minimum bias events) and low luminosity (right hand plots with zero additional minimum bias events).

With an improved Level 1 calorimeter trigger that allows correlating CFT and calorimeter based jets these backgrounds can be further suppressed.

# 4.11.4 <u>Implementation</u>

The implementation of topological cuts and shape cuts are in principle relatively easy to include in the trigger given that the logic is essentially implemented in FPGAs. There is little incremental cost to implementing these types of tools in the trigger.

### 4.11.5 Conclusions

Given the essentially zero cost impact of including these types of trigger tools in a L1 calorimeter trigger, we support the implementation of these tools in the new trigger system.

# 4.12 L1 Calorimeter Trigger Implementation

The physics imperatives that drive the need to build a new L1 calorimeter trigger raise a number of implementation issues that will need to be resolved before construction can begin. In this section we discuss the issues that have been raised to date regarding implementation choices that need to be made. Among the important considerations and constraints are ways to minimize the disturbance to the running system as the new system is integrated into the experiment and commissioned.

#### 4.12.1 Constraints

Because the L1 calorimeter system needs to be integrated into the existing D0 DAQ system it needs to obey the following constraints.

# 4.12.1.1 Existing interfaces

The interfaces of the new system to the existing hardware should be compatible. In particular the new system must interface to the input pickoff signals, the L1 framework, the L2 and L3 data, the clock, and the timing and control systems. Depending on the physics requirements, some of the interfaces may be changed because the existing systems will be modified. An example of this is the possibility that the present differential trigger sum driver signals from the calorimeter will be further subdivided to provide finer granularity EM towers. The change would mean that the present differential coax signals would be used as single ended coax cables (thereby doubling the granularity from 0.2x0.2 to 0.1x0.2 in  $\phi \times \eta$ )

# 4.12.1.2 L1 Latency

The L1 latency is 4.2 µsec. The new system should be compatible with this value. So, the maximum time remaining for complete signal processing which includes digitization, filtering and the processing of the cluster algorithms is less than 2.7 µsec after accounting for all the transit times and front end processing. While we do not believe that this should be a concern using modern FADCs and FPGAs, the execution of the cluster algorithms should be optimized in order to be as efficient as possible.

# 4.12.1.3 Adiabatic integration

The installation and integration of the new system should be designed and built in such a way as to minimize the effect on the data taking. For example, in the absence of a long shut down between Run 2a and b, we are considering the use of single ended signals from the trigger pickoff as a means to split off the signals for parasitic running – the full implications of such a choice are not yet understood, but are under study. In addition, a testing phase of a part of the trigger with real data would be a great help to debug and validate the algorithms and associated monitoring.

# 4.12.2 <u>L1 Calorimeter trigger hardware conceptual design</u>

A block diagram of the new L1 calorimeter trigger system is shown in Figure 44. The main change will consist to remove the present ADC and logic cards hosted in 13 racks and replace them by a 2 to 3 racks of new electronics that will perform the Analog to Digital Conversion, (ADC) the digital filtering (FIR) and the cluster algorithm processing (TAP) for jets and electrons. An output to track matching logic is also foreseen. The functionality of the main functional blocks are discussed in the following sections.

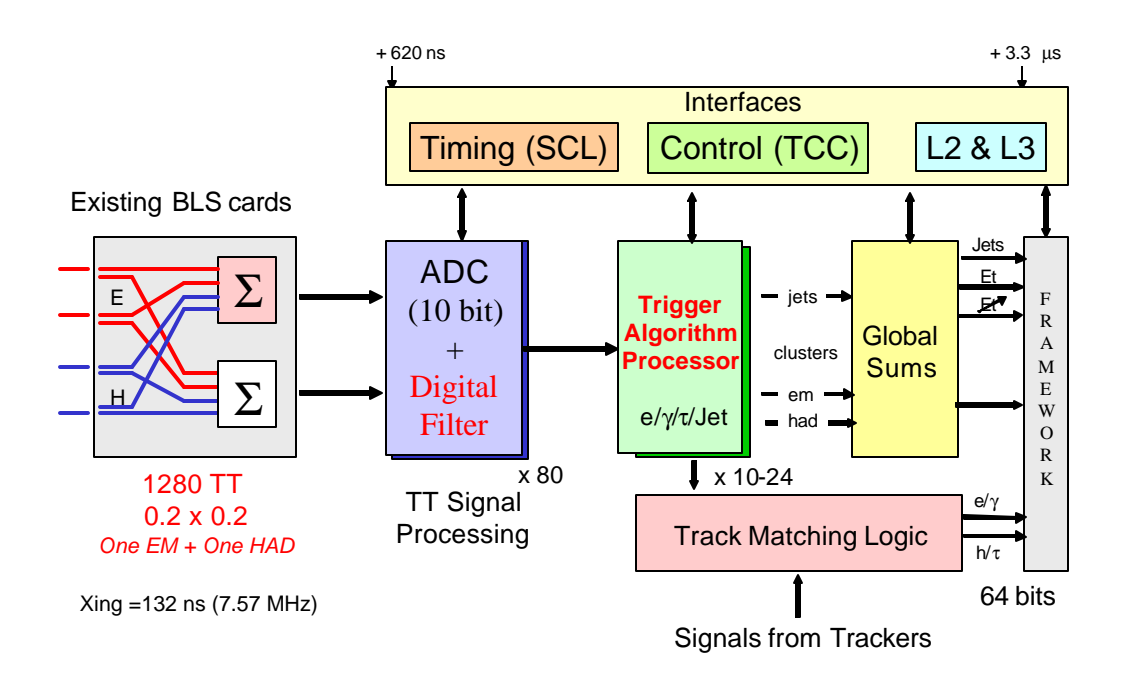


Figure 44. Block diagram of L1 calorimeter trigger.

## 4.12.3 ADC/TAP Split

In the previous sections we have discussed the various functions that are needed for the L1 calorimeter trigger. One natural split in the system could occur between the ADC section that handles analog signals and a TAP (Trigger Algorithm Processor) section that is a purely digital processor. These two

sections would then be linked by LVDS connections. The location of the digital filter leaves us with two options that we consider below.

# 4.12.3.1 Option 1: "Dumb" ADC

In this option, the ADC section contains only the analog to digital converter, and no digital filter. The reason to consider this is that the TAP should have enough processing power to perform both the digital filtering and the physics algorithms. The ADC part would produce output samples with 10 bits accuracy. The expected advantages are that in this case the ADC would not need slow controls. Thus it is viewed as inexpensive, simple and very easy (that is to say relatively fast) to implement. However the disadvantage is that this implementation would likely be incompatible with a sampling rate that is faster than the beam crossing rate, because of output bandwidth required to transport all the signals from the ADC to the TAP.

# 4.12.3.2 Option 2: Filter in the ADC

For this option we place the digital filtering on the in the ADC section. The advantages of this option are:

- The output of the ADC can be limited to 8 bits words. Thereby reducing the link bandwidth to the TAP by 20%.
- There are several towers (at the boundary between central and end caps) that need special handling. While this special treatment is required regardless of the design, it would allow at least the TAP card to use a single uniform design (thus reducing design time).
- The data at the output of the ADC is transferred to the Level 2 trigger and the read-out. Applying the filtering in the ADC section would eliminate the need to repeat the filtering calculation in level 2 and in the off-line processing.

It is also possible that given the somewhat complex designs of the digital filter and the trigger algorithm sections, having these functions physically separated would lead to more expeditious development and test, particularly if these two sections were developed and built by different collaborators. Although such a division would impose a further management burden on the project in order to preserve excellent communications between groups.

## 4.12.4 <u>Granularity</u>

The current granularity of the trigger towers is 0.2 x 0.2 in  $\phi \times \eta$ . It is possible with a replacement of the trigger sum driver hybrid in the BLS to provide a granularity of 0.1x0.2 in  $\phi \times \eta$  in while preserving the current cable plant. There are two options to this increase of granularity:

- Increasing the trigger granularity of only the EM towers (mixed sizes)
- Cutting both EM and Hadronic towers (0.1x0.1).

The gains in physics performance have been cited previously; in Table 27 we estimate the relative cost of the three options, normalized to the cost of the 0.2x0.2 option.

Table 27. The relative cost of the various granularity options, normalized to the cost of the 0.2x0.2 option.

	0.2x0.2	Mixed sizes	0.1x0.1
ADC	1	1.5	2
DFE	1	2	4

The mixed solution has a particular difficulty. The 0.2x0.2 Rol consists of two adjacent TTs. This Rol may have two different positions relative to the hadronic towers behind it. The Rol is either exactly on top of one hadronic tower or partially above two hadronic towers. The threshold for the cuts on hadronic fraction or isolation should clearly be different for the two cases. In order to implement those different thresholds we would need additional hardware, and that in turn may end up lessening the effectiveness of the cuts.

# 4.12.5 <u>Overlap</u>

The amount of data produced by the ADC cards is too large to be processed by a single TAP. The volume of data would be about 20 Gbytes/s (for  $0.2 \times 0.2$  and twice that for  $0.1 \times 0.2$ ). Therefore the digital processing must be done by tens of TAP cards, each one processing the data corresponding to a rectangular area of the calorimeter. The number and speed of the LVDS links supplying data to one TAP card determine the number of TAP cards needed. Each DFE card is responsible for the recognition of electrons and jets in its section of the calorimeter.

It is necessary for the data to be shared across neighboring TAP cards in order to implement the algorithms. The amount of sharing depends on the details of the algorithms; the jet algorithm is the most demanding (because jets are larger than electrons). In order to have a reasonable system size, the overlap must be kept to a maximum of two cells in all. This limits the choice of the jet algorithm. The first limitation comes from the need to avoid double counting: the same jet should not be found in two adjacent TAPs. The second requirement is to avoid splitting a single jet at the boundary of two TAPs. Both limitations can be addressed in the subsequent processing stage, but we would to avoid that if possible. That leads to two options for the overlap:

- 2 TT overlap in all directions: This allows for jet algorithms up to 1.0x1.0. It is also needed in the 0.8x0.8 algorithm if one requests separated jets. This symmetrical arrangement makes the cabling easier.
- Alternating 2 TT and 1 TT: This is the minimum for the 0.8x0.8 algorithm.
   This reduces the bandwidth between the ADC and the TAP by 8%.

# 4.12.6 <u>TAP implementation</u>

Since the detailed designs for the L1 calorimeter trigger system do not yet exist, we have explored two possible options for the TAP card implementation. In the first case we consider reusing existing designs of processor cards from other DØ systems. In the second case we imagine a completely new design.

# 4.12.6.1 Option 1: Reuse the existing CTT's DFE design

We have considered the possibility of using the tracking electronics (CTT) digital front end cards (DFE) to perform the trigger processing functions of the TAP. Initial studies on the logical mapping of the DFEs to calorimeter sectors, the physical cabling and the required capacity of the links show that such an option appears viable. More detailed studies are needed before a firm conclusion could be drawn on the ultimate viability of this option, especially concerning the implementation of trigger algorithms in FPGAs. We estimate that this solution would roughly divide by two the design effort required, leading to several months of savings in manpower.

If this solution is adopted, then the digital filter must be implemented on the ADC cards because of:

- The link capacity. Carrying 10 bit samples over DFE links requires 25% more bandwidth than dealing with 8 bit E<sub>T</sub> calibrated samples.
- The available processing power. Incorporating a series of digital filters and the trigger algorithm logic may not fit in the FPGA of DFEs.
- The existing slow controls system. The limitation of bandwidth for slow controls on the DFEs could make the loading and update of filter coefficients unacceptably slow.

Although the potential savings in manpower and the reduction of further complex boards that will need to be maintained are attractive, there are, however, a number of concerns for a DFE based solution. They include:

- The possible unavailability of some components of the DFE, especially connectors on the motherboard. It may not be possible to build a sufficient number of DFEs and spare cards from presently available parts.
- FPGAs on the daughter card of a DFE are mature devices and may not be cost-effective when run 2b starts. Although a new daughter card with a more modern FPGA could be designed, the fact that the serial to parallel conversion for the input links is implemented on the motherboard of a DFE places a tight upper limits on link speeds and imposes a worrisome constraints on FPGA pin counts, printed circuit board design, etc.
- The bandwidth of DFE links which is marginally acceptable, even if these links could be clocked at 61 MHz instead of the current 53 MHz. This limitation could exclude the possibility to run algorithms that

- operate on a 1.0x1.0 window in  $\phi \times \eta$  space, though using 0.8x0.8 windows would probably fit.
- There are no SCL links in the DFE system. The SCL link must be implemented in the ADC sub-system. This will obviously complicate the design of the ADC cards, offsetting the expected savings in manpower on the DFE side.
- Because DFEs do not receive timing information and are purely data driven, the necessary timing signals must be embedded in the dataflow by the ADC cards. This places additional constraints on the ADC cards and consumes a small fraction of the (precious) link bandwidth.
- The logic capacity of the FPGA in the current DFE may not be sufficient. This point has not been studied yet. The FPGA manufacturer does not foresee much (>2) larger devices because it has switched to a new footprint.
- The bandwidth of the slow control is insufficient to keep all the functionalities of the current trigger software.
- The present DFE design is not as robust as one would like because of some rather delicate front panel connectors.

# 4.12.6.2 Option 2: New TAP design

While the possibility of reusing existing designs is attractive, it may not prove possible. Thus we have considered a completely new design for the trigger logic processors (the TAP cards) which allows for superior performance because the compromises imposed by using an already existing design can be avoided (at the cost of design manpower of course). In this study of a new, dedicated TAP module the following guidelines were proposed:

- Use faster LVDS links. This is obtained by feeding the links directly into the FPGA, bypassing the (relatively) slow serializer/deserializer used in the CTT DFE.
- Use SCL data from the back plane for synchronization.
- Use a modern serial bus (such as USB2) for slow control.
- Use 12 input links and 6 output links.
- Use the latest generation FPGA. Use smaller footprint FPGAs because of the reduced number of IO pins obtained by serial IO instead of parallel.
- Place all IO cables at the rear of the module.

Additional compatibility issues could also be addressed in this new design specification, to conserve the current CTT DFE environment:

- Use the same LVDS cables.
- Accept the slow control of the DFE crate as an alternate to the normal one.
- Use software compatible FPGAs.
- Such a design would provide ample improvement margin for possible CTT upgrades.

# 4.12.7 <u>Schedule, resources and cost e</u>stimate

Since a detailed design has not yet been made, the details of the schedule, resources and cost estimate are necessarily sketchy. They will require more work to developed a fully resource loaded schedule. However given the extreme time pressures that are imposed on any Run 2b upgrades, we have made an attempt to broadly address these issues. At present we imagine the construction of the L1 calorimeter trigger as proceeding in three logical:

# Feasibility study - December 2001

This phase already well advanced consists of optimizing the system design, studying the proof of principle and implementation of each element. Bench tests are underway to understand the various parameters, in particular concerning the size of the FPGAs needed for the cluster algorithms. This phase is strongly connected to the physics studies and conclusions that will be used to define the "baseline" specifications (such as granularity and algorithms). It will end with a Technical Design Report that covers a more detailed design along with the requisite organizational details such as the project cost, schedule and resources.

### Prototypes: end of 2002.

This phase will evaluate and optimize each element separately. In a second step, a full slice will be installed in a parasitic mode in the experiment in order to validate the full chain of both hardware and software.

### • Construction, installation: and integration: end of 2003

The fabrication of the series of cards, the installation and integration in the experiment should be done by end of 2003. A possibility to test a part of the new system in a parasitic mode in parallel with the present one could be done in the case where we use single ended trigger sum driver signals on the existing cable plant.

## 4.12.8 Resources

A first evaluation of the available collaboration resources was made at the September 2001 trigger workshop. We believe that there is sufficient manpower to carry out this project in a timely manner. Detailed manpower estimates will be available once the design and responsibilities have been established.

### 4.12.9 Cost estimate

A preliminary cost estimate for the Level 1 calorimeter trigger upgrade is presented in Table 28 below. Manpower is not included. Most of these M&S funds will be needed in FY03 and FY04.

As described in the above sections, much progress has been made in defining the technical approach that the Level 1 calorimeter upgrade is expected to pursue. Nevertheless, there are a number of outstanding issues that remain: among them, for example, is the final trigger tower granularity that is adopted, which introduces a factor of two uncertainty in the number of boards that would have to be fabricated. (The boards for both the ADC/digital filtering system and the digital processing system will be the M&S cost driver for this project.) In an effort to accommodate this broad option in project scope, as well as other sources of uncertainty at this early stage in the design, we include a contingency of 100%. The base cost for most of the items below has been estimated from previous projects in Run 2a that required similar boards, power supplies, backplanes, and other elements.

Table 28. Preliminary cost estimate for the Level 1 calorimeter trigger. A contingency of 100% has been applied. Manpower is not included.

Item	M&S (\$k)	Contingency (%)	Total (\$k)
ADC/digital filter system (crates, boards, etc.)	440	100	880
Digital processing system (crates, boards, etc.)	240	100	480
LVDS cables	25	100	50
VME master processors	25	100	50
TOTAL	\$730k		\$1,460k

# 4.13 L1 Calorimeter Summary & Conclusions

The proposed L1 calorimeter upgrade offers a lot of improvements for the future Run2b luminosity increase. Since almost 80% of the L1 rate is calorimeter based, the importance of sharpening the Pt cut and the possibility to trigger on real objects like electromagnetic clusters and jets using the sliding window technique to reduce the input rate has been justified using a basic trigger tower granularity of 0.2 x 0.2. A possible implementation of a logical chain FADC-Digital Filter and Trigger algorithms Processor with various options in under study. Around 100 cards would be necessary replacing the 13 existing racks by 2 or 3.

The option to merge the output results of the electromagnetic cluster algorithms with the track trigger shows that a possible rate reduction of 2 could

be obtained for the L1 track trigger side. This option would need a finer granularity in phi (0.1 instead of 0.2) for the electromagnetic Trigger tower, will add some complexity to the pure calorimeter trigger chain:. The impact of that complexity has not yet been totally evaluated, but a minimum of factor 2 in number of cards (i.e. cost) should be obviously foreseen.

The possible scenarios for the various possible implementation options are under evaluation in order to propose a single baseline.

Finally, this project has a meaning if it is realized in time, i.e. working in 2004. A realistic schedule, milestones and resource organization is under study.

# **5 L1 Muon Trigger**

#### 5.1 Goals

The primary goal of the L1 Muon Trigger (L1MU) system for Run2b of the DØ experiment is to provide an unprescaled high  $P_T$  ( $P_T > 10$  GeV/c) single muon trigger of 1-2 kHz. Other L1 physics triggers may combine the L1 muon trigger with other L1 object triggers such as jets or electrons. Some physics triggers may utilize lower P<sub>T</sub> threshold L1 muon triggers combined with other L1 object triggers. The L1 trigger rates of these other triggers will either be lower than the single muon trigger or prescaled because of their lower physics priority. For purposes of this document, the high P<sub>T</sub> single muon trigger seems the best benchmark. In Run 2a, an additional goal is to provide an unprescaled 1-2 kHz low  $P_T$  dimuon trigger ( $P_T > 1.5 \text{ GeV/c}$ ). That goal is not presently extended to Run 2b.

# 5.2 Description of the Current L1 Muon Trigger

#### 5.2.1 Overview

Information on the L1MU trigger hardware including the technical design report can be found at http://hound.physics.arizona.edu/l1mu/l1mu.htm. Only a brief summary is provided here.

The L1MU trigger identifies muon candidates by using combinatorial logic that makes use of tracks from the L1 Central Fiber Tracker (L1CFT) trigger and hits from **all** muon detector elements. The muon detector elements include both drift chambers and scintillation counters.

A block diagram of the L1MU Trigger is shown in Figure 45. There are three custom VME crates of L1MU Trigger Cards (MTCxx's) corresponding to the central (CF), north (EFN), and south (EFS) geographic regions of the DØ detector. There is one custom VME crate that serves as a Muon Trigger Manager There are also four custom VME crates of Muon Centroid Finder (MCEN) cards and one custom VME crate of Muon Concentrator (MCON) cards. All VME crates reside on the detector platform and are thus inaccessible during data taking.

<sup>&</sup>lt;sup>7</sup> The six highest-p<sub>T</sub> tracks in each CFT trigger sector are sent from the first layer of track-finding trigger electronics before combination and collation by L1CTT.

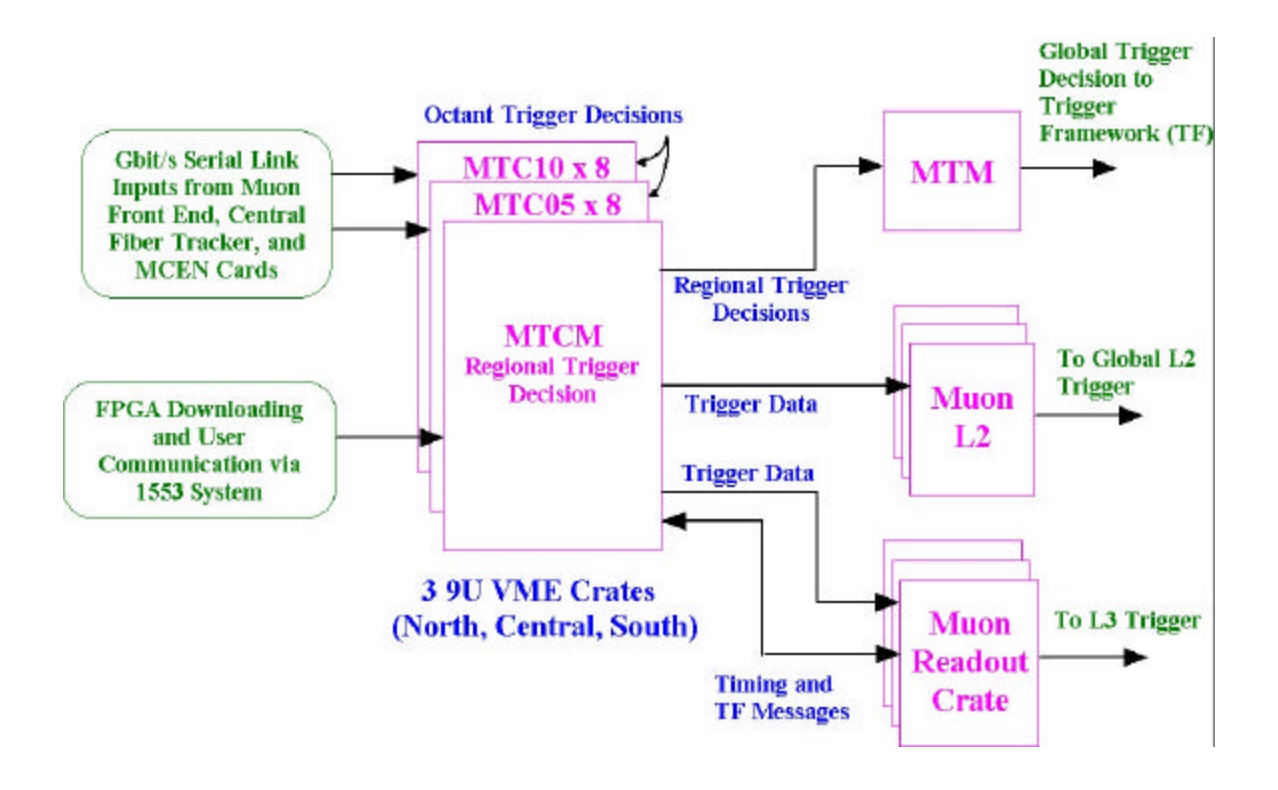


Figure 45. Block diagram of the L1MU trigger system.

Within each L1MU crate there are eight muon trigger "05" cards (MTC05 cards) and eight corresponding muon trigger "10" cards (MTC10 cards). Each geographic region is divided into octants and each MTC05 and MTC10 card makes local trigger decisions for one octant. The names "05" and "10" do not represent different levels of triggering but rather distinguish between those trigger decisions made primarily using L1CFT tracks combined with muon scintillator hits and those made primarily with muon wire chamber hits combined with muon scintillator hits. The muon trigger uses both "05" and "10" trigger decisions in a flexible, user-defined manner to determine whether a good L1 muon trigger has occurred.

A Muon Trigger Crate Manager (MTCM) card for each region collects the MTC05 and MTC10 trigger decisions for each octant to form several regional trigger decisions. These regional trigger decisions are collected by a Muon Trigger Manager (MTM) card that forms the 32 user-defined global L1MU trigger decisions sent to the trigger framework.

# 5.2.2 <u>Central Muon Trigger Algorithm (CF MTC05)</u>

For the CF MTC05 cards, tracks from the L1CFT Trigger are received on twelve cables with up to six tracks per cable. Ten of the cables are from L1CFT Trigger sectors corresponding to a muon detector octant plus one each from a sector in adjacent octants. Tracks from different cables are processed in parallel.

Each L1CFT Trigger track is currently described by its position in the outer layer of the CFT and its signed offset in the inner layer with respect to an infinite momentum track passing through the position in the outer layer of the CFT. This information can be used to determine the signed  $P_T$  of the L1CFT track. Currently only four groups of such inner layer offsets are possible corresponding to four  $P_T$  thresholds of 2, 4, 7, and 11 GeV/c. We (L1MU) call these thresholds PT1 to PT4 respectively. Tracks from the twelve cables are input simultaneously with subsequent tracks following every 18.8 ns. In the MTC05 FPGA logic, the  $P_T$ 's of the tracks are decoded and the outer layer positions are used to form "wedges" of CFT tracks that will be matched to  $\phi$  slices defined by the A-layer A-Phi counters.

Scintillator hit information from the A-Phi and Cosmic Cap scintillator counters is carried by the four remaining cables. Combinatorial logic is then used to find  $\eta$  and  $\varphi$  correlations in AC and AB scintillation counter hits. (Note the present B-layer scintillator coverage is modest and only fills in C-layer gaps.) A valid muon trigger is denoted by the corresponding  $\varphi$  slice of the A-layer A-Phi counter. The trigger conditions (correlations) are found separately for each of the four  $P_T$  thresholds. Finally, the L1CFT wedges are matched to the  $\varphi$  slices of the A-Phi triggers to form the CF MTC05 triggers. The results are output in two-bit counters that give the number (A # B # C) scintillation counters and (AC # AB) correlated counter patterns that have been matched to L1CFT wedges. There are separate two-bit counters for each  $P_T$  threshold. These counters are subsequently sent to the MTCM card for use in forming the central regional trigger decision.

## 5.2.3 <u>Central Muon Trigger Algorithm (CF MTC10)</u>

For the CF MTC10 logic three layers of PDT **hits** are received on thirteen input cables. The hits in each layer are used to find centroids (track stubs) in each layer using combinatorial logic. Scintillator hit information from the A-Phi and Cosmic Cap counters are input on the remaining three cables. The scintillator hit information is used to confirm that the PDT centroids came from this specific crossing. This step is necessary because the maximum drift time of the PDT's spans four or five 132 ns bunch crossings.

Next, using only scintillator-confirmed centroids, combinatorial logic is used to find good trigger conditions that are defined by correlations between centroids in different layers. The results are output in two-bit counters which give the number of (A # B # C) centroids and (AB # AC) correlated centroid patterns. (BC

patterns could also be used if needed.) These counters are subsequently sent to the MTCM card for use in forming the central regional trigger decision.

## 5.2.4 Forward Muon Trigger Algorithms (EF MTC05)

For the EF MTC05 cards, tracks from the L1CFT Trigger are received on twelve cables with up to six tracks per cable. Ten of the cables are from L1CFT Trigger sectors corresponding to a muon detector octant plus one each from a sector in adjacent octants. Tracks from different cables are processed in parallel.

Each L1CFT Trigger track is currently described by its position in the outer layer of the CFT and its signed offset in the inner layer with respect to an infinite momentum track passing through the position in the outer layer of the CFT. This information can be used to determine the signed  $P_T$  of the L1CFT track. Currently only four groups of such inner layer offsets are possible corresponding to four  $P_T$  thresholds of 2, 4, 7, and 11 GeV/c. We (L1MU) call these thresholds PT1 to PT4 respectively. Tracks from the twelve cables are input simultaneously with subsequent tracks following every 18.8 ns. In the MTC05 FPGA logic, the  $P_T$ 's of the tracks are decoded and the outer layer positions are used to form "wedges" of CFT tracks that will be matched to  $\phi$  slices defined by the A-layer Pixel counters.

Scintillator hit information from the A-, B-, and C-layer Pixel counters is carried by the four remaining cables. Combinatorial logic is then used to find a good muon "track" defined by  $\eta$  and  $\phi$  correlations in the AB and AC-layer Pixel counter hits. (BC-layer combinations could be used if needed.) A valid L1MU trigger is described by the corresponding  $\varphi$  slice of the A-layer Pixel counter. The trigger conditions (correlations) are found separately for each of the four  $P_T$  thresholds. Finally, the L1CFT wedges are matched to the  $\varphi$  slices defined by the A-layer Pixel triggers to form the EF MTC05 triggers. The results are output in two-bit counters which give the number of (A # B) Pixels and (AB # AC) correlated Pixel patterns that have been matched to L1CFT wedges. There are separate counters for each  $P_T$  threshold. These counters are subsequently sent to the MTCM card for use in forming the forward regional trigger decision.

### 5.2.5 Forward Muon Trigger Algorithms (EF MTC10)

For the EF MTC10 logic three layers of MDT **centroids** are received on twelve input cables. The MCEN cards use MDT hits to first find the MDT centroids. Scintillator hit information from the A-, B-, and C-layer Pixel counters input on the remaining four cables. The scintillator hit information is used to confirm the MDT centroids.

Next, using only scintillator-confirmed centroids, combinatorial logic is used to find good trigger conditions that are defined as correlations between centroids in different layers. The results are output in two-bit counters which give the number (A # B) centroids and (AB # AC) correlated centroid patterns. These two-bit counters are subsequently sent to the MTCM card for use in forming the forward regional trigger decision.

#### 5.3 Performance of the Current Muon Detector

Only one relevant aspect is reported here. The occupancies of the Pixel counters in the A-, B-, and C-layer per minimum bias event per octant are 3%, 0.7%, and 1.4% respectively. The occupancies of the MDT chambers in the A-, B-, and C-layers per minimum bias event per octant per number of planes (decks) are 2.3%, 0.6%, and 1.3 % respectively. These numbers are quite low and in agreement with our expectations based on old Monte Carlo simulation. We need to re-check these numbers with current Monte Carlo samples. We must also study the occupancy as a function of luminosity. However at least in the forward region, we feel that the substantial beamline shielding installed for Run 2a appears to be doing its job.

# 5.4 Performance of the Current L1Muon Trigger

Some elements of the L1MU trigger have been operational since the start of Run 2a. Others elements are not yet operational. Presently, the L1MU trigger consists of two-layer scintillator coincidences in the central and forward muon detector regions. The two-layer requirement imposes at  $\sim$ 3-4 GeV/c momentum threshold on the muons. Single muon triggers using reasonably tight "roads" are operational in both regions. Dimuon triggers are operational in both regions as well. Muon plus jet triggers are defined in the central muon detector region only as no calorimeter triggers currently exist in the calorimeter EC region. Trigger rates for existing L1MU triggers at L=5x10 $^{30}$  /cm $^{2}$ /s are given in Table 29.

Table 29. Trigger rates for existing L1MU triggers at  $L=5x10^{30}$  /cm<sup>2</sup>/s.

Trigger	Description	Rate (Hz)
mu1cmsc_fz	Single muon trigger - central region	135
mu2cmsc_fz	Dimuon muon trigger -central region	2
mu1pix_fz	Single muon trigger - north or south region	76
mu2pix_fz	Dimuon trigger - north or south region	<1
mu1cmsc_j5_fz	Single muon + jet trigger - central region	<1
mu1cmsc_j10_fz	Single muon + jet trigger - central region	<1

Elements currently missing from the L1MU trigger are the MTC10 triggers using the PDT's and MDT's and the MTC05 triggers using the L1CFT trigger. The MTC10 triggers using PDT's exist but problems with PDT front-end board timing have prevented us from fully commissioning this trigger. MTC10 triggers

from the MDT's await the installation of the MCEN system that finds MDT centroids. The MCEN system will be installed during the October 2001 accelerator shutdown. Information from the L1CFT trigger awaits installation of the L1CFT and other CFT electronics. The L1CFT and other CFT electronics will also be installed during the October 2001 accelerator shutdown.

Data analysis of the purity and efficiency of L1MU triggers is just beginning. Using the d0ve event display we find that approximately 20% of the L1MU triggers in the forward region have good tracks by eye. Good here is defined as three layers of pixel scintillation counters and three layers of MDT track stubs. (Recall the L1MU trigger just requires two layers of pixel counters.) An analysis using reconstructed muon tracks (with muon detector elements only) gives a somewhat smaller number but also includes unknown reconstruction efficiency. Results on the purity of the L1MU trigger in the central region are poorer and studies are underway to understand this.

# 5.5 Estimating the Run 2b Performance of the L1 Muon Trigger

We are presently missing **the** key element of the L1MU trigger, namely the L1CFT trigger. Hence estimating the Run 2b performance of the L1MU trigger is difficult. We have three pieces of information: current data rates, L1MU simulator rates performed 1997, and current L1MU simulator rates.

Figure 46 and Figure 47 show the measured single muon L1MU Trigger rates in the central and forward regions. As described above, these triggers do not include the L1CFT or the PDT and MDT triggers. The fast z (minimum bias) requirement is presently part of the trigger definition. The central region data use an 88ns (wide) timing window for good scintillator hits on the scintillator front-end cards. The forward region data use a 40ns (narrow) timing window for good scintillator hits.

Table 30 contains measured rates for  $L = 2 \times 10^{30} / \text{cm}^2 / \text{s}$  and estimated rates for  $2 \times 10^{32}$  and  $5 \times 10^{32} / \text{cm}^2 / \text{s}$ .

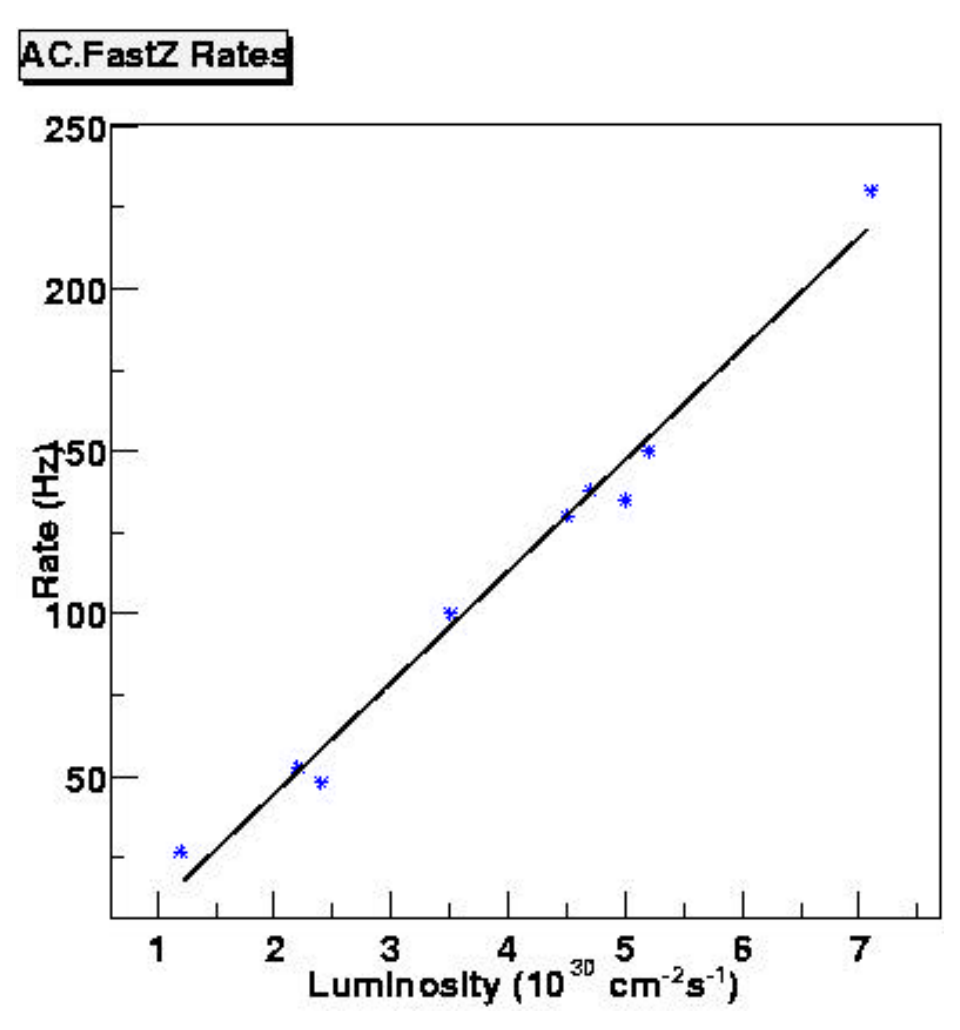


Figure 46. Measured single muon L1MU trigger rate in the central region.

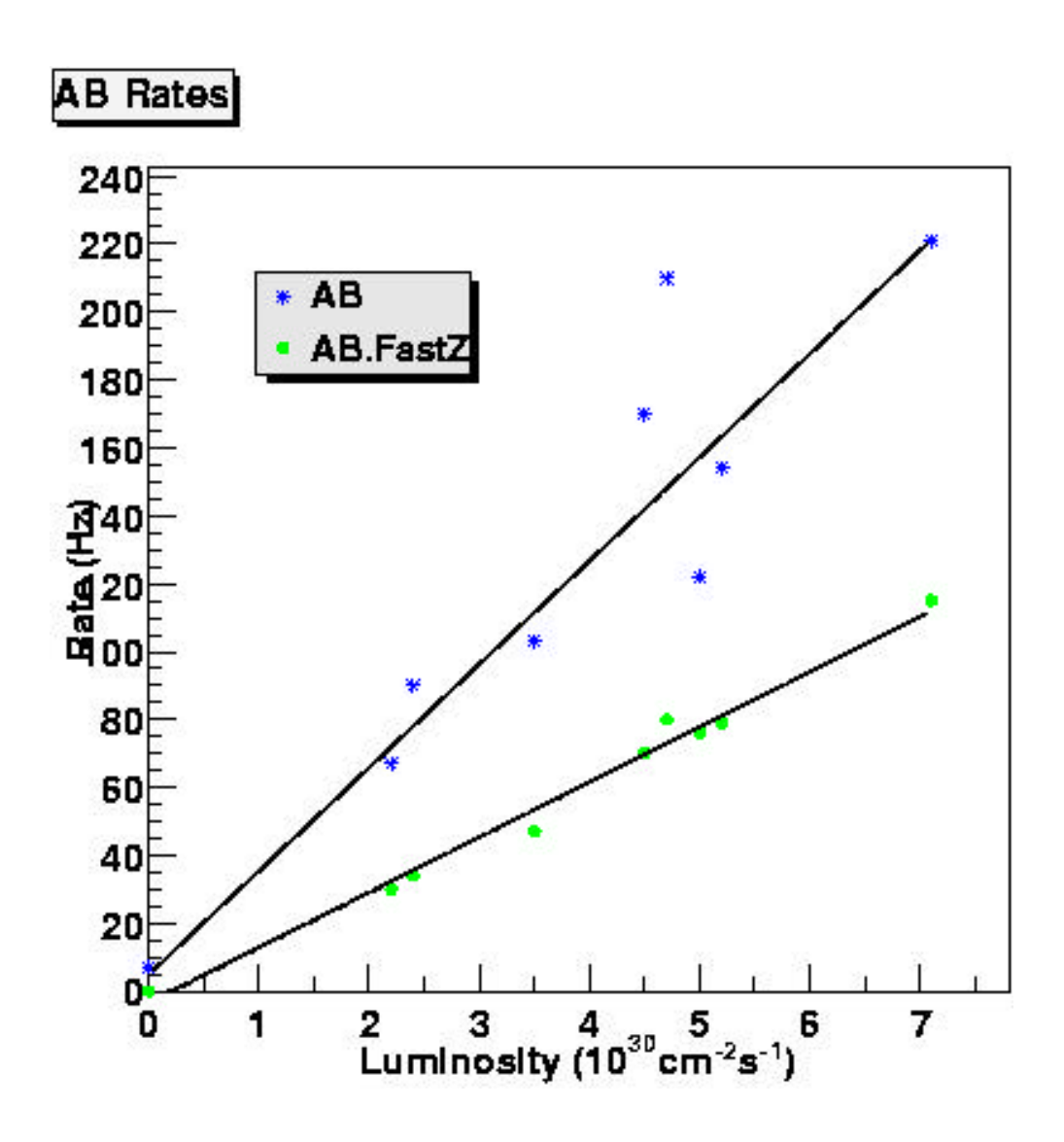


Figure 47. Measured single muon L1MU trigger rate in the forward region.

Table 30. Measured rates for L =  $2 \times 10^{30}$ /cm<sup>2</sup>/s and estimated rates for  $2 \times 10^{32}$  and  $5 \times 10^{32}$  /cm<sup>2</sup>/s.

Trigger	Measured Rate (Hz) at L= 2 x 10 <sup>30</sup> /cm <sup>2</sup> /s	Estimated Rate (Hz) at L= 2 x 10 <sup>32</sup> /cm <sup>2</sup> /s	Estimated Rate (Hz) at L= 5 x 10 <sup>32</sup> /cm <sup>2</sup> /s
Single muon - central region	40	6800	17000
Single muon - forward region	30	3000	7500

Tightening the timing window from 88 to 40 ns for good hits on the scintillator front-end cards reduces the rates by roughly a factor of 2. This was recently implemented in the forward region scintillator front-end cards and is included in the forward region rate estimates above. On the other hand, removing the fast z (minimum bias) requirement increases the rates by roughly the same factor. (Since we don't know the efficiency of the fast z requirement for muons it might be removed at some later date.)

At some level, these rates are encouraging. We have yet to include the PDT and MDT L1MU triggers. We have yet to include the L1CFT tracks. The timing window for good hits on the scintillator front-end cards might possibly be narrowed even further. Assuming the L1MU triggers can take ~2kHz of the ~6kHz L1 trigger bandwidth at the highest luminosity, a reduction of ~x7 is needed which we believe possible with the above mentioned elements still to be brought to bear.

On the other hand, these numbers can be used to estimate the L1MU trigger rates if the L1CFT fails to provide any rejection at high luminosity. Achieving the x5 reduction with just the PDT and MDT triggers is probably difficult but factors of x2-3 may not be.

A Fortran-based L1MU trigger simulator was used in 1996-1997 to help design the L1MU trigger algorithms. A selection of rates from that era is given in Table 31.

Table 31. Selection of rates from the Fortran-based L1MU trigger simulator.

Trigger	Description	Rate (Hz) for QCD + 1 Min Bias	Rate (Hz) for QCD + 4 Min Bias	Rate (Hz) for QCD + 6 Min Bias
L1CFT only – PT4	L1CFT only for P <sub>T</sub> > 11 GeV/c	3395	51364	440929
L1MU(1,PT1, Loose, Central)	L1CFT & One- Layer Scintillator,	13546	96365	117114
	P <sub>T</sub> > 2 GeV/c,  η  < 1.0			
L1MU(1,PT4, Loose, Central)	L1CFT & One- Layer Scintillator,	92	617	81
	P <sub>T</sub> > 11 GeV/c,  η  < 1.0			
A-layer PDT	PDT A centroid only	65356	278012	364892
AB & AC-layer PDT	MTC10	950	5632	9636
L1MU(1,PT1, Loose, Forward)	L1CFT & One- Layer Scintillator,	30123 x 2	148251 x 2	252096 x 2
	$P_T > 2 \text{ GeV/c}, 1.0 < $ $\eta < 2.0$			
L1MU(1,PT4, Loose, Forward)	L1CFT & One- Layer Scintillator,	13 x 2	4 x 2	4 x 2
	$P_T > 11 \text{ GeV/c}, 1.0 < $ $\eta < 2.0$			
A-layer MDT	MDT A centroid only	28292 x 2	70509 x 2	124490 x 2
AB-layer MDT	MTC10	26 x 2	24 x 2	75 x 2

### A few comments on Table 31:

- The L1CFT trigger with the highest P<sub>T</sub> threshold (PT4) has a 1% firing rate with 4 minimum bias interactions and a 10% firing rate with 6 minimum bias interactions.
- The x 2 in Table 31 is given because the rates were estimated for the North region only.
- Note the dramatic fall-off of rates once a muon detector layer outside the toroid iron is included in the trigger. Compare the PDT or MDT triggers for example.
- One of the easiest methods to reduce the L1MU trigger rates is to include muon detectors outside the toroid. However one must be equally concerned about loss of efficiency.

The L1MU Trigger rates of the L1CFT Trigger coupled with muon detector elements appear to be survivable at the highest luminosities. The rates in this case, however, are based on very few background events passing the trigger requirements. The trigger rates could be higher if more Monte Carlo had been available at that time because one event carrying a large weight could significantly increase the estimated rate.

Finally, we also have some relative rate estimates using the current DØ C++ trigger simulator. We do not quote an absolute rate but rather simply compare numbers of events with 0.7 and 5.0 minimum bias events with  $p_{\rm T}$  (hard scatter) > 2 GeV/c . Results are included in Table 32. Note that timing window cuts on the scintillator hits have **not** been applied here. Including them would likely reduce the number of events passing the various trigger conditions. The study to determine this rejection factor in the simulator is in progress.

Table 32. Muon trigger rates estimated using Run 2trigger simulator.

Trigger	Description	Number Passed per 16k events	Number Passed per 16k events
		QCD + 0.7 minimum bias events	QCD + 5.0 minimum bias events
L1MU(1,PT1, Loose,Central)	L1CFT & One-Layer Scintillator,	38 (2.3x10 <sup>-3</sup> )	958 (5.9x10 <sup>-2</sup> )
	$P_T > 2 \text{ GeV/c},$		
	η  < 1.0		
L1MU(1,PT4, Loose,Central)	L1CFT & One-Layer Scintillator,	1 (6.2x10 <sup>-5</sup> )	113 (7.0x10 <sup>-3</sup> )
	P <sub>T</sub> > 11GeV/c,		
	η  < 1.0		
L1MU(1,PT4,	L1CFT &	0 (0)	1 (6.2x10 <sup>-5</sup> )
Tight,Central)	Two-layers Scintillator,		
	P <sub>T</sub> > 11 GeV/c,		
	η  < 1.0		
L1MU(1,PT4,	L1CFT &	1 (6.2x10 <sup>-5</sup> )	149 (9.3x10 <sup>-3</sup> )
Loose, Central+Forward)	One-Layer Scintillator,		
	P <sub>T</sub> > 11 GeV/c,		
	η  < 1.5		
L1MU(1,PT4,	L1CFT &	0 (0)	1 (6.2x10 <sup>-5</sup> )
Tight, Central+Forward)	Two-Layers Scintillator,		
	P <sub>T</sub> > 11 GeV/c,		
	η  < 1.5		

As a crude consistency check, we can compare the trigger rates from the old and new simulators. In the current C++ simulator if one assumes that 16k events corresponds to the maximum trigger rate of 5 MHz, then the trigger rates of

L1MU(1,PT1, Loose, Central) and L1MU(1,PT4, Tight, Central) are 12k and 300 Hz respectively. These rates compare reasonably well with the corresponding numbers from the older Fortran simulator of 14k and 100 Hz.

The points to note from Table 32 are:

- The Loose (L1CFT plus one-layer of scintillator counters) L1MU Trigger rates significantly increase as more minimum bias events are added to the event. Again note however that timing cuts have **not** been applied in this particular analysis.
- The Tight (L1CFT plus two-layers of scintillator counters) L1MU Trigger rates are small even at high luminosities. Again, the iron toroids serve as an effective shield of background of particles coming from the calorimeter and hence keep the L1MU Trigger rate low. There is loss of signal efficiency though as discussed below.

Finally, we do not have a comparison of data versus simulator rates since non-L1CFT triggers were never implemented in the simulator. Work is underway to add the current L1MU triggers used in data-taking to the simulator so that this comparison can be made.

#### 5.6 Run 2b Issues

Given the present lack of an L1CFT trigger in the experiment, it is difficult to argue that the L1MU trigger (which relies heavily on the L1CFT trigger) will not function in Run 2b. On the other hand, data rates and Monte Carlo background rate estimates can be used to offer weak evidence that the L1MU trigger will be useable in Run 2b. Any sound estimate must wait until early in 2002 when the L1CFT trigger is operational.

There are several other L1MU issues related to Run 2b. These include PDT aging, central muon detector acceptance, central C-layer scintillator shielding, and the trigger decision time.

Aging of the PDT's in Run 1 was a major problem and a main motivation for replacing the PDT's in the forward region with MDT's. A number of steps were taken to reduce the effect of aging for the PDT's remaining in the central region for Run 2a. The A-layer PDT's are the most susceptible to aging and the most difficult to clean. In their case, the source of aging was removed by replacing the glasteel pads with G10 pads. It is expected that the aging of the A-layer PDT's will be greatly reduced although the actual rate from Run 2a collider running is unknown.

Most of the B and C-layer PDT's retain their glasteel pads for Run 2a and aging in their case is a real concern. The absence of the Main Ring will certainly reduce the aging rate. To further help minimize the effects of outgassing from the glasteel, the gas flow rate was increased for Run 2a. Nonetheless, the chambers will age and require periodic cleaning. Again, the actual aging rate due to Run 2a collider running is not yet known for the B and C-layers. It will be measured by tracking the pad gains. It is reasonable to assume that the B and

C-layer PDT's will require cleaning several times during Run 2b. One could contemplate replacing the PDT's with MDT's or replacing the glasteel in the remaining PDT's. Both are large, manpower intensive jobs and the former is likely prohibitively expensive.

Except in the bottom two octants, the acceptance of the A-Phi scintillator is above ~90%. There is some loss of efficiency for  $0.8 < |\eta| < 1.0$ . The Cosmic Cap efficiency is ~80%. There is more loss in the  $0.8 < |\eta| < 1.0$  region. The Tight (two-layer) L1MU Trigger efficiency in the central region is shown in Figure 48. The trigger efficiency in the bottom can be improved to 80% by requiring only a single layer of counters.

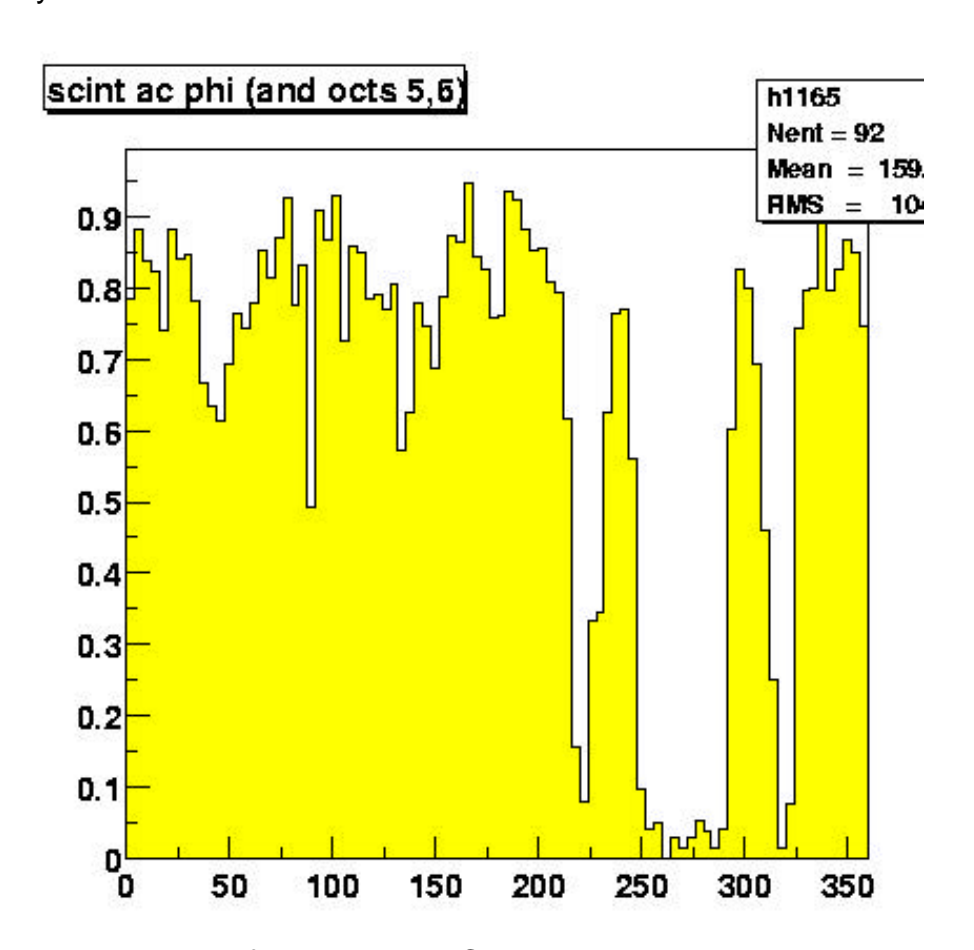


Figure 48. Acceptance of the AB- and AC-layer scintillator in the central region.

Because the L1MU trigger rates drop dramatically when scintillator outside the iron toroid is included, it is important to keep the efficiency of the B- and C-layer scintillator high (see Figure 49). Increasing the outside scintillator efficiency might be achieved by the addition of some amount of B-layer scintillator. We will investigate available space in the B-layer during the October 2001 accelerator shutdown when we have access to the collision hall. Alternatively, more clever trigger algorithms that allow A-layer only triggers at

large  $|\eta|$  and AC layer coincidences elsewhere could possibly be employed. Neither improvement has yet been studied in detail.

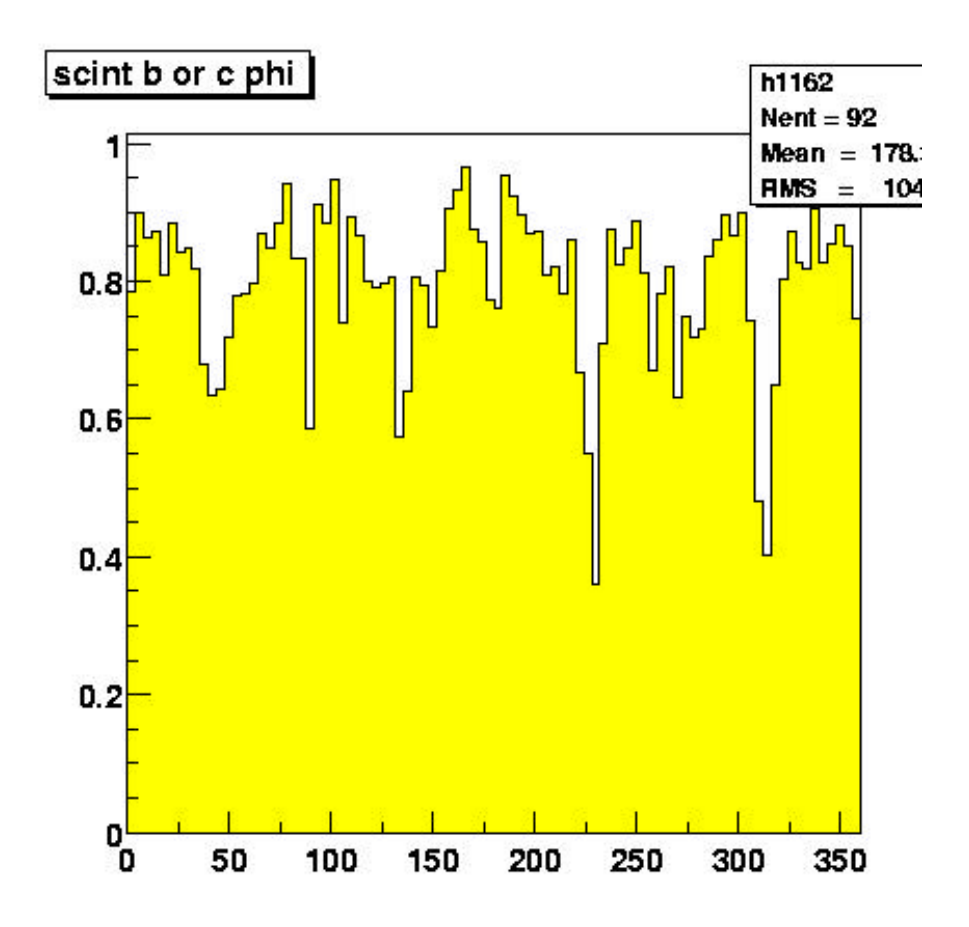


Figure 49. Acceptance of the B- and C-layer scintillators in the central region.

Hits in the C-layer Cosmic Cap counters are dominated by radioactivity in the collision hall ceiling and walls. The main source is  $^{22}$ Na that produces 1.3 MeV photons with a half-life of 2.6 years. The present C-layer singles rate with (L = 2.5-3 x  $10^{30}$  /cm²/s) and without beam are 1.15 MHz and 1.07 MHz respectively. Thus at a threshold of  $V_T = 10$  mV and a wide (88 ns) time window, the singles rates are dominated by the low energy photons. While ~1 MeV photons are notoriously difficult to shield, work is underway to measure the reduction in singles rate using a thin sheet of Pb for shielding.

For Run 2a, it was agreed upon by all electronics groups that the total L1 trigger decision time would  $25 \times 132$  ns = 3300 ns. This is the time between a bunch crossing and the time when an L1 subsystem trigger decision must reach the Trigger Framework. Unfortunately, the designers of silicon and central fiber electronics did not respect this specification and as a result do not have sufficient pipeline depth to hold front-end-data for this period of time. This later statement applies to 132 ns bunch crossing operation in the accelerator. These groups have been pressing for a reduction of  $2-4 \times 132$  ns in the L1 trigger decision time

to regain sufficient pipeline depth. These groups have also been investigating other solutions in their own electronics, some of which appear very promising.

The present L1MU decisions times are given in Table 33.

Table 33. Present L1MU decision times.

Trigger	L1MU Decision Time (ns)	
CF MTC05	3095	
CF MTC10	3222	
EF MTC05	3057	
EF MTC10	3260	

The above numbers come from a detailed spreadsheet that combines both real timing measurements and estimates. Comparison of the spreadsheet with a real measurement shows the real decision time for the current L1MU triggers to be 200 ns less than our estimate for the current L1MU triggers. We do not understand the source of this discrepancy at the present time. Nevertheless, it may mean that we do have 1-2 x 132 ns to spare, but likely not 3-4.

In the event that DØ decides to reduce the L1 trigger decision time, the impact on the L1MU trigger system would be significant. In this case, possibly two elements of the L1MU trigger (the CF and EF MTC10 trigger decisions) would either cease to function or would function much less effectively. The latter would be true if we had to greatly simplify the processing and signal-handling in order to meet the time budget. Another possibility would be to produce new muon trigger flavor boards with faster FGPA's in order to meet this time budget but we have not investigated this option to date.

## 5.7 Summary

There is weak but positive evidence that the L1MU trigger will allow unprescaled single muon triggers in Run 2b. Important information will be gained once the L1CFT trigger becomes operational. At the moment we do not foresee major Run 2b upgrades for the L1MU trigger. There are items however that can increase the effectiveness of the L1MU trigger. These include additional scintillator in the central region to increase the acceptance of two-layer L1MU triggers in the central region and Pb shielding for the C-layer Cosmic Cap counters. We did not investigate the replacement of the PDT chambers at this time. The loss of PDT and MDT trigger capability because of a reduced L1 trigger decision time is of some concern and solutions are being sought in consultation with the silicon and central fiber tracker electronics group.

# **6 Level 2 Triggers**

#### 6.1 Goals

The input rate to L2 is limited by the SMT digitization deadtime, and the output rate is limited by the calorimeter precision readout deadtime. Since neither of these differs from Run 2a, the primary charge for Level 2 will be to maintain the current rejection, with the same time budget, despite some of the algorithms used in Run 2a Level 2 trigger being moved upstream to Level 1 for Run 2b.

To accomplish this goal, Level 2 must make better use of the time budget by using more powerful processors. This project is already under way, to deal with manufacturing problems in the Run 2a Alpha processors. In addition, the Level 2 trigger preprocessor which uses SMT data, the L2STT (Silicon Tracking Trigger), must also be upgraded to match the physical configuration of the Run 2b SMT.

## 6.2 L2b Upgrade

## 6.2.1 Concept & physics implications

The motivation for upgrading from Alpha processors to  $L2\beta$  processors is twofold. First, the existing complement of available Alpha processors is insufficient to implement the baseline L2 trigger.

The first production run of alphas yielded 2 stable alpha boards, and 7 more boards operating with varying degrees of reliability. A second production run of 12 alphas is in progress, with a maximum yield of 12 boards. The baseline system required 16 processors in the trigger crates, and another 6 or so in test and algorithm development facilities. We will adapt our plans to the resources available, combining Administrator nodes (one per crate) and Worker nodes whenever possible. The current commissioning efforts are proceeding with a single Alpha processor per crate. Eventually, as luminosity increases, we will likely have problems accomplishing all processing within the time budget.

Thus the first purpose of L2 $\beta$  processors is to replace unreliable processors and to increase the number of processors up to the amount required for smooth running in Run 2a.

The second purpose of L2 $\beta$  processors is to increase the computing resources available to Level 2. The processors we can purchase currently are roughly 2-3 times as powerful as Alpha processors, according to standard benchmarks. For Run 2b, a subset of the most heavily-loaded processors should be replaced with higher-performance processors. Assuming that processors in the format used by the L2 $\beta$ s increase performance by Moore's law, a purchase near the start of Run 2b could gain another factor of 4 in processing power over current  $\beta$  processors.

The most obvious use of additional CPU power would be in the global processor, which does the work of final Level 2 trigger selection by combining the results of preprocessors across detectors. More powerful CPU's will allow us to

break the present software restriction of one to one mapping of Level 1 and Level 2 trigger bits (128 each at this point). This would allow more specific trigger processing to be applied to individual L1 trigger conditions at Level 2, as we currently do in Level 3.

We have begun to study algorithms that might profit from additional CPU power. Multi-track displaced vertices could be searched for with the tracks output by the L2STT. This is beyond the original projected work of the L2CTT preprocessor, and might be time intensive. A neural-net filter might search for tau events in the L2 Global processor. The effectiveness of such improvements depend on the actual mix of triggers chosen for Run 2b physics, so these should only be considered as examples. We have not yet studied which algorithms can be imported from Level 3 and applied to the lower-precision data available in Level 2, nor have we determined the bottlenecks for the present Level 2 trigger in detail.

# 6.2.2 <u>Implementation</u>

Rather than attempt a complete redesign of the Alpha processor board, we use a more modular approach, taking full advantage of industry-standard components and upgrade paths. We follow the same conceptual design for the function of the board in our Level 2 system. Moreover, we <u>require</u> both hardware and software compatibility between both Alphas and L2 $\beta^8$ . This not only facilitates more seamless integration into the experiment, but also offers a great economy in the manpower required to commission the new system.

The L2 $\beta$  implementation replaces the CPU and assorted computer peripheral functions with a commercially produced single board computer (SBC). This SBC will reside on a 6U CompactPCI (CPCI) card providing access to a 64-bit, 66 MHz PCI bus via its rear edge connectors. Such cards are currently available "off the shelf" from several vendors including Advantech<sup>9</sup>, Diversified Technology Inc.<sup>10</sup>, and Teknor<sup>11</sup>. The remaining functionality of the board will be implemented in a large FPGA and Universe II<sup>12</sup> VME interface mounted on a 6U-to-9U VME adapter card as shown in Figure 50.

The adapter card will contain all DØ-specific hardware for Magic Bus and trigger framework connections. The SBC, in the adapter, will have its front panel at the face of the crate and will be easily removable. This implementation offers several clear advantages:

• The modular design, incorporating existing CPU cards, greatly reduces the engineering, debugging, and prototyping required for the system.

-

<sup>&</sup>lt;sup>8</sup> Extensive documentaion on L2βeta can be found at the project's website: http://galileo.phys.virginia.edu/~rjh2j/l2beta

<sup>&</sup>lt;sup>9</sup> http://www.Advantech-nc.com.

<sup>10</sup> http://www.dtims.com.

<sup>11</sup> http://www.teknor.com

<sup>&</sup>lt;sup>12</sup> Tundra Semiconductor Corp., http://www.tundra.com.

- The modular design provides a clear path for CPU performance upgrades by simple swapping of SBC cards.
- Hardware compatibility allows for a phased-in replacement of the Alphas.

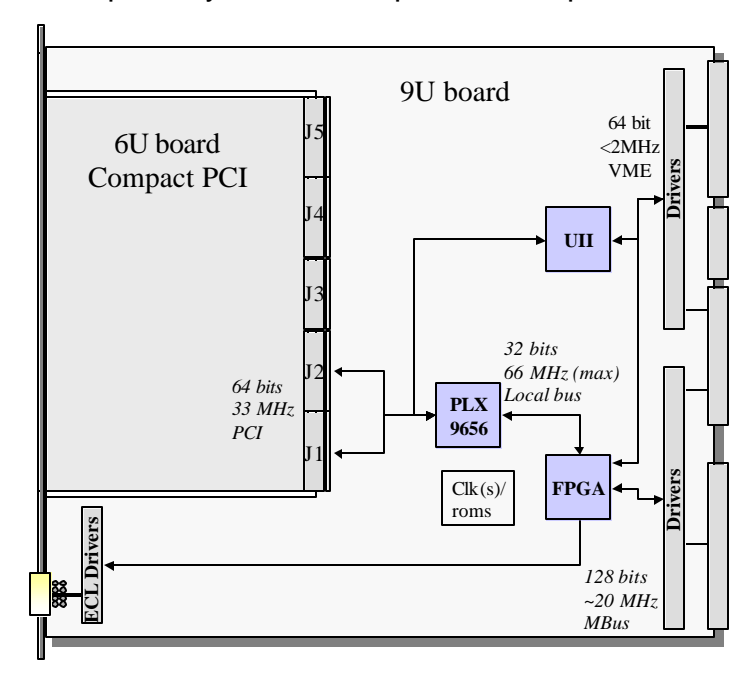


Figure 50. Physical model for the L2 $\beta$  processor card. Connectors J1 and J2 provide the 64-bit CPCI connection to the CPU. The functions available on the J3-J5 connectors may be assigned arbitrarily by each board manufacturer.

- Higher or lower performance CPUs may be selected. For example, lower performance, less expensive CPUs may be used in Administrator-type processor cards, while more powerful CPUs can be used where physics algorithms are run.
- The use of a much smaller number of components to implement the DØspecific functions of the board greatly reduces the parts count, increasing reliability and ease of hardware debugging.

As described above, the L2 $\beta$ s will be composed of two separate devices: a commercial single board computer with a 64-bit CPCI interface and a custom 6U-to-9U adapter card. To minimize development time and to maximize chances of success for the L2 $\beta$ s, our philosophy has been to use commercial devices where custom devices can be replaced, to simplify the electrical design of the boards as much as possible, and to push as much of functionality as possible into firmware to reduce hardware prototype cycles.

Initially, we plan to use the MC-3385 CPCI SBC<sup>9,13</sup> as our processor in the L2βs. This board (and others in its class) can accept dual Pentium CPUs (up to 933 MHz). As shown in Table 34, these CPUs offer substantial performance gains over the 500MHz Alphas. The SBC supports a local 64-bit wide PCI bus that runs at 33 or 66MHz and, via a PCI-PCI bridge, it provides a 64-bit CPCI interface also supporting both 33 and 66 MHz bus speeds.

Table 34. Performance comparisons <sup>14</sup> for several modern CPUs available on mass-produced VME single board computers. The current Level 2 Alpha CPU is shown at the top of this table. The integer performance of the CPUs is of primary importance for most of the operations in  $D\emptyset$  's trigger.

CPU Type	SpecInt95	SpecFP95
Alpha 500 MHz	~15	~21
PIII 800 MHz	~38	~29
PIII 850 MHz	~41	~35
PIII 933 MHz	~45	~39
PIII 1000 MHz	~48	~41

All of the CPCI cards are supported under Linux. And the KAI C++ compiler is readily available for this platform and OS. The KAI compiler and Pentium Linux are fully supported in the DØ Experiment this offers additional convenience for software support of the system as compared to the Level 2 Alphas using COMPAQ's Cxx compiler. Developing online code for the Alphas under Linux facilitates our move to L2\beta hardware, and the similarity of byte-ordering in the Alpha and PIII processors simplifies the transition.

The 9U card will both adapt the 6U SBC card to the 9U crate form factor and provide hardware for all custom I/O required of the processor cards. This includes all Magic Bus (MBus) I/O, an interface to user-defined VMEbus J2 lines, the VME interface and outputs to trigger scalers.

Details of the 9U adapter card are shown in Figure 50. The adapter will contain a Universe II PCI-to-VME interface and all custom I/O functions on this card will be implemented in a single FPGA plus assorted logic converters and drivers. The FPGA of choice is the Xilinx XCV405E<sup>13,15</sup>. This device is particularly suited to our application, because of its large amount of available Block RAM. 70KB of RAM (in addition to >10K logic cells) is available to implement internal data FIFOs and address translation tables for broadcasting data from the Magic bus to CPU memory, thus greatly reducing the complexity of the 9U PCB. A 64-bit,

<sup>15</sup> Xilinx XCV405E, http://www.xilinx.com, go to VIRTEX-EM products.

See documents at: http://galileo.phys.virginia.edu/~rjh2j/l2beta/#components.
 Information on Spec measurements can be found at http://www.specbench.org.

33MHz PCI interface to the CPCI card will be implemented with a PLX 9656 PCI Master chip<sup>13,16</sup>.

The following requirements will be satisfied in the design of the L2 $\beta$ s to meet or exceed the Alpha's capabilities:

- The 9U board/SBC will exceed the DMA performance of the Alphas. Although the theoretical bandwidth of the PC164's bus is 264 MB/s, the Alpha board typically realizes 80-100 MB/s due to internal buffer limitations. While the PCI front end of the PLX is capable of delivering data at the full 264MB/s, we expect the L2β's effective throughput to be 80-90% of this limit due to the need to broadcast data that is translated into non-contiguous DMA packets.
- On-board FIFOs must be able to receive bursts of data up to the full 320MB/s bandwidth of the Magic Bus. This is accomplished by implementation of fast FIFOs within the Xilinx FPGAs block RAM sections.
- It will be possible for the DMA to be preempted by pending Magic bus I/O requests. An advantage of the new design is that system performance may be fine tuned by configuration of PCI Latency timers and local bus DMA abort logic.
- DMA destinations will be configurable by the CPU for all MBus broadcast addresses. The full functionality of the DMA Mapper (responsible for converting MBus addresses to Memory target addresses) as used in the Alphas will be implemented in a functionally identical way inside the Xilinx.
- It will be possible to interrupt the PCI bus in accordance with events on the local bus (DMA complete, new event arrival, etc). The PLX explicitly supports generation of interrupts from the PLX local bus. The new hardware also supports the use of more convenient interrupt implementations (MSI) defined in the latest PCI specifications <sup>17</sup>.
- Magic Bus Programmed I/O (PIO) will be able to support a number of data modes: Master/Write, Master/Read, Slave/Write, Slave/Read. In our design this is a matter for firmware only. Bi-directional drivers are provided to send or receive MBus data.
- Fast MBus arbitration (~15ns). This is consistent with realizable gate delay times in the Xilinx FPGA.

In order to minimize the demand on the experiment's resources to bring the  $L2\beta s$  to completion it is vital that this project tread as lightly as possible on other trigger groups' projects. We have planned at the onset that the  $L2\beta s$  are to be both hardware and software compatible with the Alphas. Hardware compatibility will largely be a product of proper firmware design. By software compatibility we are referring to high-level software. It should be possible to recompile online

<sup>&</sup>lt;sup>16</sup> http://www.plxtech.com.

<sup>&</sup>lt;sup>17</sup> Shanley and Anderson, "PCI System Architecture", Mindshare, 1999.

code with little or no changes to run on the  $L2\beta s$ . This compatibility will be enforced either by the hardware interface layer, or device driver software and API.

The L2 $\beta$  processors will run Linux Redhat Version 7.1 (kernel version 2.4). The OS version will remain fixed indefinitely for the duration of Run 2, unless there are Figure 5-5 Acceptance of the B- and C-layer scintillators in the central region.to upgrade. We will use the KAI compiler and all code will be built using the standard DØ software environment.

The coding tasks for this project can be displayed as in Figure 51. The device driver code will require a rewrite of the hardware interface layer, while the programmer interfaces for the device drivers will be unchanged from the present system. This is necessary for source code compatibility. A large fraction of this low-level software has already been tested. The UII driver will require the least amount of change. In fact, the current device drive code will function "as is" when the PCI base classes it depends on are fully replicated for the PIII boards. The remaining device driver code will have to be completely redesigned, since three former PCI devices will now live inside one FPGA. Different functions of this FPGA will be treated as pseudo-PCI devices to maintain a software interface compatible with the Alphas.

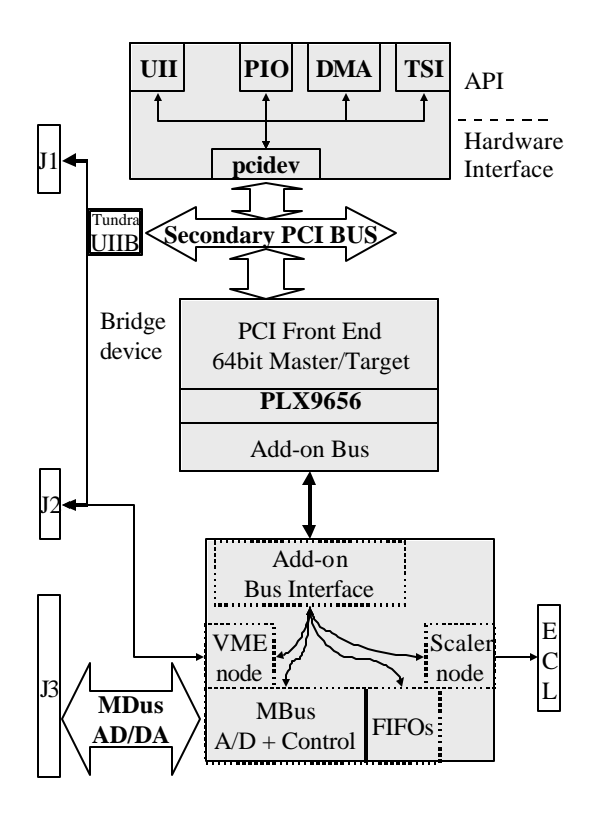
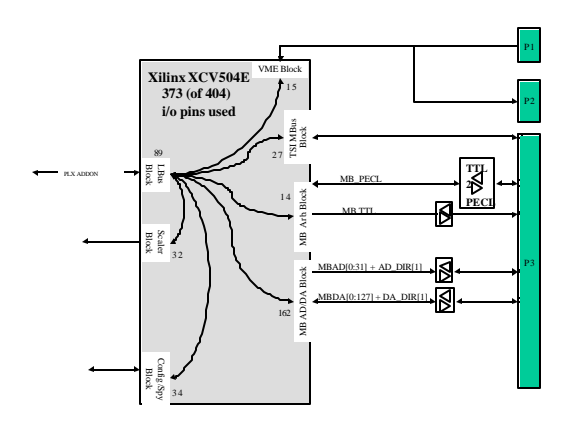


Figure 51. Block diagram of L2β software and firmware components.

The firmware will be composed in loosely coupled blocks similar to those shown in Figure 51. The most complex blocks will be the add-on bus interface

and the MBus I/O block. A more detailed summary of the firmware blocks and FPGA resources required is shown in Figure 52. In addition to I/O resources for required functions, "utility pins" are allocated for configuration settings and logic analyzer 'spy' channels for assistance in hardware and firmware debugging.



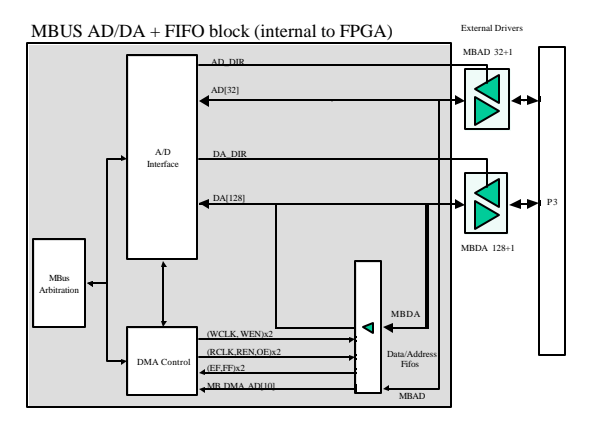


Figure 52. Overview of firmware blocks.

Figure 53. MBus I/O firmware blocks. I/O pin requirements are shown with each block.

Although we have sought to develop a system that is implemented in firmware to as large an extent as possible, we have, as mentioned above, chosen to use a hardware PCI interface rather than to overly complicate our firmware project with a PCI core implementation. We plan to take full advantage of the PLX's features to simplify the firmware design. The PLX 9656 provides a set of local configuration registers mapped to PCI Memory and I/O space and to a local bus address range. Additionally it provides four PCI memory windows for direct data transfers between PCI and local bus addresses. These memory windows will be configured to present interfaces similar to those used in the Alpha's devices. Perhaps the most interesting feature of the PLX 9656 is its ability to become a Master on both the PCI and add-on buses and to fully control DMA transactions. Thus we may simplify the DMA block of the firmware to a protocol that provides data words at the PLX's request. This removes all need for the Xilinx to directly support PCI timing, because the PLX completely decouples the two buses.

The MBus firmware (Figure 53) is responsible for controlling the MBus Data and Address drivers and the (internal) Data FIFOs. It must respond to a request from the PLX to send or fetch data (PIO Master), it must request that the PLX fetch or receive data (PIO Target), and it must provide data to the PLX for DMA transfers (FIFO readout).

The Trigger System Interface (TSI) is fully implemented in the Xilinx FPGA. This interface only functions as a PCI slave and is used to receive and send information to the rest of the trigger system. This includes the DØ trigger signals from the P2 backplane, as well as direct communication with the Trigger Control

Computer (TCC) through a front panel connector. It is also used for monitoring the status lines of the Magic Bus.

## 6.2.3 <u>Performance scaling</u>

Given comparable I/O capabilities, the amount of time required to run complex algorithms should be inversely proportional to the processor speed; more complicated algorithms can be used to process the available data if the processors are faster. However, a factor of two increase of processing power is more useful when supplied in the form of a single processor than in the form of a second identical processor working in parallel. This is because load balancing among multiple nodes is difficult in the Level 2 system due to constraints imposed by the front-end digitization. The front-end digitization holds buffers for 16 events awaiting Level 2 trigger decisions. A critical restriction in the system is that L2 results (accept or reject) must be reported to the front ends in the order in which the triggers were taken at L1. While one processor works on an event with a long processing time, other events will arrive and fill the 16 front-end buffers. Other processors working on these events will go idle if they finish processing them quickly, since they cannot receive new events until the pending decision on the oldest event is taken. Faster processing for each event in turn is thus more desirable than adding additional processors, once a baseline level of parallelism is established.

As one possible path to processor upgrades, we note that the L2 $\beta$  CPU card architecture allows equipping the cards with dual processors that share the card's memory and I/O. This upgrade is attractive because its incremental cost is low, but it would require a substantial software effort to turn it into increased throughput, even if it is possible to build code that takes advantage of the dual processors without writing thread-safe code. However, a dual-processor upgrade might be attractive for reasons other than performance. One processor could keep the Linux operating system active for debugging of problems in algorithms run in the second processor. Or one could run a production algorithm in one processor and a developmental version in the second processor. This second processor might even be operated in a "shadow" mode (as in Level 3), processing events parasitically, but skipping events if the developmental algorithm gets behind, or is being debugged.

### 6.2.4 Cost & schedule

The L2 $\beta$  project is underway, and consists of a fruitful collaboration between Orsay, University of Virginia, and University of Maryland. Orsay is designing and building the 9u boards, and writing the firmware. Virginia is specifying the processor, writing software, and (with Maryland) specifying firmware functionality. Testing and commissioning will take place at Orsay, then Virginia/Maryland, then at Fermilab. Fermilab has provided 50K of funds to get the project started. Orsay has provided contributions of 20K in cash and 127K in-kind (engineering and travel), and Virginia and Maryland have provided another 10K in-kind (travel). Manpower for testing, commissioning, and maintenance has also been committed. The baseline system provides for replacement of all alphas, including

the 14 alphas originally reserved for upgrades to the Level 2 trigger during Run 2a.

We direct the reader to Appendix B, which contains a cost estimate for that portion of the Level  $2\beta$  project associated with completion of the Run 2a system. Our estimate of the engineering needed is included. The total M&S is \$411k, and the total sub-project cost after the addition of 37% contingency is \$562k. Identified sources of funding are shown in the spreadsheet as well – these come to a total of \$192k, leaving \$370k remaining to be identified in order to complete the project. We include in Table 35 below the current milestones for the Run 2b Level  $2\beta$  project.

Table 35. Schedule milestones for the Level 2β project

		_
	One prototype round needed	Two prototype rounds needed
Final Prototype delivery	Jan 1, 2001	Mar 1, 2002
Hardware Verification	Mar 8, 2002	May 8, 2002
Begin production	Apr 8, 2002	Jun 8, 2002
Pre-production verification	Jun 8, 2002	Aug 8, 2002
Begin Installation	Aug 8, 2002	Oct 8, 2002
Final system	Sep 1, 2002	Nov 1, 2002

Fro Run 2b, we are proposing a partial upgrade of the Level  $2\beta$  system by allocating sufficient funds to replace the processors on 12 of the 24 boards. This is in anticipation of the potential increase in computing power that could at that time be used to implement more sophisticated tracking, STT, and calorimeter/track matching algorithms at Level 2 in response to the increased luminosity. Since this is an upgrade associated with Run 2b, we earmark this money for FY04 (see Table 47 in the Summary section at the end of this report). We base this estimate on our experience with the Run 2a Level  $2\beta$  system; the cost is estimated to be \$83k, including 34% contingency.

# 6.3 STT Upgrade

#### 6.3.1 Concept & physics implications

The D0 Level 2 Silicon Track Trigger (L2STT) processes the data from the L1 Central Track Trigger (L1CTT) and the Silicon Microstrip Tracker (SMT) to associate hits in the SMT with tracks found by the L1CTT. These hits are then fit together with the L1CTT information, thus improving the resolution in momentum and impact parameter, and the rejection of fake tracks.

Tracks with large impact parameter are indicative of long lived particles (such as b-quarks) which travel for several millimeters before they decay. The L2STT

thus provides a tool to trigger on events with b-guarks in the level 2 trigger. Such events are of particular importance for the physics goals of Run 2. The Higgs boson decays predominantly to  $b\overline{b}$  pairs if its mass is less than about 140 GeV/c<sup>2</sup>. The most promising process for detection of a Higgs boson in this mass range at the Tevatron is associate production of Higgs bosons with W or Z bosons. If the Z boson decays to neutrino pairs, the b-guarks from the Higgs decay are the only detectable particles. In order to trigger on such events (which constitute a significant fraction of associated Higgs production) the L2STT is essential to detect jets that originate from b-quarks at the trigger level. The L2STT will also allow the collection of a large enough sample of inclusive  $b\bar{b}$ events to see the decay  $Z \rightarrow b\bar{b}$ . Such a sample is important to understand the mass resolution and detection efficiency for  $b\overline{b}$  resonances, and to calibrate the calorimeter response to b-quark jets. The latter will help to drastically reduce the uncertainty in the top quark mass measurement, which is dominated by the jet energy scale uncertainty. Detailed descriptions of the physics benefits of STT are written up as DØ Notes<sup>18,19</sup>.

## 6.3.2 STT Architecture

The L2STT consists of three types of electronics modules:

- The Fiber Road Card (FRC) receives the data from L1CTT and fans them out to the other modules. It also receives SCL information from the TCC and initiates appropriate action, and manages the buffers used for storing processed data for readout by the VBD.
- The Silicon Trigger Card (STC) receives the raw data from the SMT front ends. These are then processed to find clusters of hit strips and associate these clusters with the tracks found by L1CTT.
- The Track Fit Card (TFC) fits a trajectory to L1CTT tracks and the SMT clusters associated with it. The results are then relayed to the Level 2 Central Track Trigger.

Each of these modules is based on the same 9U by 400 mm VME motherboard. Logic daughter boards carry out the main function of the three modules. VME Transition Modules (VTM) receive the inputs from L1CTT and SMT. Serial Link Transmitter and Receiver Boards (LTB/LRB) transmit data between modules.

The STT modules are located in 6 VME creates, each serving two 30-degree azimuthal sectors. Each of these crates holds one FRC, nine STCs - one for eight silicon sensors, and two TFCs - one per 30-degree sector.

<sup>&</sup>lt;sup>18</sup> "A silicon track trigger for the DØ experiment in Run II − Technical Design Report", Evans, Heintz, Heuring, Hobbs, Johnson, Mani, Narain, Stichelbaut, and Wahl, DØ Note 3510.

<sup>&</sup>quot;A silicon track trigger for the DØ experiment in Run II – Proposal to Fermilab", DØ Collaboration, DØ Note 3516.

## 6.3.3 Reconfiguration of STT for Run 2b

The silicon tracker planned for Run 2b consists of more sensors than the present detector. The STT must be upgraded to process the data that these sensors provide. The Run 2b silicon tracker will include 552 readout units (one or more sensors read out through one HDI) arranged in 6 layers of sensors (see

Figure 54). Since one STC accommodates eight such HDIs, 12 STCs are required in each of the six VME crates to process these data. Since we currently have nine STCs per crate, we will need a minimum of 18 additional STC modules.

The data must be channeled into TFCs such that all hits from a track are contained in one TFC. In layers 0, 1, and 2 the overlaps between adjacent sensors are large enough so that each sensor can be uniquely associated with one TFC. This divides the detector into 12 azimuthal sectors as indicated by the shaded regions in

Figure 54. To maintain full acceptance for tracks with  $p_T>1.5$  GeV/c and impact parameter < 2 mm, the data from some sensors in layers 3, 4, and 5 must be channeled into two TFCs, which are in some cases located in different crates. This is not the case in the current configuration, but should not present any problems. We are limited to 8 STC inputs into each TFC, which is sufficient for the Run 2b detector geometry.

#### 6.3.4 Cost and Schedule

The cost estimate for the additional hardware required for the L2STT in Run 2b are shown in the second spreadsheet in Appendix B. The estimate includes our current understanding of the engineering needs. Quantities include 10% spares. The most effective way to acquire this hardware would be at the time the production of STT modules for Run 2a takes place: combining the 2a and 2b production runs, as well as purchasing many of the processors before they become obsolete, would save much time, manpower, and money. Since the Run 2a STT module manufacturing is scheduled for the beginning of CY02, we will need the funds for the Run 2b STT upgrade in FY02.

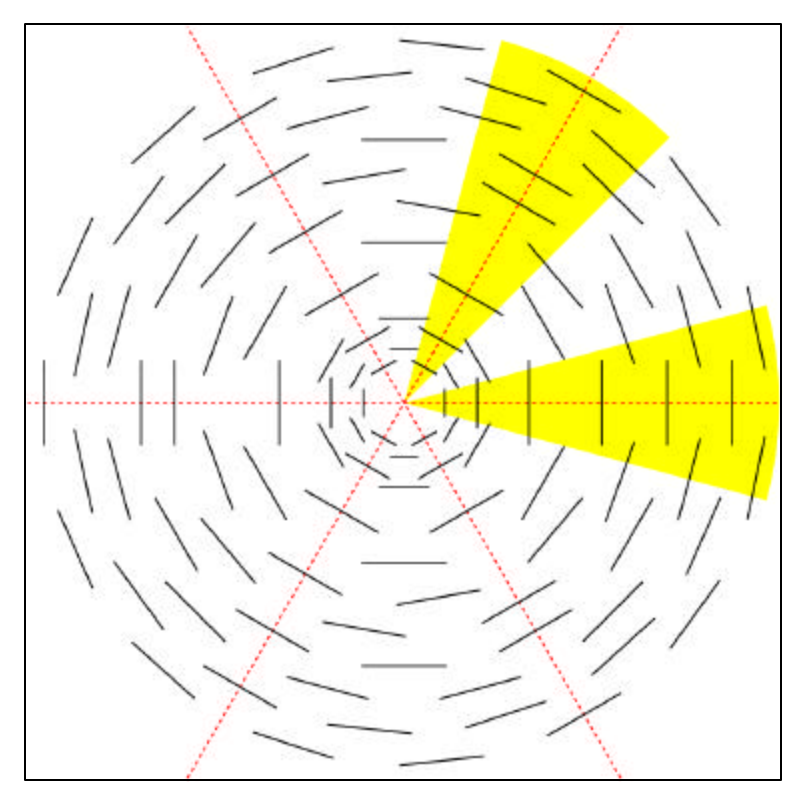


Figure 54. Geometry of D0 Silicon Tracker for Run 2b.

# 6.4 Other Level 2 Options

At this point there are several further options under study.

If it appears that bandwidth limitations will appear because of higher data volume per event in Run 2b, we could consider optimizing MBT firmware to raise DMA bandwidth to perhaps 150MB/s from the present estimate of 120MB/s. The main cost would be engineering time, perhaps \$10-15K. The Alphas will likely limit throughput to 80-100MB/s, but the L2 $\beta$  processors are likely to be capable of larger bandwidth than the current Alpha processors. A further option is to increase the bandwidth of the individual Cypress Hotlinks connections. The transmitters and receivers are capable of upgrading from the current 16MB/s to perhaps 40MB/s. However, the implications of operating such a system need to be explored, given that the muon inputs will likely remain at lower frequency and that hardware is shared between the muon subsystem and other parts of the L2 system. Some hardware might actually have to be rebuilt if this is necessary, so this could be more costly if such a bandwidth upgrade is needed.

Another option under study is adding stereo information to either L1 or L2 triggering to help combat fake axial tracks due to pileup. If this were done in L1, any new outputs from would need to be sent to L2. Such outputs, probably only 4 at most, could require additional FIC-VTM card pairs costing some 5K per additional 4-input card pair. If this option were pursued at Level 2, it would likely result in some 50K in new cards pairs, and another 50K in engineering, backplane, crate, power, and other infrastructure. In the case of L2, this would

have to be justified by an improvement in fake rates after the L2STT tigger confirmation of L1CTT axial tracks.

A third option is calculation of a longitudinal vertex for use in calculating Et and sharpening L2 thresholds. This could be approached by adding post-processing of the L2STT tracks, based on the granularity of detectors, and would result in resolution of a centimeter or two, well-matched to the position precision of L2 data. This would probably require CPU power rather than new hardware. The gain of such improved Et resolution would depend on the physics emphases of Run 2b. Precision physics which requires extremely high acceptance efficiency might actually not prefer such corrections, because erroneous assignments might result in longer acceptance tails than simply using  $Z_V$ =0. But search-oriented physics could use the improved acceptance due to an efficiency curve rising more rapidly to moderately high (80-90%) values.

Another possible upgrade would improvement of the DSP daughter boards of the SLIC, particularly if we find we are I/O limited. Such an effort would be on the scale of 50-100K\$ for hardware and engineering. We will need operational experience with real data to determine whether this proves necessary.

# 6.5 Conclusions for Level 2 Trigger

- The Level 2β upgrade needs the bulk of its funds approved for early 2002, because the initial phase is required for Run 2a.
- The Level 2 STT modifications for the Run 2b SMT also needs the bulk of its funds approved for early 2002, because the new components are most effectively acquired as part of the initial production run.
- Construction of additional VTM's for the Run 2b STT, for readout of the Run 2b SMT, or for providing stereo information to Level 2, should be pursued in a coordinated fashion, and the needs understood soon, because parts are becoming difficult to procure for this design.

# 7 Level 3 Triggers

# 7.1 Status of the D0 Data Acquisition and Event Filtering

## 7.1.1 <u>Description of Current Data Acquisition System</u>

The complete D0 data acquisition system is shown in Figure 55. Data is collected in a VME front-end crate by the VBD boards using VME DMA transfers. The VBD interface board or VBDI (not shown) collects data from one or two chains of VBD's. Each chain consists of as many as 16 VBDs connected by a 32-bit wide data cable. In addition a token loop connects the crates in a chain. Upon receipt of a token, a VBD places its data on the data cable. The token is then modified and passed to the next VBD in the chain which then acts on it. The VBDI board collects the data and sends it over optical link to a VBD readout controller (VRC).

The VRC is a PC with a custom optical link card called the serial interface board (SIB). The SIB is used throughout the system for high-speed data connections. Each VRC contains one input SIB and one output SIB. The system nominally includes eight VRCs.

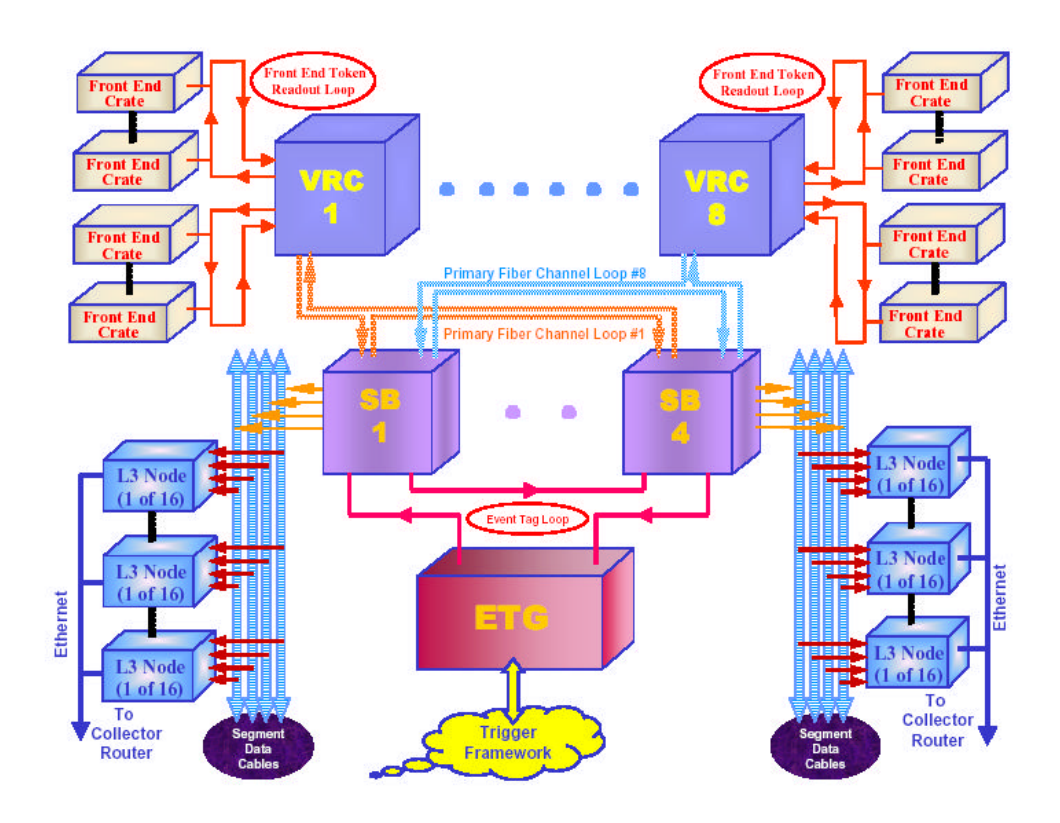


Figure 55. The full L3/DAQ data path.

The VRCs then pass the data to the four segment bridges (SB) via optical links. (Initially the system will be instrumented with three segment bridges but can be scaled to four.) Each VRC sits on a loop communicating with segment bridges. As the data blocks pass through the SB loops they are directed to available L3 nodes. Each SB has four12 SIBs, three each in four PCs. Eight of the SIBs communicate with the VRCs. The remaining four communicate with the Level 3 nodes via optical links.

The L3 nodes have four SIBs and a CPU that collects the data blocks. Once assembled in the L3 nodes the data is transmitted via ethernet to a Cisko switch, which, in turn, transmits the data to a farm of 48 Linux filtering nodes.

The flow and final L3 node destination of an event is directed by the event tag generator (ETG). The ETG uses L1 trigger information and look-up tables to form an "event tag". The tag is sent to each SB via LVDS links. To receive this information each SB has a fifth PC instrumented with an event tag interface (ETI). The ETIs determine if a SB can accept a tag if not, the ETI sends the tag to the next SB. This is a closed, recirculation loop. Tags are returned to the ETG with a bit set for each SB. The ETG can decide to recirculate an event, timeout, or shut down the triggers. The ETG also has a special purpose interface to the L1 trigger called the VBDI-prime.

To recapitulate the system is composed of eight VBDIs, 8 VRCs, 3 SB, 48 L3 nodes, 48 filtering nodes with event flow controlled by the ETG. There are four custom cards in the system including eight VBDIs, about 300 SIBS, three ETIs, and one VBDI-prime.

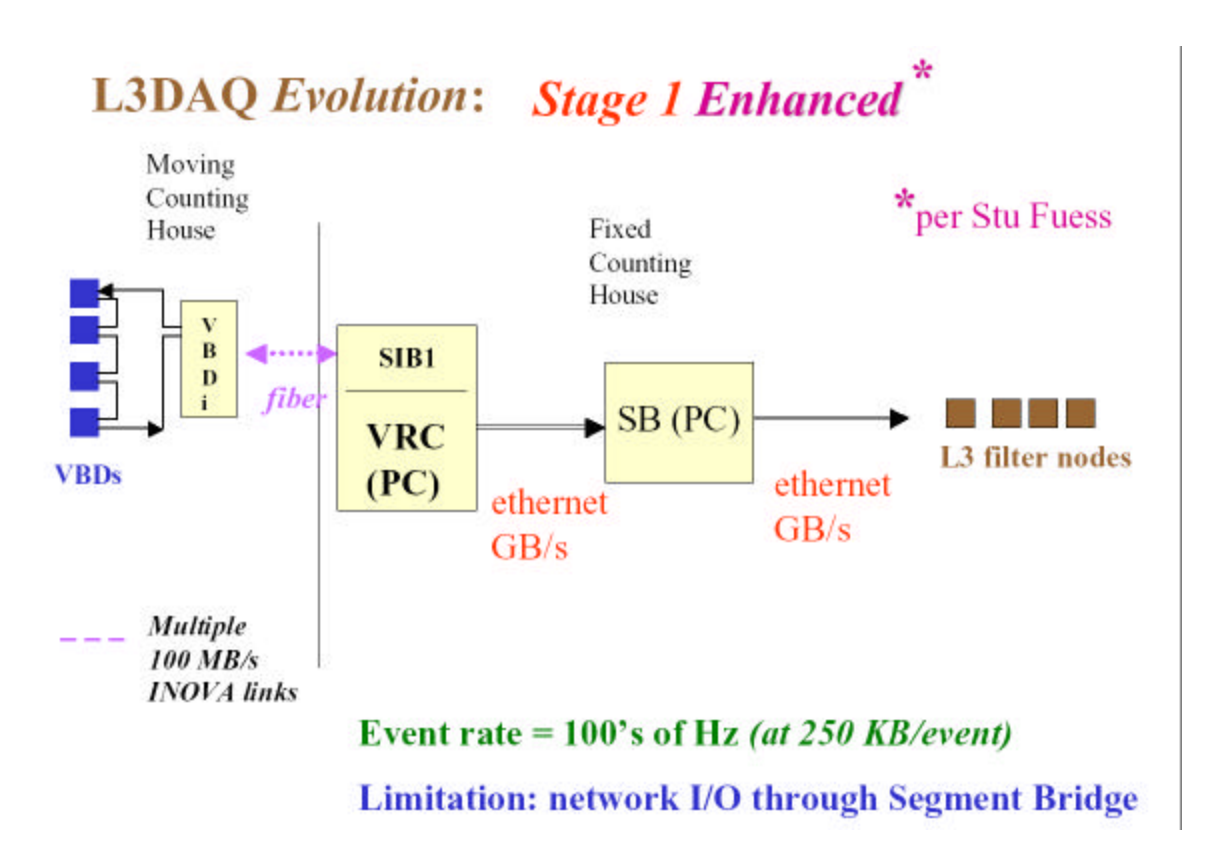


Figure 56. Current scheme at D0.

### 7.1.2 Status

Figure 56 shows the current implementation of the L3 data acquisition and filtering system, which supports commissioning at an 80 Hz event rate. (A typical event has a size of 250 Kbytes.) The VBDs are legacy hardware from Run I and are installed and functioning. Three prototype VBDIs and VRCs transmit data via ethernet to software emulated SBs and ETG. Presently, the events land and are filtered in ten or so L3 nodes.

By the end of the calendar year, numerous upgrades and additions will expand the capacity to 500 Hz and improve filtering capability. The installation of production VBDIs and VRCs and an increase in their number will be required. Similarly the emulated SBs will be upgraded and increased in number. These upgrades are scheduled for October and November. The ethernet switch between the L3 nodes and filter farm as well as the 48 filtering nodes are onhand and will be installed in late September and early October. The filtering farm will be fully commissioned by mid-November.

Layout of the production VBDIs and SIBS is currently underway. Production of sufficient numbers to populate eight VRCs and a prototype hardware SB is scheduled for mid-October. The overall hardware schedule has slipped several months because of technical difficulties with the fiber transceivers. ETI design and production will occur through November and December. The installation of

hardware SBs at D0 will start in February and continue through March. Final commissioning of the system with all components will occur in April and May.

# 7.1.3 An Alternate System

The system described above is the baseline data acquisition system for D0 but has had schedule and technical difficulties. As a result D0 is aggressively developing a backup solution based upon commercial networking hardware. Preliminary analyses and tests show that such a system, shown in Figure 57, is feasible and can provide 1 kHz or more bandwidth. The system is composed of single-board computers (SBC) in each front-end crate, which communicate with the filtering farm through a series of ethernet switches. The SBCs transmit data to a series of 4 Cisco 2948G switches, which, in turn, transmit data to a single Cisco 6509 switch. The large switch finally routes the data to L3 filtering nodes.

SBCs and switches have been ordered for a "slice" test in mid-October. Both the Fermilab Computing Division and D0 are participating in these tests and the system design. The full slice has ten SBCs to read out at least one VME crate of each type, 1 Cisco 2948G switch used to transfer the data from the 10 SBCs on 100 Mbit copper cables to 1 Gbit optical fibers, 1 Cisco 6509 switch to transfer the data from there to the Level 3 nodes, and the 48 Level 3 filter nodes.

Ten SBCs have been ordered from VMIC, and delivery is expected on October 10th. In the meantime, similar, older boards are used for software development. One Cisco 2948G switch has been ordered and should be delivered soon. Fermilab does have a spare, which could be used if necessary, if not needed elsewhere. A spare Cisco 6509 switch has been installed at DAB, and cabling to a number of crates to be used in early tests is underway. All 48 Level 3 filter nodes are available part-time, since integration of the farm in the existing DAQ will also happen during the October shutdown.

On the software front, basic readout of a calorimeter crate has been achieved, and results are encouraging. Good progress has been made on the software design for the full system, and details of the interactions between the various systems are being ironed out. Effort assigned to the project has increased steadily and has reached the minimum required level.

The main tests proposed are: (1)Establish that all types of crates used in D\O\ can be read out reliably using SBCs. (2) Establish that events can be routed from multiple SBCs to individual Level 3 nodes based on Level 1 and 2 trigger decisions while keeping system latency low. (3) Establish that the SBCs can handle simultaneous connections to 48 Level 3 nodes, sending event fragments to each of these. (4) Establish that event building can be done in the level 3 nodes with reasonable CPU consumption. (5) Establish that no congestion occurs at any point of the network when reading out 10 SBCs at high rate (in the full system, the signal from 10 SBCs is carried by 1 fiber link from the Cisco 2948G to the Cisco 6509 switch).

Further tests will involve tuning of communication parameters between the various system components. It should also be demonstrated that nodes receiving

event fragments from 65 SBCs do not exhibit non-linear scaling effects leading to excessive CPU time consumption. While the 10 SBCs are not sufficient to establish this, the 48 nodes can be used instead, since the nature of the sending computer has no impact on this.

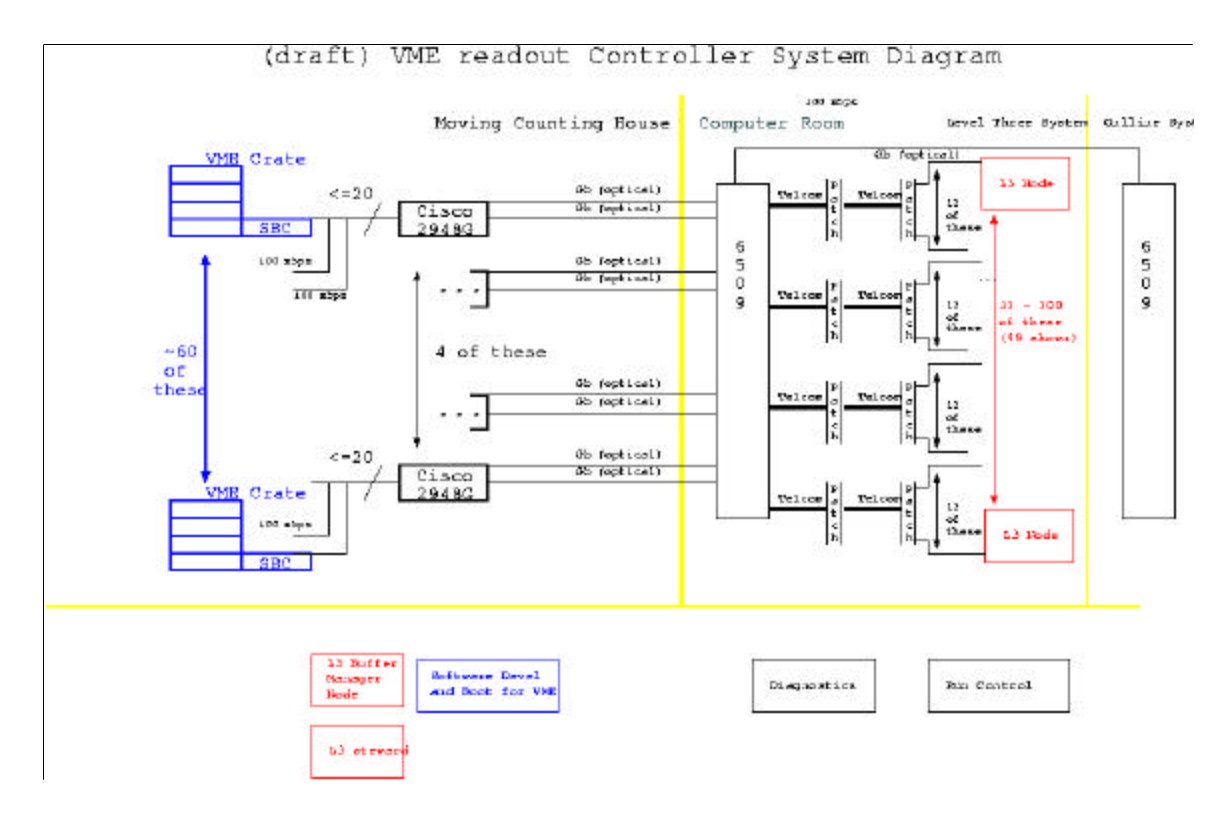


Figure 57. VME/Commodities Solution.

#### 7.1.4 Comments on Current Status

The current Level 3 system as designed by the Brown/ZRL team remains the baseline system being pursued DØ. As has already been noted, the delivery of this system has been plagued by serious schedule and technical difficulties. We are therefore pursuing the commercial alternative as a backup solution should the baseline system continue to encounter difficulties. Management is very carefully monitoring the development of both systems. Extensive discussions of the status of sub-project milestones, technical status, integration issues, and short- and long-term schedule development for both systems take place in weekly meetings with all of the principals. These discussions are overseen by a DAQ Technical Review Committee, appointed in July by the DØ Technical Manager (J. Kotcher), which consists of 10 scientists and technical personnel from both DØ and the Fermilab Computing Division.

The Brown/ZRL solution was costed in equipment funds for the Run 2a upgrade, with more than 80% of the \$1,049k in total project cost having been obligated to date. What remains will be covered by what exists in the original Run 2a estimate, and there is therefore no additional cost associated with this

system. Nevertheless, we consider the risk associated with completion of the baseline DAQ option to be sufficiently high that we have generated a preliminary cost estimate of the commercial DAQ solution (see Table 36 below). The major costs have been based on orders placed for the slice test and the LINUX filter farm development. A contingency of 50% has been applied.

Table 36 Preliminary cost estimate for commercial data acquisition system. A contingency of 50% has been applied. Manpower is not included.

Item	# Required	Unit cost (\$k)	M&S total (\$k)	Cost + 50% Contingency (\$k)
Single board computers	80	2.9	232	348
Digitial I/O cards	80	0.7	56	84
CISCO 6509 switch (with blades)	1	80	80	120
CISCO 2948 switch (concentrators, w/blades)	5	4.2	21	32
Additional filter nodes	16	2.2	35	53
Cables & connectors	-	-	25	38
TOTAL COST			\$449k	\$675k

## 7.2 Run 2b Upgrades to Level 3

The Level 3 trigger consists of two principle elements: a high speed data acquisition system that provides readout of the entire detector at rates expected to exceed 1 kHz, and a processor farm that utilizes software filters written to select events that will be permanently recorded. Since the required Run 2b data acquisition bandwidth is expected to be made available once the Run 2a Level 3 hardware is fully commissioned, the most likely need for Level 3 upgrades will be to provide increased processing power in the farm.

Given the increased selectivity of the Level 1 and Level 2 triggers, it is expected that there will be an increase in the complexity of the Level 3 filter algorithms. This will undoubtedly lead to the need for faster processors in the Level 3 nodes. However, the tremendous flexibility of Level 3 to implement complex trigger filters, combined with the lack of good experience in understanding the trade-off between CPU processing time and trigger rejection, make it very difficult to estimate the required increase in processing power.

Historically, DØ has equipped the Level 3 farm with the fastest processors on the market within the chosen processor family. It would seem reasonable to expect this approach to continue. At the time of the Run 2b upgrade, Moore's law would lead us to expect an approximately four-fold increase in processing

speed over what is currently available. Thus, a significant increase in Level 3 processing power could be obtained by replacing the Run 2a Level 3 processors with the latest technology available in 2004.

#### 7.3 Conclusions

We conclude that the Level 3 processing nodes should be replaced as part of the Run 2b upgrade. We have opted to pursue a series of partial upgrades to the filter farm, performed on a yearly basis as the luminosity increases. The responsibility for this sub-project falls under the online system, and is therefore discussed in more detail in the next section. We note here that the overall cost we anticipate for this upgrade is \$200k.

# 8 Online Computing

### 8.1 Introduction

### 8.1.1 <u>Scope</u>

For the purposes of this document, the DØ Online system will be defined to consist of the following components:

- Online network,
- Level 3 Linux software filter farm,
- Host data logging system,
- Control room computing systems,
- Data monitoring computing systems,
- Database servers,
- File servers.
- Slow control system, plus the associated software for each of these elements.

#### 8.1.2 Software Architecture

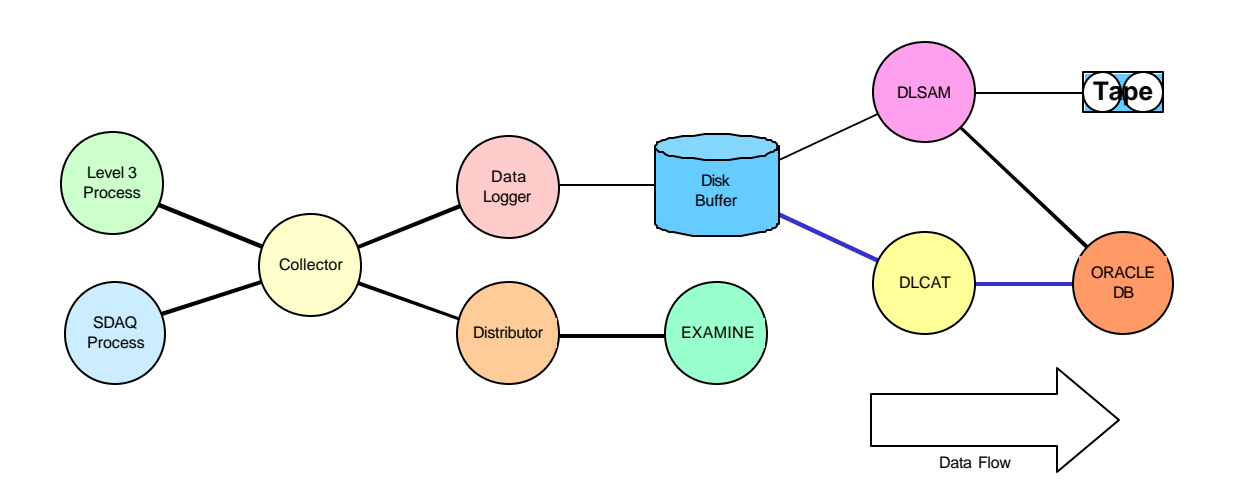


Figure 58. Online System Software Components.

The software architecture of the Run 2B Online system is unchanged from that of Run 2A. Some components will need replacing and/or updating, but there are no structural differences. The major software components of the current system are illustrated in Figure 58. The slow control system components are not illustrated in the figure.

#### 8.1.3 Hardware Architecture

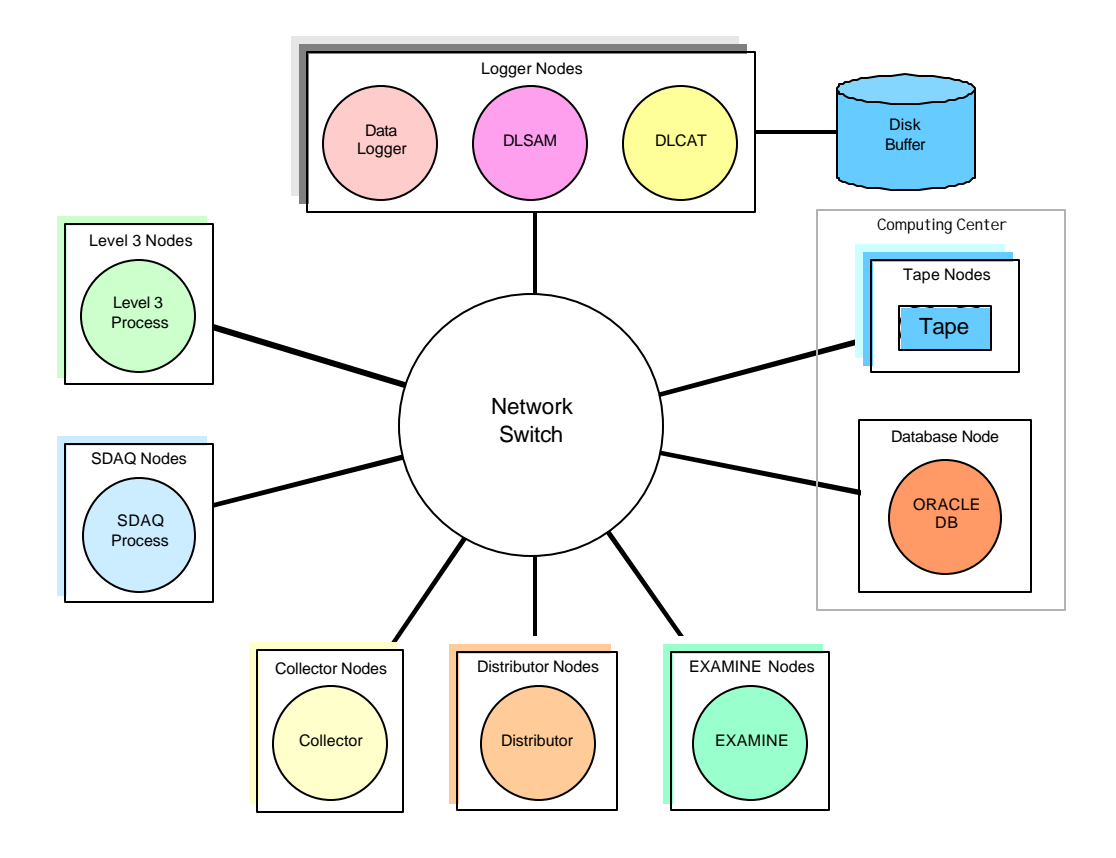


Figure 59. Online System Hardware Components.

The hardware architecture of the Run 2B Online system is also largely unchanged from that of Run 2A. The current architecture is illustrated in Figure 59. The center of the system is one or more high capacity network switches (Cisco 6509). The event data path includes the Level 3 Linux filter nodes, the Collector and Distributor nodes, the Data Logger nodes with large disk buffers, and the final data repository in the Feynman Computing Center. The EXAMINE nodes provide the real-time data monitoring functions. Some of the Slow Control system nodes also participate in the Secondary data acquisition (SDAQ) path. Not included in this figure are the Control Room, File Server, and most of the Slow Control system nodes.

For Run 2B many of these computer systems will need to be updated or replaced.

#### 8.1.4 Motivations

The primary considerations governing the development of the DØ Online system for Run 2B are supplying the enhanced capabilities required for this running period, providing hardware and software maintenance for the (by then) five-year old hardware, and supplying the required software support. We expect

the requirements for the Online data throughput to at least double, largely driven by the ability of the Offline analysis systems to absorb and analyze the data. The Online computing systems will reach the end of their viable lifetime in capability, maintainability, and software support by the Run 2B era. The gradual replacement of many of the component systems will be essential.

#### 8.1.4.1 Enhanced Capabilities

The factors limiting the rate at which DØ records data to tape have been the cost of storage media and the capability of the Offline systems to analyze the data. Assuming five years of improvements in computing capability, it is reasonable to expect the Offline capacity for absorbing and analyzing data to more than double. The Online system should be capable of providing equivalent increased data throughput.

After five years of experience in analyzing events, it can be expected that more sophisticated software filters will be run on the Level 3 trigger farm. These more complicated codes will likely increase execution time. The resulting increased computing demand in Level 3 will need to be met by either an increase in the number of processors, replacement of these units by more capable processors, or both.

It is also expected that data quality monitoring software will be vastly improved by the Run 2B era. These capabilities again are likely to come at the cost of increased execution time and/or higher statistical sampling requirements. In either case, more numerous and more powerful monitoring systems will be required.

#### 8.1.4.2 Hardware and Software Maintenance

By the time of Run 2B, the computing systems purchased for Run 2A will be more than five years old. In the world of computing hardware, this is ancient. Hardware maintenance of such old equipment is likely to be either impossible or unreasonably expensive. Experience shows that replacement by new (and under warranty) equipment is more cost effective. Since replacement of obsolete equipment not only addresses the maintenance question, but also issues of increased capability, it is likely to be the most effective course of action.

The DØ Online system is composed of several subsystems that have differing hardware components and differing maintenance needs. Subsystem specific issues will be addressed in the following sections.

#### 8.1.4.3 Software Support

Several different operating systems are present in the Online system, with numerous custom applications. We have tried, wherever possible, to develop software in as general a fashion as possible so that it can be migrated from machine to machine and from platform to platform. However, support of certain applications is closely tied to the operating system on which the applications run. In particular, ORACLE database operations require expertise that is often specialized to the host operating system. By the time of Run 2B, there is expected to be a consolidation in ORACLE support by the laboratory that will not

include the existing DØ Online database platform. These platforms will thus need to be replaced.

### 8.1.5 <u>Interaction with the Computing Division</u>

The Run 2A Online system was developed through an active partnership with the Computing Division's Online and Database Systems (CD/ODS) group. It is essential that this relationship be maintained during the transition to the Run 2B system. While the level of effort expended by CD/ODS personnel has already decreased relative to what it was during the height of the software development phase of the Run 2A Online system, the continued participation of this group will be needed to maintain the system, and to migrate the existing software to new platforms as these are acquired. Computing Division assistance and expertise will be particularly critical in the area of database support since the Oracle consultant who led the design of the current system is not expected to be involved in maintaining the system. The continued involvement of the CD in the Online effort, which will presumably be described in a future MOU, will be left mostly implicit in later sections of this document, but will nevertheless continue to be crucial to the success of the effort.

#### 8.2 Plan

A description of planned upgrades follows for each component noted in the Introduction. The philosophy and architecture of the Online system will not change, but components will be updated. Note that some changes are best achieved by a continuous, staged approach, while others involve large systems that will need to be replaced as units.

#### 8.2.1 Online Network

The backbone of the DØ Online computing system is the switched Ethernet network through which all components are interconnected. The Run 2A network is based on a Cisco 6509 switch (a second Cisco 6509 switch is under consideration for a network-based DAQ readout system). The switch is composed of a chassis with an interconnecting backplane and various modules that supply ports for attaching the Online nodes. The total capacity of the switch is determined both by the chassis version and the number and versions of the component modules.

The existing Cisco 6509 switch will need to support an increased number of Level 3 nodes, a slight increase in the number of (high bandwidth) host system nodes, and more gigabit-capable modules. The switch chassis will need to be upgraded to support these newer modules. The cost of this upgrade and the new modules is indicated in Table 37.

Table 37. Network upgrade cost.

Item	Cost	Schedule
Upgrade existing Cisco 6509	\$80K	2 years @ \$40K per year

The upgrades of the existing switch will be purchased and installed as required.

#### 8.2.2 Level 3 Linux Filter Farm

The final configuration of the Run 2A Level 3 filter farm is currently unknown. The expected configuration to be completed with Run 2A DAQ funds calls for 48 Windows NT nodes, connected to the readout system, to feed 48 Linux filter nodes. Existing funds do not allow for further expansion of this Linux filter farm.

We expect that the computing capacity of the Linux filter farm will be stressed at current Level 3 input rates with only the existing hardware. As Offline analysis software improves, some algorithms are likely to move into Level 3. As Level 2 filter algorithms are improved, the complexity of the Level 3 algorithms will increase in tandem. All of these efforts to enhance the capability of the Level 3 trigger will come at the expense of processing time. More and improved filter nodes will therefore be required. Table 38 gives a summary of the required hardware.

Table 38. Level 3 node upgrade cost.

Item	Cost	Schedule
Level 3 filter nodes	\$250K	5 years @ \$50K per year

Purchase and installation of the additional Level 3 filter nodes will be staged over the years leading up to Run 2B.

### 8.2.3 <u>Host Data Logging Systems</u>

The current DØ Online Host system comprises three Compaq/Digital AlphaServers in a cluster configuration. Two of the machines are AlphaServer 4000s (purchased in 1997 and 1998) and the third is an AlphaServer GS80 (purchased in 2000). These machines mount disks in the form of two RAID arrays, ~500 GB in a Compaq/Digital HSZ50 unit and ~800 GB in a Compaq/Digital HSG80 unit, and an additional 2.8 TB in Fibre Channel JBOD disk. This cluster supports data logging, the ORACLE databases, and general file serving for the remainder of the Online system.

The long-term maintenance of these systems is a serious concern. While they can be expected to still be operational in the Run 2B era, the high availability required for critical system components may be compromised by the inability to obtain the necessary maintenance support. Maintenance costs, particularly 7x24 coverage, for these systems will increase with age. By the time of Run 2B, maintenance costs are likely to rapidly exceed replacement costs.

These systems currently run Compaq Tru64 UNIX, previously known as Digital UNIX, previously known as Digital OSF1. With the pending purchase of Compaq by Hewlett Packard, long term support for this operating system is problematic.

All applications developed for the data acquisition system that currently run on the Host systems were written with portability in mind. In particular, all will work under Linux. The proposed upgrade to the Host systems is therefore to replace them with Linux servers. Since the existing Host system provides data logging, database support, and file serving functions, each of these needs must be accommodated by the replacement system. These requirements will be addressed individually in this and following sections.

The data logging system must, with high (> 99%) availability, be capable of absorbing data from the Level 3 filter systems, distributing it to logging and monitoring applications, spooling it to disk, reading it from disk, and dispatching it to tape-writing nodes in FCC. The required data rate is an open issue—the minimum required is the current 50 Hz @ .25 Mbytes/event, but this may increase depending on the ability of the Offline computing systems to process the data. The high availability requirement, satisfied in the current system by using a cluster of three machines, precludes the use of a single machine. The amount of disk required to spool the data, and to act as a buffer if Offline transfers are disrupted, is currently ~2.8 Tbytes. Currently the disk buffers are shared by the cluster members, but this is not a strict requirement.

The proposed upgrade solution is for a set (two or three) of Linux servers (dual or quad processors) to act as the new data logging nodes. The data acquisition applications can run in parallel to distribute the load at full bandwidth, but a single node should be capable of handling nearly the entire bandwidth for running under special conditions. Each system will require gigabit connectivity to the Online switch, thereby raising the number of gigabit ports required.

Some R&D effort is needed to test such a configuration. The possibility of clustering the Linux nodes and the possibility of sharing the disk storage should be examined. A purchase of the complete data logging system can be staged, as not all members need to be identical (as noted above, the current Host system was purchased in three increments). The cost of these systems, which can be spread over several years, is noted in Table 39.

Table 39. Host data logging upgrade cost.

Item	Cost	Schedule
DAQ HOST system R&D	\$40K	2 years @ \$20K per year
DAQ HOST system	\$60K	2 years @ \$30K per year

### 8.2.4 <u>Control Room Systems</u>

The current DØ control room is composed of 12 Linux nodes (single and dual processor) that manage 27 monitors. These systems range in age from one to five years. Many of the monitors are already showing the effects of age. It is expected that we should replace some fraction of the control room nodes and monitors each year. The cost of these replacements, spread out over several years, is noted in Table 40.

Table 40. Control room systems upgrade cost.

Item	Cost	Schedule
Control room systems	\$100K	5 years @ \$20K per year

### 8.2.5 <u>Data Monitoring Systems</u>

Real-time monitoring of event data is accomplished by a scheme in which representative events are replicated and distributed to monitoring nodes as they are acquired. The monitoring ranges from examination of low-level quantities such as hit and pulse height distributions to complete event reconstruction. In the latter case, the environment and the code are similar to that of the Offline reconstruction farms. There are one or more monitoring applications for each detector subsystem, and for the trigger, luminosity, and global reconstruction tasks.

The rate at which the monitoring tasks can process events, as well as the complexity of monitoring, are limited by the processing capabilities of the monitoring nodes. The Control Room systems and several rack-mounted Linux nodes currently share this load. Much can potentially be gained by upgrading the experiment's monitoring capability. As more sophisticated analysis software becomes available, these improved codes can be run in the Online environment to provide immediate feedback on data quality.

The monitoring nodes, rack mounted Linux systems, should be continually updated. Such upgrades can occur gradually. The cost, including the infrastructure (racks, electrical distribution), is noted in Table 41.

Table 41. Data monitoring upgrade cost.

Item	Cost	Schedule
Monitoring systems	\$100K	5 years @ \$20K per year

#### 8.2.6 Database Servers

The ORACLE databases currently run on the AlphaServer cluster, with the database files residing on the attached RAID arrays. As mentioned above, long-

term support for this hardware is questionable. Additionally, ORACLE database and application support from the Computing Division no longer includes the Tru64 UNIX platform.

The principal requirement for the database server is high availability (> 99%). Support needs include maintaining the hardware, the operating system, and the application software (ORACLE). User application development also benefits from having independent production and development database instances.

The planned replacement of the database servers is by two redundant SUN or Linux systems with common access to RAID disk arrays. The Computing Division supports both of these systems. The combined cost of the systems, RAID arrays, and tape backup system is noted in Table 42. The purchase of these systems is best staged over two years, with early purchase of the development machine and later purchase of the production machine.

Table 42. Database server upgrade cost.

Item	Cost	Schedule
Development ORACLE system	\$40K	\$40K purchase
Production ORACLE system	\$60K	\$60K purchase

#### 8.2.7 File Servers

The Host cluster currently provides general-purpose file serving. Linux nodes within the Online system access the Host file systems by NFS. Approximately 500 GB of RAID disk is currently available. Files stored include the DØ software library, Fermilab software products, DAQ configuration files, detector subsystem application data, and user home areas. Since the existing file servers are the AlphaServers, replacement is necessary, for reasons already delineated.

The requirement for the file server system is again high reliability (> 99%) of both system and disks. The proposed solution is a pair of redundant Linux servers with common access to both RAID and JBOD disk arrays, plus access to tape backup devices. Acquisition of these systems can be staged. Table 43 shows the costs.

Table 43. File server upgrade cost.

Item	Cost	Schedule
Primary File Server system	\$20K	\$20K purchase
Backup File Server system	\$20K	\$20K purchase

### 8.2.8 Slow Control Systems

The Input/Output Controller (IOC) processors for the DØ Online Slow Control system consists of Motorola 68K and PowerPC single-board computers. These nodes perform downloading, monitoring, and calibration functions critical to the operation of the detector. Both of these processor families have limited lifetimes. By the beginning of Run2B, repairs or replacements for the 68K processor boards will no longer be available and, by the end of the run, the same situation may exist for the PowerPC boards as well. Without a change in single-board computer architecture (for example, moving to Intel processors with a significant accompanying software effort) DØ must be able to sustain operation with the existing systems through Run 2B. At the least, a significant number of spare PowerPC boards – the number based on operational experience – must be purchased and the existing 68K boards in the slow controls system must be replaced.

The functionality of the Muon system 68K processors in the read-out crates is limited by their available memory and memory upgrades are no longer available. Monitoring, control, and calibration functionality would be greatly improved by a complete replacement of these aging processors.

Associated front-end bus hardware, MIL1553 controllers, and rack monitors, are also dependent upon hardware that is no longer available. Spares for these components can no longer be acquired and, since several critical IC chip types are no longer being manufactured, they cannot be repaired. Some devices could be replaced by contemporary systems that employ an Ethernet connection in place of the MIL1553 bus. The existing rack monitors (a general purpose analog and digital signal interface) are prime candidates for such replacement. This would release a number of other MIL1553 components that would then be available for replacement spares. For the remaining MIL1553 devices on the detector platform, reliability would be improved by moving the IOC processors and MIL1553 bus controllers from the Moving Counting House to the platform, thereby eliminating the long runs of the MIL1553 bus cables that have been a significant source of reliability problems.

It is very likely that, by the beginning of Run2B, the operating system on the IOC processors, VxWorks, will no longer be supported at the current level by the Computing Division. The most likely replacement is some version of the Linux system, possibly RT Linux. Conversion of the existing IOC processors to the new operating system, while not requiring significant equipment costs, will involve substantial programming effort. The replacement system must, however, be capable of operating on the existing PowerPC processors.

The replacement of the Muon system processors should take place as soon as possible. The replacement of the 1553 hardware is likely to be spread over many years. The estimate of costs is given in Table 44.

Table 44. Slow control upgrade cost.

Item	Cost	Schedule
Muon processor replacements	\$45K	\$45K purchase
Controls M68K replacements	\$15K	3 years @ \$5K per year
PowerPC spares	\$20K	4 years @ \$5K per year
MIL1553 bus replacements	\$100K	4 years @ \$25K per year

#### 8.3 Procurement Schedule

Table 45 provides a schedule for procurement of the items listed in the above Plan. The fiscal year immediately preceding Run 2B, FY04, will see the greatest expenditures as the bulk of the production systems are purchased. Other purchases are spread out in time, with the philosophy that the Online components will be gradually updated.

Note that Table 45 does not include normal operational costs of the Run 2A and Run 2B Online computing system. Software and Hardware maintenance contracts, repairs, procurement of spares, hardware and software support of Online group personnel, and consumables will equire an additional \$140K per year.

Table 45. Procurement schedule.

				Thousa	inds of \$		
WBS	Item	FY02	FY03	FY04	FY05	FY06	Total
.1.1	Upgrade existing Cisco 6509	\$ 40	\$ 40				\$ 80
.2	Level 3 filter nodes	\$ 50	\$ 50	\$ 50	\$ 50	\$ 50	\$ 250
.3.1	DAQ HOST system R&D	\$ 20	\$ 20				\$ 40
.3.2	DAQ HOST system			\$ 30	\$ 30		\$ 60
.4	Control room systems	\$ 20	\$ 20	\$ 20	\$ 20	\$ 20	\$ 100
.5	Monitoring systems	\$ 20	\$ 20	\$ 20	\$ 20	\$ 20	\$ 100
.6.1	Development ORACLE system		\$ 40				\$ 40
.6.2	Production ORACLE system			\$ 60			\$ 60
.7.1	Primary File Server system				\$ 20		\$ 20
.7.2	Backup File Server system			\$ 20			\$ 20
.8.1	Muon processor replacements	\$ 45					\$ 45
.8.2	Controls M68K replacements		\$ 5	\$ 5	\$ 5		\$ 15
.8.3	PowerPC spares		\$ 5	\$ 5	\$ 5	\$ 5	\$ 20
.8.4	1553 Hardware replacements		\$ 25	\$ 25	\$ 25	\$ 25	\$ 100
	Total	\$195	\$225	\$235	\$175	\$120	\$ 950

#### 8.4 Summary

The need to update and replace DØ Online computing equipment is based mainly on the problems associated with the rapid aging and obsolescence of computing hardware. Maintenance costs, particularly 7x24 costs for high availability systems, rapidly approach replacement costs by systems with much greater functionality. Additionally, software support for operating systems and critical applications (ORACLE) is potentially problematic for the platforms currently in use. There is a possible need for higher bandwidth data logging if this can be accommodated by Offline throughput. There are very real benefits to be accrued from more complex trigger filters and data monitoring software. For these reasons, we plan to update and replace the Online systems.

Replacement systems, wherever possible, will be based on commodity Linux solutions. This is expected to provide the best performance at the lowest cost. The Fermilab Computing Division is expected to support Linux as a primary operating system, with full support of local products and commercial applications. We plan to follow a "one machine, one function" philosophy in organizing the structure of the Online system. In this way, less costly commodity processors can replace costly large machines.

## 9 Summary and Conclusions

The DØ experiment has an extraordinary opportunity for discovering new physics, either through direct detection or precision measurements of SM parameters. An essential ingredient in exploiting this opportunity is a powerful and flexible trigger that will enable us to efficiently record the data samples required to perform this physics. Some of these samples, such as  $p\bar{p}\to ZH\to b\bar{b}\,n\bar{n}$ , are quite challenging to trigger on. Furthermore, the increased luminosity and higher occupancy expected in Run 2b require substantial increases in trigger rejection, since hardware constraints prevent us from increasing our L1 and L2 trigger rates. Upgrades to the present trigger are essential if we are to have confidence in our ability to meet the Run 2b physics goals.

To determine how best to meet our Run 2b trigger goals, a Run 2b Trigger Task Force was formed to study the performance of the current trigger and investigate options for upgrading the trigger. These studies are described in some detail in the previous sections, along with the status and plans for changes in the fiber readout electronics, development of the Level  $2\beta$  trigger system, DAQ, and online systems that are needed well before Run 2b. We summarize below the major conclusions of this report.

- 1. The Analog Front End (AFE) boards used to readout the fiber tracker and preshower detectors require modification to operate with 132 ns bunch spacing. The design of a new daughter board, which would replace the Multi-Chip Modules (MCMs) currently mounted on the AFE boards, is well underway. Completion of the AFE modification is critical to our being able to operate with 132 ns bunch spacing.
- 2. The Level 1 Central Track Trigger (CTT) is very sensitive to occupancy in the fiber tracker, leading to an explosion in the rate for fake high-p<sub>T</sub> tracks in the Run 2b environment. The most promising approach to increasing the selectivity of the CTT is to better exploit the existing axial fiber information available to the CTT. Preliminary studies show significant reductions in the rate of fake tracks are achievable by utilizing individual fiber "singlets" in the track trigger algorithm rather than the fiber doublets currently used. Another attractive feature of the fiber singlet upgrade is that the scope is limited to changing the DFEA daughter boards. While further study is needed to optimize and develop an FPGA implementation of the singlet tracking algorithm, the present studies indicate upgrading the DFEA daughter boards is both feasible and needed to maintain an effective track trigger.
- 3. The Level 1 calorimeter trigger is an essential ingredient for the vast majority of DØ triggers. Limitations in the current calorimeter trigger, which is essentially unchanged from the Run 1, pose a serious threat to the Run 2b physics program. The two most serious issues are the long pulse width of the trigger pickoff signals and the absence of clustering in the jet trigger. The trigger pickoff signals are significantly longer than 132 ns, jeopardizing our

ability to trigger on the correct beam crossing. The lack of clustering in the jet trigger makes it very sensitive to jet fluctuations, leading to a large loss in rejection for a given trigger efficiency. Other limitations include exclusion of ICD energies, inability to impose isolation or HAD/EM requirements on EM triggers, and very limited capabilities for matching tracking and calorimeter information. An upgrade of the L1 calorimeter trigger would allow most, if not all, of these deficiencies to be addressed:

- A digital filter would utilize several samplings of the trigger pickoff signals to properly assign energy deposits to the correct beam crossing.
- Jet triggers would utilize a sliding window to cluster calorimeter energies and significantly sharpen jet energy thresholds.
- ICD energy would be included in the calorimeter energy measurement to increase the uniformity of calorimeter response.
- Electron/photon triggers would allow the imposition of isolation and HAD/EM requirements to improve jet rejection.
- Tracking information could optionally be utilized to improve the identification of electron and tau candidates. Significant improvements in rates for both EM and track-based (τ) triggers have been demonstrated, but further study is needed to better understand how tracking information could be incorporated into the L1 calorimeter trigger and the cost and resources required.
- Topological triggers (for example, an acoplanar jet trigger), would be straight-forward to implement.
- 4. No major changes are foreseen for the Level 1 Muon trigger. Modest upgrades that provide additional scintillator counters in the central region and shielding upgrades may be required for Run 2b.
- 5. The Level 2 Alpha processor boards have suffered from low yield and poor reliability. The replacement of these processors with L2β processors is needed to fully deploy the L2 trigger for Run 2a. In addition, we expect to need to upgrade some of the L2 processors for Run 2b. The L2 Silicon Track Trigger (STT) requires additional cards to accept the increased number of inputs coming from the Run 2b silicon tracker.
- 6. The Level 3 trigger utilizes a high bandwidth Data Acquisition (DAQ) system to deliver complete event information to the Level 3 processor farm where the Level 3 trigger decision is made. For Run 2b, the DAQ must be able to readout the detector at a rate of 1 kHz with a high degree of reliability. DØ is in the process of commissioning its Run 2a DAQ system based on custom hardware that provides the high-speed data paths. We are also exploring an alternative approach based on commercial processors and network switches. Maintaining Level 3 trigger rejection as the luminosity increases will require increasing the processing power of the L3 processor farm as part of the upgrade to the online system.

7. The online computing systems require upgrades in a number of different areas. These upgrades are largely needed to address the rapid aging and obsolescence of computing hardware. We anticipate upgrading our networking infrastructure, L3 farm processors, the online host system, control and monitoring systems, database and file servers, and the 1553 slow control system.

### 9.1 Cost Summary for Trigger Completion and Upgrades

We present in the two tables below a summary of the preliminary cost of the trigger projects being proposed here. We segment the projects into two categories: that covering the completion of and upgrades to the detector for data taking prior to Run 2b, and that addressing the preparations for Run 2b and beyond. The estimates do not include manpower.

At Level 1, we are proposing an upgrade to the calorimeter trigger for Run 2b, which is included in Table 47 below. The studies performed here suggest that an upgrade to the track trigger in which fiber singlet information is integrated at Level 1 will offer significant gains in rejection. In light of what these initial studies have demonstrated, we include the projected cost of this improvement in Table 47. Because it offers more processing power, and does not require the invasive and technically risky process of removing FPGAs from the existing daughter boards, we have chosen the option in which the daughter boards are replaced. Both of these upgrades are being targeted for FY03 and FY04.

The dominant portion of the funds required for the Level  $2\beta$  system is earmarked for the Run 2a system, which will be completed within the next calendar year. These funds will therefore be needed in FY02. Taking into account the \$192k in funding that has already been identified, completion of the Run 2a Level  $2\beta$  project requires a total of \$370. In anticipation of a partial upgrade of the Level 2 trigger system for Run 2b – in particular, the handling and processing of information from the track trigger and possibly the Silicon Track Trigger – we include in Table 47 a line item corresponding to a processor upgrade of 12 of the 24 Level  $2\beta$  boards. In addition, we note that the funds for the upgrade of the STT for Run 2b are requested in FY02. This is to allow us to exploit significant gains in time and money by piggybacking on the Run 2a STT production run in early CY02. Obsolescence of some of the processors over the next three years is also a concern; these will be purchased for both the baseline and upgraded STT in FY02 as well.

As noted in Section 7.1.4, the Brown/ZRL DAQ system remains our baseline data acquisition system, and is financially covered in the original Run 2a cost estimate, with most (more than 80%) of the money having already been obligated. We therefore do not include a cost for that system below. We consider the risk associated with the delivery of this system to be substantial enough that we include the estimated cost for the commercial DAQ option in Table 46 below. Should this option be pursued, we anticipate that the bulk of the money will be needed in FY02, with some limited complementary portion required in early FY03.

An estimated total of \$950k is needed to cover yearly project-related upgrades to the online system for the five year period spanning FY02 through FY06, inclusive. These upgrades include the LINUX filter farm for the Level 3 trigger, the slow controls system, etc. We assume here that this money will come out of the operating budget - pending final discussions with the Laboratory - and therefore do not include this sum in the tables below, which represent estimates for equipment expenditures. We note that this money for online upgrades is requested in addition to the yearly operating allocation for online support for  $D\varnothing$  operations.

Table 46. Preliminary cost estimate to complete trigger sub-projects required prior to Run 2b. Total includes secondary (commercial) DAQ option. Manpower is not included. \* Rows corresponding to Level  $2\beta$  and TOTAL do not account for \$192k in funds already identified for the Level  $2\beta$  sub-project.

Sub-Project	M&S (\$k)	Contingency (%)	Total (\$k)	Fiscal Year Needed
SIFT Replacement (Option 1)	410	54	630	FY02-03
Level 2β*	411	37	562	FY02
Commercial DAQ system	449	50	675	FY02-03
TOTAL*	\$1,270k		\$1,867k (incl. DAQ option)	

Table 47. Preliminary cost estimate for projects associated with detector upgrades for Run 2b. Manpower is not included.

Sub-Project	M&S (\$k)	Contingency (%)	Total (\$k)	Fiscal Year Needed
Level 1 Calorimeter Trigger	730	100	1,460	FY03-04
Level 1 Track Trigger	360	50	540	FY03-04
Level 2β	62	34	83	FY03-04
Level 2 Silicon Track Trigger	392	40	549	FY02
TOTAL	\$1,544k		\$2,632k	

## A D0 Run 2b Trigger Task Force

### A.1 Task Force Charge

The Run 2b Trigger Task Force is charged with developing a plan for a Run 2b trigger system that allows D0 to run at 132 nsec, and a luminosity of  $5\times10^{32}$ , with the following output trigger rates:

L1: 5 kHz L2: 1 kHz

L3: 50 Hz.

The upgraded trigger system will ideally allow D0 to run with a full complement of triggers, thereby spanning the space of physics topics available in Run 2b. It should be ready for installation at D0 by the summer of 2004, and must remain within reasonable bounds in terms of cost, technical resources, development and production time, and the impact on the existing detector. The addition of new tracking detectors, a greatly expanded cable plant, or significant additions to the number of crates in the Movable Counting House are examples of options that will in all probability not be feasible, given the time, manpower and hardware constraints that we are facing. The Task Force should take such constraints into consideration as it explores the various options.

The tight time constraints the Task Force is facing will in all probability not allow them to consider the full suite of possible Run 2b triggers. They should therefore consider focusing on the essential elements of the Run 2b high-pT physics program, of which the Higgs search is of paramount importance. The bandwidth requirements and trigger efficiencies that result from the implementation of the available technical solutions, applied to provide the needed rejection, should be estimated.

To guide their work in the relatively short time that is available, the Task Force may assume that the most extensive upgrade is likely to be needed at Level 1. Feasibility arguments for upgrades to the higher trigger levels - which may be based on expected improvements in processing power, for example - might be sufficient, depending on what is learned during their studies. Should their investigations indicate that more extensive upgrades at Levels 2 or 3 (i.e., board replacements, etc.) will be needed, however, they should outline this in a more comprehensive manner in their report.

The Task Force should submit a Conceptual Design Proposal that lists the proposed upgrades to the Run 2b Project Manager by September 17, 2001. These recommendations should be supported by physics simulations, and include an estimate of the financial and technical resources required, an outline of the expected schedule for delivery, and the impact on the existing detector infrastructure.

# A.2 Trigger Task Force Membership

Brad Abbott, Maris Abolins, Drew Alton, Levan Babukhadia, Drew Baden, Vipin Bhatnagar, Fred Borcherding, John Butler, Jiri Bystricky, Sailesh Chopra, Dan Edmunds, Frank Filthaut, Yuri Gershtein, George Ginther, Ulrich Heintz, Mike Hildreth (co-chair), Bob Hirosky, Ken Johns, Marvin Johnson, Bob Kehoe, Patrick Le Du, Jim Linnemann, Richard Partridge (co-chair), Pierre Petroff, Emmanuelle Perez, Dean Schamberger, Kyle Stevenson, Mike Tuts, Vishnu Zutshi

# B Level 2b and Level 2 STT Cost Estimates

The cost estimates for that portion of the Level  $2\beta$  project associated with the completion of the Run 2a detector, and the Run 2b upgrade to the L2 STT, are shown in the spreadsheets below. Our current estimates of the engineering needs for each are included.

Table 48: Cost estimate for the Run 2a Level 2β project. Engineering is included.

WBS	2.1	Title							1						
WBS	ITEM	MATE	RIALS &	SERVICES	(M&S)	CONTING	ENCY		1			Sources of	Funds		
2.1	Level 2 Beta Processor 2a	Unit	#	Unit	M&S			TOTAL	Spent			Fermi			dentifie
				Cost	TOTAL	%	Cost	Cost	to date	ETC	Orsay	Prototype	Fermi 2a Fe	ermi 2t <sup>-</sup>	<b>Fotal</b>
2.1.1	Motherboard				243,489	28	68,131	311,621	74,417	169,072	138,328	27,000	0	0	165,328
2.1.1	Engineering and Design				131,415	3	3,425	134,840	64,415	67,000	128,415	3,000	0	0	131,415
2.1.1.1	Exploratory Design (Maryland)	lot	1	3,000	3,000	0	3,423	3,000	3,000		120,413	3,000			3,000
2.1.1.1.2	Design and schematics (Orsay)	yr	0.7	100,000	70,000	0	0	70,000	50,000		70,000	•			70,000
2.1.1.1.3		yr	0.17	100,000	17,000	0	0	17,000	30,000	17,000	17,000				17,000
2.1.1.1.4	Mechanical Engineering (Thales)	lot	1	11,415	11,415	30	3,425	14,840	11,415		11,415				11,415
2.1.1.1.5	Testing and Commissioning (Orsay)	vr	0.30	100,000	30,000	0	0	30,000		30,000	30,000				30,000
2.1.1.2	Setup Engineering by Assembler (Thales)				6,032	50	3,016	9,048	0	6,032	C	6,500	0	0	6,500
2.1.1.2.1	PC Board	lot	1	1,974	1,974	50	987	2,961	i	1,974		***************************************			0
2.1.1.2.2	Assembly	lot	1	1,958	1,958	50	979	2,937		1,958					0
2.1.1.2.3	Testing	lot	1	2,100	2,100	50	1,050	3,150	· ·	2,100					0
2.1.1.3	Prototype Board			4,335	17,339	100	17,339	34,679	10,002	7,337	9,913	17,500	0	0	27,413
2.1.1.3.1	PC Board	ea	4	1,245	4,981	100	4,981	9,416		4,435					0
2.1.1.3.2	Assembly	ea	4	168	672	100	672	5,653		4,981					0
2.1.1.3.3	Testing	ea	4	68	273	100	273	945		672					0
2.1.1.3.4	Mechanical parts	ea	4	1,109	4,435	100	4,435	4,708	4,435		4,435				4,435
2.1.1.3.5	BGAs	ea	5	813	4,067	100	4,067	8,133	4,067		4,067				4,067
2.1.1.3.6	OtherComponents	ea	5	282	1,411	100	1,411	2,822		1,411	1,411				1,411
2.1.1.3.7	Connectors	ea	4	375	1,500	100	1,500	3,000	1,500						0
2.1.1.4	Production Board			2,334	88,703	50	44,351	133,054	0	88,703		0	0	0	0
2.1.1.4.1	PC Board	ea	38	672	25,520	50	12,760	24,447		11,687					0
2.1.1.4.2	Assembly	ea	38	170	6,464	50	3,232	28,752		25,520					0
2.1.1.4.3	Testing	ea	38	32	1,197	50	599	7,062		6,464					0
2.1.1.4.4	Mechanical parts	ea	42	278	11,687	50	5,843	7,040		1,197					0
2.1.1.4.5	BGAs	ea	42 42	809	33,957	50	16,979 4,939	50,936		33,957					0
2.1.1.4.6 2.1.1.4.7	Other Components Connectors	ea	42	235	9,878	50 50	4,939	14,818		9,878					0
2.1.1.4.7	Processors	ea	42	0	129,523	49	63,050	192,573	14,389	115,134	3,513	23,000	0	0	26,513
2.1.2.1	Prototypes				23,651	43	10,114	33,765	14,389	9,262	3,513	23,000	0	0	26,513
2.1.2.1.1	VMIC processor	ea	1	3,423	3,423	0	10,114	3,423	3,423		3,113	23,000	J	- 0	20,513
2.1.2.1.2	CPCI Crate	ea	1	3,375	3,375	50	1,688	5,063	3,375						0
2.1.2.1.3	CPCI Crate Equipment	lot	1	565	565	50	283	848	565						0
2.1.2.1.4	Advantech SBC	ea	4	3,513	14,052	50	7,026	21,078	7,026		3,513				3,513
2.1.2.1.5	Heat Sink Modification	ea	4	125	500	50	250	750		500					0
2.1.2.1.6	DiskDrive	ea	4	200	800	50	400	1,200	•	800					0
2.1.2.1.7	2nd CPU Chip	ea	4	234	936	50	468	1,404		936					0
2.1.2.2	Production Boards			4,072	105,872	50	52,936	158,808	0	105,872	0	0	0	0	0
2.1.2.2.1	Advantech SBC	ea	26	3,513	91,338	50	45,669	137,007		91,338					0
2.1.2.2.2	Heat Sink Modification	ea	26	125	3,250	50	1,625	4,875		3,250					0
2.1.2.2.3	DiskDrive	ea	26	200	5,200	50	2,600	7,800	<b>.</b>	5,200					0
2.1.2.2.4	2nd CPU Chip	ea	26	234	6,084	50	3,042	9,126		6,084					0
2.1.3	Maintenance Facilities	ļ			38,400	50	19,200	57,600	0	38,400		0	0	0	0
2.1.3.1	VIPA Crate	ea	2	5,000	10,000	50	5,000	15,000		10,000					0
2.1.3.2	Mbus Backplane	ea	2	500	1,000	50	500	1,500		1,000					0
2.1.3.3	Mbus Terminators	ea	4	100	400	50	200	600		400					0
2.1.3.4	Power	ea	2	5,000	10,000	50	5,000	15,000		10,000					0
2.1.3.5	Bit3 Interface	ea	2	4,000	8,000	50	4,000	12,000		8,000					0
2.1.3.6	Control PC	ea	2	2,000	4,000	50	2,000	6,000		4,000					0
2.1.3.7	Test Equipment	ea	2	2,500	5,000	50	2,500	7,500		5,000					0
2.1	Level 2 Beta Processor 2a				411,412	37	150,381	561,794	88,806	322,606	141,841	50,000	0	0	191.841
		•			,	<u> </u>	54.01	- 329.73	50,000		- 129071	20,000	<u> </u>		

Table 49: Cost estimate for the Run 2b Level 2 STT upgrade. Engineering is included.

WBS	2.2	Title						
WBS	ITEM	MATERIALS & SERVICES (M&S)				CONTINGENCY		
2.2	Level 2 STT Upgrade	Unit	#	Unit Cost	M&S TOTAL	%	Cost	TOTAL Cost
2.2.1	Boards (more of existing types)				275,755	37	103,288	379,043
2.2.1.1	Motherboard	ea	32	2,000	64,000	30	19,200	83,200
2.2.1.2	STC Logic Board	ea	20	2,500	50,000	30	15,000	65,000
2.2.1.3	Link Transmitter Board (LTB)	ea	52	200	10,400	30	3,120	13,520
2.2.1.4	Link Receiver Board (LRB)	ea	33	550	18,150	30	5,445	23,595
2.2.1.5	Buffer Controller Board (BC)	ea	32	950	30,400	30	9,120	39,520
2.2.1.6	VME Transition Module (VTM)	ea	20	2,500	50,000	50	25,000	75,000
2.2.1.7	Track Fit Card (TFC)	ea	8	5,000	40,000	50	20,000	60,000
2.2.1.8	Board Testing	ea	197	65	12,805	50	6,403	19,208
2.2.2	Link Echo Board				48,290	49	23,807	72,097
2.2.2.1	Design & Prototyping	hours	960	35	33,600	50	16,800	50,400
2.2.2.2	Production	ea	26	500	13,000	50	6,500	19,500
2.2.2.3	Testing	ea	26	65	1,690	30	507	2,197
2.2.3	Software & Firmware changes				33,600	50	16,800	50,400
2.2.3.1	STC	hours	960	35	33,600	50	16,800	50,400
2.2.4	J3 Backplane				15,131	41	6,266	21,397
2.2.4.1	Design & Layout	lot	1	5,000	5,000	50	2,500	7,500
2.2.4.2	Setup for production	lot	1	1,500	1,500	30	450	1,950
2.2.4.3	Backplanes	ea	10	500	5,000	30	1,500	6,500
2.2.4.4	Connectors	ea	10	363	3,631	50	1,816	5,447
2.2.5	Cables				18,950	35	6,675	25,625
2.2.5.1	LVDS	ea	165	30	4,950	50	2,475	7,425
2.2.5.2	Splitters	ea	80	125	10,000	30	3,000	13,000
2.2.5.3	Fibers	ea	160	25	4,000	30	1,200	5,200
2.2	Level 2 STT Upgrade				391,726	40	156,835	548,561